
AFRL-RZ-WP-TP-2009-2107

# AIRCRAFT THERMAL MANAGEMENT USING LOOP HEAT PIPES

**Andrew J. Fleming, Scott K. Thomas, Kirk L. Yerkes, and Quinn H. Leland**

**Thermal and Electrochemical Branch**
**Energy/Power/Thermal Division**

**MARCH 2009**



**AIR FORCE RESEARCH LABORATORY**
**PROPULSION DIRECTORATE**
**WRIGHT-PATTERSON AIR FORCE BASE, OH 45433-7251**
**AIR FORCE MATERIEL COMMAND**
**UNITED STATES AIR FORCE**

# REPORT DOCUMENTATION PAGE

*Form Approved*
*OMB No. 0704-0188*



| 1. REPORT DATE *(DD-MM-YY)* | 2. REPORT TYPE | 3. DATES COVERED *(From - To)* |
|---|---|---|
| March 2009 | Technical Paper | 01 January 2005 – 20 March 2009 |

**4. TITLE AND SUBTITLE**
AIRCRAFT THERMAL MANAGEMENT USING LOOP HEAT PIPES

**5a. CONTRACT NUMBER**
In-house

**5b. GRANT NUMBER**

**5c. PROGRAM ELEMENT NUMBER**
62203F

**6. AUTHOR(S)**
Andrew J. Fleming, Scott K. Thomas, Kirk L. Yerkes, and Quinn H. Leland

**5d. PROJECT NUMBER**
3145

**5e. TASK NUMBER**
20

**5f. WORK UNIT NUMBER**
314520C9

**7. PERFORMING ORGANIZATION NAME(S) AND ADDRESS(ES)**
Thermal and Electrochemical Branch (AFRL/RZPS)
Energy/Power/Thermal Division
Air Force Research Laboratory, Propulsion Directorate
Wright-Patterson Air Force Base, OH 45433-7251
Air Force Materiel Command, United States Air Force

**8. PERFORMING ORGANIZATION REPORT NUMBER**
AFRL-RZ-WP-TP-2009-2107

**9. SPONSORING/MONITORING AGENCY NAME(S) AND ADDRESS(ES)**
Air Force Research Laboratory
Propulsion Directorate
Wright-Patterson Air Force Base, OH 45433-7251
Air Force Materiel Command
United States Air Force

**10. SPONSORING/MONITORING AGENCY ACRONYM(S)**
AFRL/RZPS

**11. SPONSORING/MONITORING AGENCY REPORT NUMBER(S)**
AFRL-RZ-WP-TP-2009-2107

**12. DISTRIBUTION/AVAILABILITY STATEMENT**
Approved for public release; distribution unlimited.

**13. SUPPLEMENTARY NOTES**
Master of Science in Engineering Dissertation, Wright State University, Dayton, OH.
PAO Case Number: 88ABW 2009-1066; Clearance Date: 17 Mar 2009. Paper contains color.

**14. ABSTRACT**
The objective of this thesis was to determine the feasibility of using loop heat pipes to dissipate waste heat from power electronics to the skin of a fighter aircraft and examine the performance characteristics of a titanium-water loop heat pipe under stationary and elevated acceleration fields. In the past, it has been found that the boundary condition at the condenser can be a controlling factor in the overall performance of this type of thermal management scheme. Therefore, the heat transfer removed from the aircraft skin has been determined by modeling the wing as a flat plate at zero-incidence as a function of the following parameters: airspeed: $0.8 \leq \mathrm{Ma}_\infty \leq 1.4$; altitude: $0 \leq H \leq 22$ km; wall temperature: $105 \leq T_w \leq 135$ °C. In addition, the effects of the variable properties of air have been taken into account. Heat transfer due to thermal radiation has been neglected in this analysis due to the low skin temperatures and high airspeeds up to $\mathrm{Ma}_\infty = 1.4$. It was observed that flight speed and altitude have a significant effect on the heat transfer abilities from the skin to ambient, with heat rejection becoming more difficult with increasing Mach number or decreasing altitude.
*Abstract concludes on reverse →*

**15. SUBJECT TERMS**
LHP, loop heat pipe, elevated acceleration, centrifuge table, compensation chamber heat input, convective heat transfer, flat plate, supersonic flow

| 16. SECURITY CLASSIFICATION OF: | | | 17. LIMITATION OF ABSTRACT: | 18. NUMBER OF PAGES | 19a. NAME OF RESPONSIBLE PERSON (Monitor) |
|---|---|---|---|---|---|
| a. REPORT | b. ABSTRACT | c. THIS PAGE | | | Andrew J. Fleming |
| Unclassified | Unclassified | Unclassified | SAR | 158 | 19b. TELEPHONE NUMBER *(Include Area Code)* N/A |

**Standard Form 298 (Rev. 8-98)**
Prescribed by ANSI Std. Z39-18

**14. ABSTRACT (concluded)**

An experiment has been developed to examine operating characteristics of a titanium-water loop heat pipe (LHP) under stationary and elevated acceleration fields. The LHP was mounted on a 2.44 m diameter centrifuge table on edge with heat applied to the evaporator via a mica heater and heat rejected using a high-temperature polyalphaolefin coolant loop. The LHP was tested under the following parametric ranges: heat load at the evaporator: $100 \leq Q_{in} \leq 600$ W; heat load at the compensation chamber: $0 \leq Q_{cc} \leq 50$ W; radial acceleration: $0 \leq a_r \leq 10$ g. For stationary operation ($a_z = 1.0$ g, $a_r = 0$ g), the LHP evaporative heat transfer coefficient decreased monotonically, thermal resistance decreased to a minimum then increased, and wall superheat increased monotonically. Heat input to the compensation chamber was found to increase the evaporative heat transfer coefficient and decrease thermal resistance for $Q_{in} = 500$ W. Flow reversal in the LHP was found for some cases, which was likely due to vapor bubble formation in the primary wick. Operating the LHP in an elevated acceleration environment ($a_z = 1.0$ g, $a_r > 0$ g) revealed dry-out conditions from $Q_{in} = 100$ to 400 W and varying accelerations and the ability for the LHP to reprime after an acceleration event that induced dry-out. Evaporative heat transfer coefficient and thermal resistance as found not to be significantly dependent on radial acceleration. However, wall superheat was found to increase slightly with radial acceleration.

**TABLE OF CONTENTS**

**LIST OF FIGURES**

**LIST OF TABLES**

**NOMENCLATURE**

| | |
|---|---|
| $a$ | Speed of sound, m/s; acceleration, m/s$^2$; flow meter calibration constant |
| $b$ | Flow meter calibration constant |
| $B$ | Experimental constant related to Eq. (F.2) |
| $c$ | Flow meter calibration constant |
| $C_f$ | Skin friction coefficient, $2D/(\rho U^2 A)$ |
| $C_p$ | Specific heat, J/(kg-K) |
| $d$ | Flow meter calibration constant |
| $D$ | Diameter, m |
| $f$ | Frequency, Hz |
| $g$ | Acceleration due to standard gravity, 9.81 m/s$^2$ |
| $h$ | Heat transfer coefficient, W/(m$^2$-K) |
| $H$ | Altitude, m |
| $k$ | Thermal conductivity, W/(m-K) |
| $L$ | Length, m |
| $m$ | Mass, kg |
| Ma | Mach number, $U / a$ |
| $n$ | Number of data points |
| Nu | Nusselt number, $hD/k$ |
| Pr | Prandtl number, $k/(\rho C_p)$ |
| $Q$ | Heat transfer rate, W |
| $q$ | Heat flux, W/m$^2$ |
| $r$ | Recovery factor; radial coordinate, m |
| $R$ | Particular gas constant, m$^2$/(s$^2$-K); thermal resistance, K/W |
| $R^2$ | Coefficient of determination |
| Ra | Rayleigh number, $g\beta(T_s - T_\infty)D^3/\nu\alpha$ |

| | |
|---|---|
| Re | Reynolds number, $\rho U x/\mu$ |
| St | Stanton number, $h/(\rho U C_p)$ |
| $t$ | Time, s; t-distribution |
| $T$ | Temperature, K |
| $U$ | Velocity, m/s |
| $V$ | Voltage, V; volume, L |
| $y_0$ | Flow meter calibration constant |

Greek Letters

| | |
|---|---|
| $\alpha$ | Thermal diffusivity, $m^2/s$ |
| $\beta$ | Inverse temperature, $K^{-1}$ |
| $\gamma$ | Ratio of specific heats |
| $\Delta T$ | Temperature difference, K |
| $\varepsilon$ | Emissivity |
| $\theta$ | Angle, degrees |
| $\mu$ | Absolute or dynamic viscosity, $(N\text{-}s)/m^2$ |
| $\nu$ | Kinematic viscosity, $m^2/s$ |
| $\rho$ | Density, $kg/m^3$ |
| $\sigma$ | Standard deviation; Stefan-Boltzmann constant, $5.67\times10^{-8}$ $W/(m^2\text{-}K^4)$ |
| $\varphi$ | Fluid phase |
| $\omega$ | Angular velocity, rad/s |

Superscripts

| | |
|---|---|
| * | Film condition |
| + | Normalized |
| 1φ | Single-phase |
| 2φ | Two-phase |

Subscripts

| | |
|---|---|
| 1 | Heat into vaporization of fluid |
| 2 | Heat leak to the compensation chamber |

| | |
|---|---|
| $\infty$ | Freestream condition |
| a | Actual |
| amb | Ambient |
| aw | Adiabatic wall |
| c | Condenser |
| cc | Compensation chamber |
| cl | Centerline |
| cm | Condenser midpoint |
| conv | Convection |
| cp | Cold plate |
| ct | Centrifuge table |
| dev | Deviation |
| D | Diameter |
| e | Evaporator |
| eg | Ethylene glycol |
| e/cc | Evaporator/compensation chamber junction |
| ie | Inner edge |
| in | Cold plate inlet; heat in to evaporator |
| L | Local |
| max | Maximum value |
| min | Minimum value |
| m/t | Mass/time |
| oe | Outer edge |
| out | Cold plate outlet; heat out of condenser |
| p | Predicted |
| PAO | Polyalphaolefin |
| r | Radial |
| R | Reference condition |
| rad | Radiation |
| s | Surface |
| sh | Superheat |

| | |
|---|---|
| surr | Surroundings |
| TC | Thermocouple |
| tot | Total |
| v | Vapor |
| V/T | Voltage/temperature |
| w | Wall |
| z | Axial |
| θ | Azimuthal |

# 1. CONVECTIVE HEAT TRANSFER FROM HIGH-SPEED AIRCRAFT SKIN

## 1.1. Abstract

The objective of the present analysis was to determine the feasibility of using loop heat pipes to dissipate waste heat from power electronics to the skin of a fighter aircraft. In the past, it has been found that the boundary condition at the condenser can be a controlling factor in the overall performance of this type of thermal management scheme. Therefore, the heat transfer removed from the aircraft skin has been determined by modeling the wing as a flat plate at zero-incidence as a function of the following parameters: airspeed: $0.8 \leq \mathrm{Ma}_\infty \leq 1.4$; altitude: $0 \leq H \leq 22$ km; wall temperature: $105 \leq T_\mathrm{w} \leq 135$°C. In addition, the effects of the variable properties of air have been taken into account. Heat transfer due to thermal radiation has been neglected in this analysis due to the low skin temperatures and high airspeeds up to $\mathrm{Ma}_\infty = 1.4$. It was observed that flight speed and altitude have a significant effect on the heat transfer abilities from the skin to ambient, with heat rejection becoming more difficult with increasing Mach number or decreasing altitude.

## 1.2. Introduction

The More Electric Aircraft initiative (MEA) is the concept for future aircraft including warfighter, transport, helicopters, and commercial aircraft. This approach has been adopted by the United States Air Force since the early 1990's with the purpose of reducing or removing as many of the hydraulic, mechanical, and pneumatic power components and replacing them with electrically driven devices. This approach to aircraft design was first envisioned during World War II. However, at that time, the power generation capability and power conditioning equipment required was not feasible due to volume requirements. As a result, hydraulic, pneumatic, and mechanical systems became the norm for aircraft until this initiative. Under the MEA paradigm, power for systems such as flight control actuation, anti-ice, braking, environmental control, engine starting, and fuel pumping will be provided by a starter/generator driven by the gas

generator spool of the aircraft engine (Quigley, 1993). The MEA initiative has been analytically proven to improve aircraft reliability, maintainability, support, and operations cost as well as reduce weight, volume, and enhance battle damage reconfigurability (Cloyd, 1997).

While the reduction of hydraulic, pneumatic, and mechanical systems in favor of electrical systems is beneficial, it presents a problem in terms of thermal management. Replacing the centralized hydraulic system with an electrical based system removes a primary method of transporting and removing waste heat (Vrable and Yerkes, 1998). A separate cooling fluid system for thermal management would be contrary to the goals of the MEA initiative. Therefore, thermal management would need to be distributed over the entire aircraft. As a result, a new approach to thermal management involves handling heat loads on a local level. This means taking individual components in the aircraft and locally handling their heat rejection requirements.

The operating envelope for military aircraft places stringent limitations on any proposed thermal management system. The on-board electrical flight control actuation system operates at altitudes from sea level to above 12 km, airspeeds from stationary to supersonic speeds, transient body forces up to 9 g due to maneuvering, and ambient temperatures from -68 to 58ºC. MEA has resulted in the development of high-temperature, high-efficiency, and high-density power electronic component technologies. The next-generation power electronics will be capable of operating at cold plate temperature excursions up to 200ºC, which presents an opportunity to reject heat through the aircraft skin to the ambient using passive cooling. In addition, the actuation system rejects heat continuously at a rate of $Q$ = 500 W ($q$ = 3 W/cm$^2$) and has transient heat rejection rates of $Q$ = 5000 W over a period of one second. Possible thermal management scenarios include direct connection of the electronics package to the skin, high-thermal conductivity graphite straps, or the use of a loop heat pipe between the package and the skin to provide mounting flexibility. The objective of this analysis is to determine the external heat transfer possibilities of the aircraft skin. The heat flux and heat transfer coefficient have been found as functions of the skin and ambient temperatures, the altitude, and airspeed.

### 1.3. Mathematical Model

The temperature and density of air vary considerably with altitude and also vary day-to-day depending on weather conditions. In order to be conservative in the calculation of heat transfer coefficients, data for the highest temperature recorded with a frequency-of-occurrence of 1% were used to generate equations for temperature and density versus altitude (DOD, 1997) as shown in Figure 1.1 and Table 1.1. Also presented are data for the lowest temperature recorded with a frequency-of-occurrence of 1% (DOD, 1997) and data for the "standard atmosphere" (Anderson, 2000).

The film temperature was used as the reference temperature to evaluate the air properties (White, 1988)

$$T^* = T_\infty(0.5 + 0.039\mathrm{Ma}_\infty^2) + 0.5T_\mathrm{w} \tag{1.1}$$

The air density at the film temperature and at altitude was evaluated using the perfect gas law

$$\rho^* = \rho_\infty\left(\frac{T_\infty}{T^*}\right) \tag{1.2}$$

The freestream speed of sound is

$$a_\infty = \sqrt{\gamma R T_\infty} \tag{1.3}$$

The freestream velocity is

$$U_\infty = \mathrm{Ma}_\infty a_\infty \tag{1.4}$$

The absolute viscosity of air is given by the following relation (NACA, 1953)

$$\mu = \mu_\mathrm{R}\left(\frac{T}{T_\mathrm{R}}\right)^{0.76} \tag{1.5}$$

where $\mu_\mathrm{R}$ is a reference viscosity evaluated at a known reference temperature $T_\mathrm{R}$.

The Reynolds number for a plate of length $L$ is determined by evaluating the properties of air at the freestream condition.

$$\mathrm{Re}_\mathrm{L} = \frac{\rho_\infty U_\infty L}{\mu_\infty} \tag{1.6}$$

Regression equations for the specific heat and Prandtl number were determined as functions of temperature using data from Incropera and DeWitt (2002), as shown in Table 1.2.

The adiabatic wall temperature is (White, 1988)

$$T_{\mathrm{aw}} = T_{\infty}\left[1 + r\left(\frac{\gamma - 1}{2}\right)\mathrm{Ma}_{\infty}^{2}\right] \tag{1.7}$$

where the recovery factor is

$$r = \begin{cases} \mathrm{Pr}^{1/2} \text{ for laminar flow} \\ \mathrm{Pr}^{1/3} \text{ for turbulent flow} \end{cases} \tag{1.8}$$

For the purposes of this analysis, Reynolds numbers less than 500,000 were considered to be laminar, greater than 500,000 were turbulent. The local skin friction coefficient at the end of the plate was found by evaluating the air properties at the film temperature. For laminar flow, the skin friction coefficient is given by (White, 1988)

$$C_{\mathrm{f,L}}^{*} = \frac{0.664}{\left(\frac{\rho^{*}U_{\infty}L}{\mu^{*}}\right)^{1/2}} \tag{1.9}$$

and for turbulent flow

$$C_{\mathrm{f,L}}^{*} = \frac{0.455}{\ln^{2}\left(\frac{0.06\rho^{*}U_{\infty}L}{\mu^{*}}\right)} \tag{1.10}$$

The local Stanton number at the end of the plate for laminar flow is given by (White, 1988)

$$\mathrm{St}_{\mathrm{L}}^{*} = 0.332\mathrm{Re}_{\mathrm{L}}^{1/2}\mathrm{Pr}^{-2/3} \tag{1.11}$$

and for turbulent flow

$$\mathrm{St}_{\mathrm{L}}^{*} = \frac{h_{\mathrm{L}}}{\rho^{*}U_{\infty}C_{\mathrm{p}}^{*}} = \frac{C_{\mathrm{f,L}}^{2}/2}{1 + 12.7(\mathrm{Pr}^{*2/3} - 1)\left(C_{\mathrm{f,L}}^{*}/2\right)^{1/2}} \tag{1.12}$$

The local heat transfer coefficient at the end of the plate is

$$h_{\mathrm{L}} = \mathrm{St}_{\mathrm{L}}^{*}\rho^{*}U_{\infty}C_{\mathrm{p}}^{*} \tag{1.13}$$

The local heat transfer coefficient was calculated using the appropriate skin friction coefficient and Stanton number based on laminar or turbulent flow. The average heat transfer coefficient over the length of the plate is approximated by (White, 1988)

$$\bar{h} = 1.15 h_{\mathrm{L}} \tag{1.14}$$

The heat flux dissipated over the plate, both local and average, is defined in terms of the adiabatic wall temperature (White, 1988)

$$q_{\mathrm{w}} = h(T_{\mathrm{w}} - T_{\mathrm{aw}}) \tag{1.15}$$

Thermal radiation was neglected in this analysis as it contributed less than 1.6% to the total heat rejected from the plate surface.

### 1.4. Results and Discussion

The adiabatic wall temperature is shown in Figure 1.2 as a function of altitude and Mach number. The overall trend of the adiabatic wall temperature with altitude follows the freestream air temperature in Figure 1.1 and increases with Mach number as expected. Figure 1.3 presents the temperature difference, $\Delta T = (T_{\mathrm{aw}} - T_{\infty})$, versus altitude. This temperature difference demonstrates the increase in the adiabatic wall temperature over the freestream due to aerodynamic heating. The temperature difference $\Delta T = (T_{\mathrm{w}} - T_{\mathrm{aw}})$ is given in Figure 1.4. Of interest is the portion of the curves in which this difference is negative, which indicates that heat is transferred from the air to the aircraft skin. The maximum Mach number achievable before heat is transferred from the air to the skin is given by

$$\mathrm{Ma}_{\infty,\mathrm{max}} = \left[\frac{1}{r}\left(\frac{T_{\mathrm{w}}}{T_{\infty}} - 1\right)\left(\frac{2}{\gamma - 1}\right)\right]^{1/2} \tag{1.16}$$

and is plotted in Figure 1.5 over a range of wall temperatures. The maximum Mach number increases with altitude and wall temperature up to a maximum at approximately 18 km. In Figure 1.6, the average convective heat transfer coefficient decreases monotonically with altitude due to the continual decrease in the air density. In general, the convective heat transfer coefficient increases with Mach number, as expected. The average heat flux dissipated from the plate is shown in Figure 1.7. For low Mach numbers, the heat flux is positive for all values of altitude, which indicates that heat is

transferred from the aircraft skin to the air. At high Mach numbers, however, the heat flux is negative at low altitudes due to the negative $\Delta T$ as shown in Figure 1.4. This means that the adiabatic wall temperature is higher than the skin temperature due to aerodynamic heating effects. The effect of heated plate length on the local heat flux for $H$ = 0, 10, and 20 km is shown in Figure 1.8. The local heat flux starts low and decreases in the laminar region of the plate, and then increases as the flow transitions to turbulent where it once again decreases. In general, the average heat flux follows the behavior of the local heat transfer coefficient, where $h_L$ is high at the leading edge and at the beginning of turbulent flow and decreases as the boundary layer grows. One item to note is that Figure 1.9 shows the average heat flux dissipated over the plate versus altitude for the 1% hot day, the 1% cold day, and the standard atmosphere data as presented in Figure 1.1. At low altitudes, $q_w$ is significantly higher for the 1% cold day due to the combined effects of the lower atmospheric temperature and the higher air density. The effect of wall temperature on average heat flux for a given airspeed is shown in Figure 1.10. The heat flux increases dramatically with altitude and wall temperature for low altitudes.

### 1.5. Conclusions

An analysis of the heat transfer from a heated plate has provided important insights for the possible use of the aircraft skin to reject heat from electric actuator systems. It was found that the altitude and speed of the aircraft significantly affected the amount of heat that could be rejected from the skin. Aerodynamic heating of the skin reduced the heat transfer, and if the Mach number was high enough, heat transfer from the skin to the air went to zero. A performance map of this phenomenon was provided. The altitude of the aircraft affected the freestream temperature and density, which in turn affected the overall heat transfer coefficient. It was also shown that the assumption of a "standard atmosphere" could result in significant errors in the prediction of the heat dissipation as compared to the data for the 1% hot day or the 1% cold day. The analysis showed that the aircraft skin temperature, which is directly influenced by the actuator thermal management system, has a strong effect on the heat dissipation rate, especially at low altitudes.

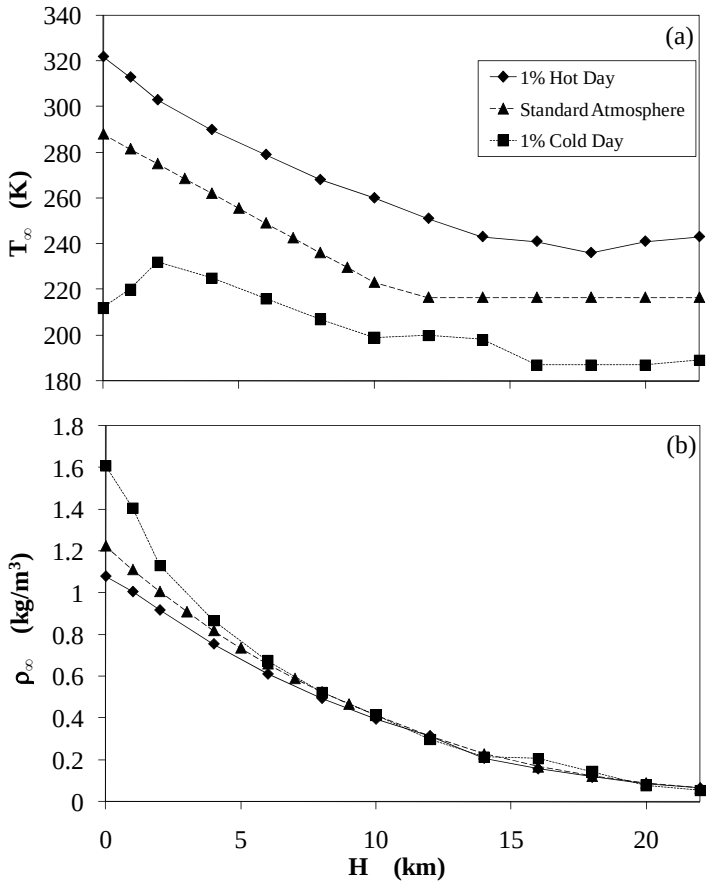


Figure 1.1. Comparison of atmospheric properties versus altitude: (a) Temperature; (b) Density (DOD, 1997; Anderson, 2000).

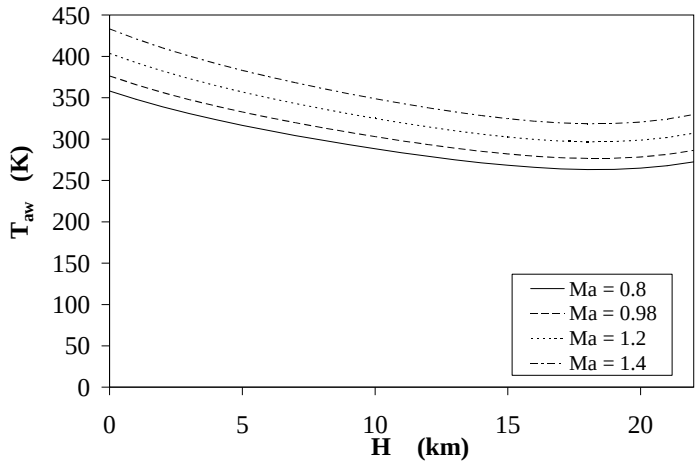


Figure 1.2. Adiabatic wall temperature versus altitude for various Mach numbers (1% hot day).

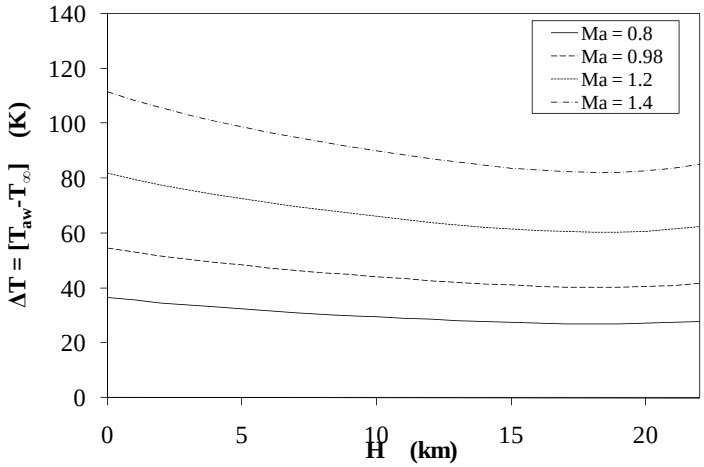


Figure 1.3. Temperature difference $(T_{aw} - T_\infty)$ versus altitude for various Mach numbers (1% hot day).

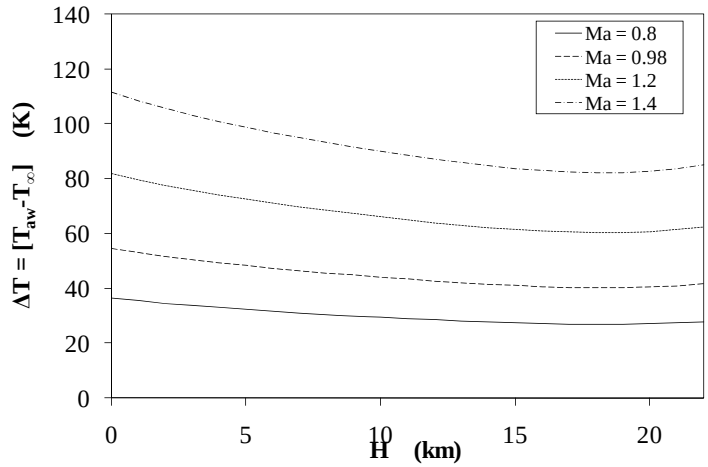


Figure 1.4. Temperature difference $(T_w - T_{aw})$ versus altitude for various Mach numbers ($T_w$ = 135ºC, 1% hot day).

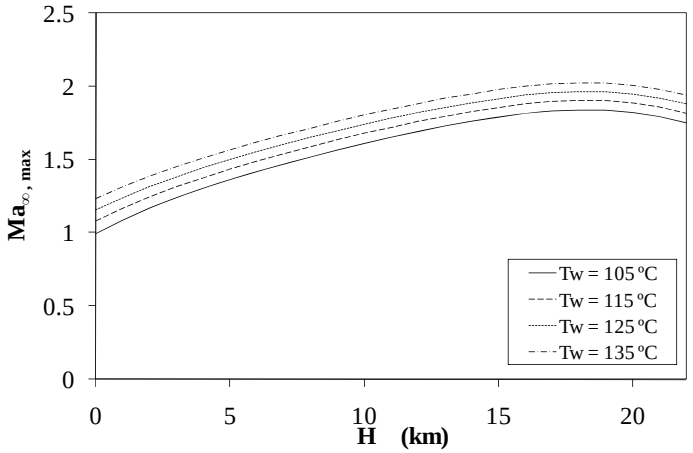


Figure 1.5. Maximum Mach number before heat is transferred from the air to the skin versus altitude for various wall temperatures (1% hot day).

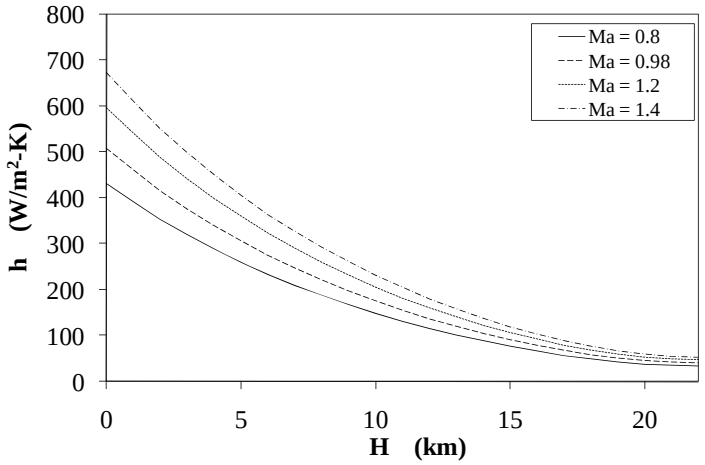


Figure 1.6. Average convective heat transfer coefficient versus altitude for various Mach numbers ($T_w$ = 135ºC, $L$ = 1.0 m, 1% hot day).

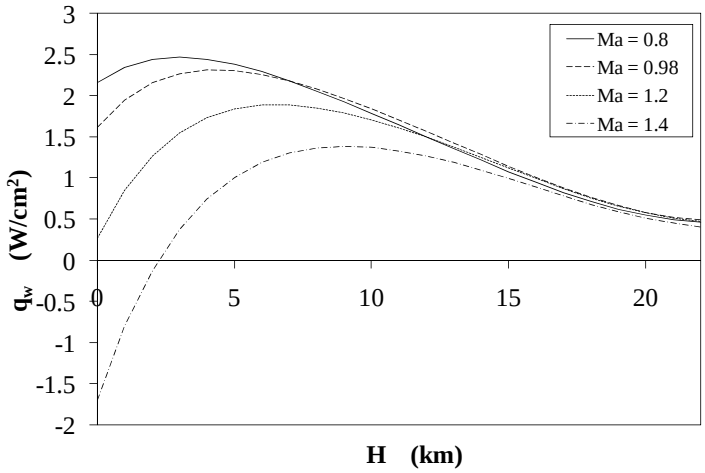


Figure 1.7. Average heat flux dissipated over the plate versus altitude for various Mach numbers ($T_w$ = 135ºC, $L$ = 1.0 m, 1% hot day).

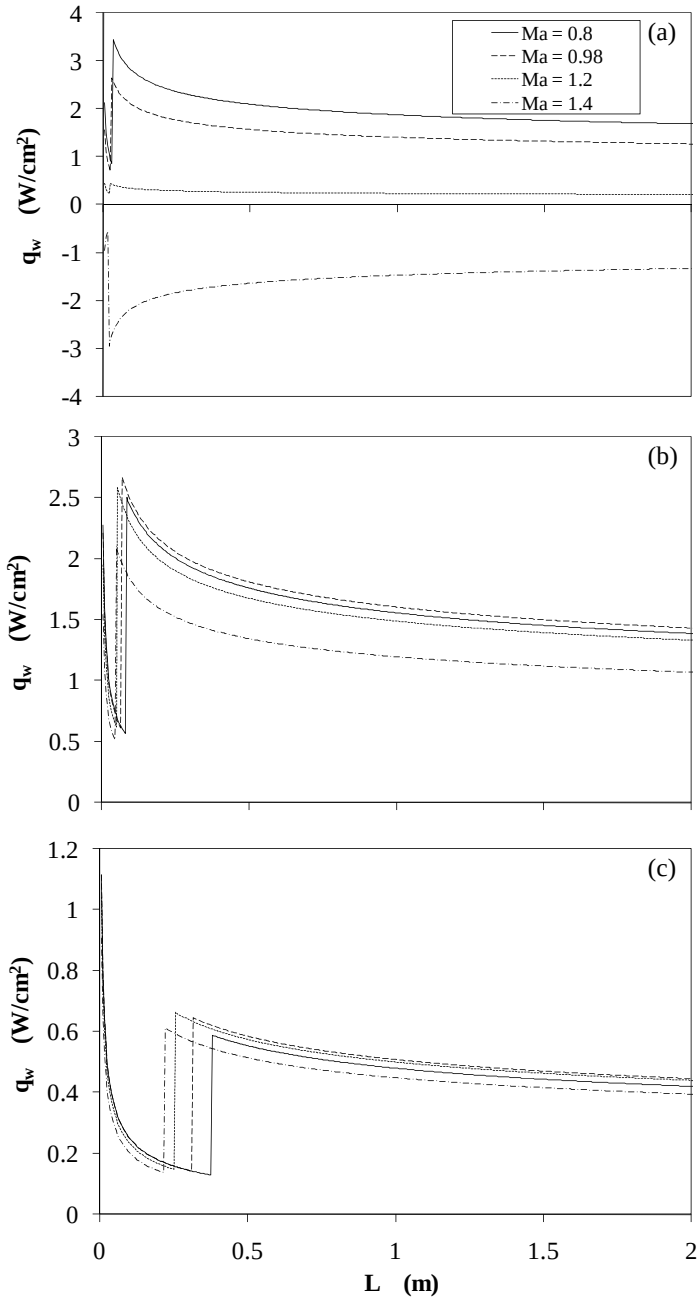


Figure 1.8. Local heat flux dissipated over the plate versus plate length for various Mach numbers ($T_w$ = 135ºC, 1% hot day): (a) $H$ = 0 km; (b) $H$ = 10 km; (c) $H$ = 20 km.

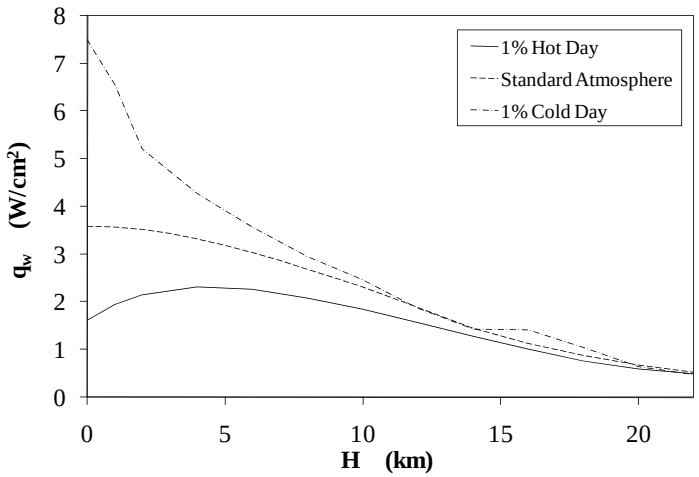


Figure 1.9. Average heat flux dissipated over the plate versus altitude for various atmospheric conditions ($T_w$ = 135ºC, $L$ = 1.0 m, $Ma_\infty$ = 0.98) (DOD, 1997; Anderson, 2000).

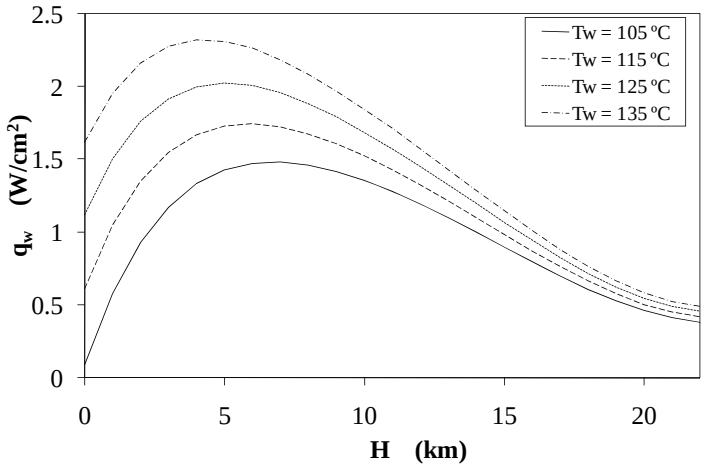


Figure 1.10. Average heat flux dissipation versus altitude for various wall temperatures ($Ma_\infty$ = 0.98, $L$ = 1.0 m, 1% hot day).

Table 1.1. Regression equations for air properties versus altitude for 1% hot (DOD, 1997).

$$y = a_0 + a_1 H + a_2 H^2 + a_3 H^3 + a_4 H^4$$
($H$ in km)

| Property | $a_0$ | $a_1$ | $a_2$ | $a_3$ | $a_4$ | $R^2$ |
|---|---|---|---|---|---|---|
| $T_\infty$ (ºC) | 4.8507E+1 | -9.5033E+0 | 5.3483E-1 | -2.8994E-2 | 7.7664E-4 | 0.99779 |
| $\rho_\infty$ (kg/m$^3$) | 1.0868E+0 | -8.9917E-2 | 2.0898E-3 | -4.9336E-6 | — | 0.99954 |

Table 1.2. Regression equations for air properties versus temperature (Incropera and DeWitt, 2002).

$$y = a_0 + a_1 T + a_2 T^2 + a_3 T^3$$
($T$ in K)

| Property | $a_0$ | $a_1$ | $a_2$ | $A_3$ | $R^2$ |
|---|---|---|---|---|---|
| $c_p$ (J/kg-K) | 1.0187E+3 | -6.9921E-2 | -3.3333E-5 | 4.4444E-7 | 0.99916 |
| Pr | 8.6418E-1 | -9.4177E-4 | 1.7778E-6 | -1.2593E-9 | 0.99725 |

## 2. TITANIUM-WATER LOOP HEAT PIPE CHARACTERISTICS UNDER STATIONARY AND ELEVATED ACCELERATION FIELDS

### 2.1. Abstract

An experiment has been developed to examine operating characteristics of a titanium-water loop heat pipe (LHP) under stationary and elevated acceleration fields. The LHP was mounted on a 2.44 m diameter centrifuge table on edge with heat applied to the evaporator via a mica heater and heat rejected using a high-temperature polyalphaolefin coolant loop. The LHP was tested under the following parametric ranges: heat load at the evaporator: $100 \leq Q_{in} \leq 600$ W; heat load at the compensation chamber: $0 \leq Q_{cc} \leq 50$ W; radial acceleration: $0 \leq a_r \leq 10$ g. For stationary operation ($a_z$ = 1.0 g, $a_r$ = 0 g), the LHP evaporative heat transfer coefficient decreased monotonically, thermal resistance decreased to a minimum then increased, and wall superheat increased monotonically. Heat input to the compensation chamber was found to increase the evaporative heat transfer coefficient and decrease thermal resistance for $Q_{in}$ = 500 W. Flow reversal in the LHP was found for some cases, which was likely due to vapor bubble formation in the primary wick. Operating the LHP in an elevated acceleration environment revealed dry-out conditions from $Q_{in}$ = 100 to 400 W and varying accelerations and the ability for the LHP to reprime after an acceleration event that induced dry-out. Evaporative heat transfer coefficient and thermal resistance was found not to be significantly dependent on radial acceleration. However, wall superheat was found to increase slightly with radial acceleration.

### 2.2. Introduction

Loop heat pipes (LHP's) are two-phase thermal transport devices that operate passively using the latent heat of vaporization to transport heat from one location to another. The LHP was invented in 1972 by Gerasimov and Maidanik (Maidanik, 2005) in the former Soviet Union, and was later patented in the United States (Maidanik et al., 1985). The LHP consists of an evaporator, compensation chamber, liquid and vapor

transport lines made of smooth tubing, and a condenser as shown in Figure 2.1. Heat is applied directly to the exterior wall of the evaporator, which often has a circular cross-section. The majority of the input heat is used to vaporize the working fluid within the primary wick structure, which is an inverted meniscus wick in direct contact with the exterior evaporator wall. The vapor is captured in the axial vapor grooves in the primary wick and is directed via a manifold at the end of the evaporator to the vapor line due to the increased pressure within the evaporator. Due to evaporation, menisci are developed in the primary wick which establishes a capillary pressure head that returns liquid to the evaporator from the condenser. This capillary head must be greater than the total system pressure drop in order for the LHP to continue to operate without drying out.

The vapor from the evaporator section travels via the vapor line to the condenser section, which is also made of smooth tubing. Heat is rejected from the condenser to the ultimate heat sink. The working fluid enters the condenser as a superheated vapor. After sufficient heat is rejected, the vapor becomes a saturated vapor, a two-phase mixture, a saturated liquid, and, depending on the amount of heat rejection, it may or may not become a subcooled liquid. The location of the point at which the working fluid becomes a subcooled liquid ($2\varphi$-$1\varphi$) is dependent on the heat input at the evaporator, the heat rejection at the condenser, and the saturation temperature in the compensation chamber. After exiting the condenser section, the liquid will continue to lose heat due to convection and/or thermal radiation to the ambient. The subcooled liquid returns to the evaporator via the bayonet tube, which delivers the liquid to the end of the evaporator where the vapor manifold resides.

As stated previously, most of the evaporator heat input evaporates liquid in the primary wick. The rest of the heat is transferred by conduction through the primary wick, where liquid is evaporated into vapor channels leading to the compensation chamber (Figure 2.2). Part of this vapor stream condenses onto the secondary wick, which is in intimate contact with the bayonet tube. This heat transfer to the bayonet tube raises the temperature of the subcooled liquid entering the compensation chamber to the saturation temperature as it travels to the end of the evaporator. The rest of the vapor condenses onto the wick lining the compensation chamber. This latent heat is then rejected from the compensation chamber to the ambient. The condensate in the compensation chamber is

drawn back to the evaporator section through the secondary wick by capillary action. In this way, the secondary wick and the compensation chamber behave similar to a conventional heat pipe.

The compensation chamber allows the LHP to automatically regulate itself during transient situations like startup, shutdown, or a change in the operating conditions. The compensation chamber provides for storage of excess liquid when the evaporator heat input is high, where the majority of the condenser section is free of subcooled liquid. The compensation chamber can also be used to control the location of the 2φ-1φ point in the condenser. Controlling the heat transfer through the shell of the compensation chamber can adjust the saturation point in the condenser, thereby changing the amount of subcooling of the liquid returning to the evaporator.

There has been limited experimentation on the acceleration effects on loop heat pipes and heat pipes. Ku et al. (2000a) performed experiments on a miniature aluminum/anhydrous ammonia LHP by using a spin table to examine the effects of varying acceleration on start-up. Four mounting configurations were examined: (1) horizontally with the compensation chamber and liquid line outboard on the table, (2) horizontally with the evaporator and vapor line outboard on the table, (3) vertically with evaporator above the compensation chamber with no radial acceleration, and (4) vertically with evaporator below the compensation chamber with no radial acceleration. Several different experiments were conducted, including LHP startup before acceleration was applied and vice versa, as well as varying heat load inputs up to $Q_{in}$ = 100 W. Several acceleration profiles were examined, including $a_r$ = 0.0 g, constant $a_r$ = 1.2 g, constant $a_r$ = 4.8 g, combination of constant $a_r$ = 1.2 and 4.8 g, constant $a_r$ = 1.2 g for 30 seconds followed by $a_r$ = 0.0 g for 300 seconds periodically, constant $a_r$ = 4.8 g for 30 seconds followed by $a_r$ = 0.0 g for 300 seconds periodically, and combinations of $a_r$ =1.2 and 4.8 g followed by $a_r$ = 0.0 g for 300 seconds periodically. Their experimental results indicated that the wall superheat, defined as the difference between the evaporator and compensation chamber wall temperatures, appeared to be independent of input heat load and acceleration. When temperature overshoot in the evaporator was examined, for heat loads greater than $Q_{in}$ = 50 W, there was essentially no overshoot. For smaller heat loads, such as at $Q_{in}$ = 5 W, a temperature overshoot of a few degrees was always observed, but

at $Q_{in}$ = 25 W, the temperature overshoot ranged from 0 to 45°C. In every experiment, the LHP started successfully.

Ku et al. (2000b), in an extension of the previous experimental study, examined the temperature stability of the same miniature LHP under varying heat loads and acceleration levels. Their experimental results showed that the radial acceleration caused a redistribution of fluid in the evaporator, condenser, and compensation chamber. This in turn changed the LHP operating temperature. The effect was not universal, in the sense that all the operating conditions needed to be taken into account. With sufficient time, constant acceleration could either increase or decrease the LHP operating temperature. Periodic acceleration led to a quasi-steady operating temperature. Temperature hysteresis could also be caused by the radial acceleration. In all of the experiments the LHP continued to operate without problems.

Similar research has been conducted to examine body force effects on heat pipes. Ponnappan et al. (1992) examined a flexible copper-water arterial wick heat pipe subjected to transverse acceleration using a centrifuge table. Evaporator heat loads up to $Q_{in}$ = 150 W and steady state radial accelerations up to $a_r$ = 10.0 g were investigated. Transport capacity of the heat pipe dropped from $Q_{out}$ = 138 W at radial accelerations of $a_r$ = 1.0 g to $Q_{out}$ = 60 W at $a_r$ = 10.0 g. The temperature difference between the evaporator and condenser remained fairly constant up to $a_r$ = 4 g then decreased from $a_r$ = 4 to 10 g. This decrease was due to a more uniform distribution of fluid within the wick at the higher radial acceleration.

Yerkes and Beam (1992) examined the same flexible copper-water arterial wick heat pipe as Ponnappan et al. under transient transverse and axial acceleration forces with periodic and burst transverse accelerations from $f$ = 0.01 to 0.03 Hz and magnitudes from $a_r$ = 1.1 to 9.8 g peak-to-peak and evaporator heat inputs up to $Q_{in}$ = 83 W. It was observed that pooling of excess fluid had a significant effect on the heat transport of the heat pipe at steady state transverse acceleration. Heat transport potential decreased with increasing transverse acceleration causing partial dry-out of the artery and pooling in the condenser. The heat pipe was able to reprime after dry-out events with subsequent reduction of transverse acceleration. Under cyclic transverse acceleration, significant fluid slosh was thought to create a cyclic variation in heat pipe temperature. Temperature

rise was lower at the onset of dry-out conditions when compared to steady state transverse acceleration. Frequency of the steady periodic burst transverse acceleration had no effect on the heat pipe temperature and tended to delay the onset of dry-out.

Thomas and Yerkes (1996) examined the same flexible copper-water arterial wick heat pipe as Ponnappan et al. with evaporator heat loads from $Q_{in}$ = 75 to 150 W, condenser temperatures of $T_c$ = 3, 20, and 35°C, and sinusoidal acceleration frequencies of $f$ = 0, 0.01, 0.05, 0.1, 0.15, and 0.2 Hz. The amplitude of the radial acceleration ranged from $a_r$ = 1.1 to 9.8 g. The effects of the previous dry-out history of the heat pipe were also examined. It was discovered that the thermal resistance increased and then decreased with respect to increasing acceleration frequency. The thermal resistance also increased with increasing evaporator heat loads. The previous dry-out history adversely affected the thermal resistance of the heat pipe when dry-out occurred prior to increasing the acceleration frequency.

Thomas et al. (1998) examined a helically grooved copper-ethanol heat pipe as a function of evaporator heat input and transverse radial acceleration. Heat loads ranging from $Q_{in}$ = 20 to 250 W were applied to the evaporator. At $Q_{in}$ = 20 W the heat pipe did not experience any dry-out conditions when the radial acceleration was increased and then decreased stepwise from $a_r$ = 0 to 10 g. At $Q_{in}$ = 50 W, the heat pipe experienced dry-out conditions at $a_r$ = 0 and 2 g, but quickly reprimed at the higher radial accelerations. This indicated the elevated body forces actually aided the performance of the heat pipe by increasing the capillary limit due to the forces generated from acceleration gradients down the length of the helical groove. The thermal resistance of the heat pipe was noted to decrease then increase with increasing heat transported when dry-out started.

Zaghdoudi and Sarno (2001) examined the body force effects on a flat copper-water heat pipe via a centrifuge setup. The heat pipe was mounted such that the accelerating forces were opposite to the liquid flow, or in an “unfavorable” mounting condition. Three types of accelerations were performed in this study: A parabolic profile from $a_r$ = 0 to 10 to 0 g with a 5 second stabilization at $a_r$ = 10 g, a step increase from $a_r$ = 0 to 10 to 0 g with a 10 second stabilization at each step, and increasing then decreasing the acceleration from $a_r$ = 0 to 10 g after thermal stabilization. Heat loads of $Q_{in}$ = 20, 40,

and 60 W were applied to examine the effect on evaporator and condenser temperature as well as thermal resistance. For the first two types of acceleration profile, it was observed there was a delayed increase in evaporator temperature and decrease in condenser temperature. This was likely due to the pooling of fluid in the condenser. Thermal resistance also experienced a delayed increase in onset and remained elevated even in the absence of an accelerating force. For the third type of acceleration profile, there was a much more gradual increase in evaporator temperature and nearly negligible decrease in condenser temperature, quickly returning to normal in the absence of the accelerating force. Thermal resistance had a similar trend, quickly returning to normal after the acceleration burst. This suggested that the heat pipe quickly reprimed after the acceleration event. These tests demonstrated the importance of prior operation history when the heat pipe was subjected to elevated body forces.

The objective of the present experiment was to determine the operating characteristics of a titanium-water loop heat pipe subjected to varying heat loads and accelerations. Transient temperature distributions, the evaporative heat transfer coefficient, and the thermal resistance have been found in terms of the heat input at the evaporator, heat input at the compensation chamber, and radial acceleration field. In addition, the transient behavior during startup and steady operation has been examined. A performance map has been developed that relates dry-out to the heat load and radial acceleration for the experimental conditions described. The experimental parametric ranges were as follows: heat load at the evaporator: $100 \leq Q_{in} \leq 600$ W; heat load at the compensation chamber: $0 \leq Q_{cc} \leq 50$ W; radial acceleration: $0 \leq a_r \leq 10$ g.

### 2.3. Experimental Setup

The Centrifuge Table Test Bed at Wright-Patterson Air Force Base (AFRL/RZPS) was used to determine the heat transfer characteristics of the titanium-water LHP under stationary and elevated acceleration fields. A schematic of this test bed can be seen in Figure 2.3. The test bed consisted of a 2.44 m diameter horizontal rotating table driven by a 20 hp DC electric motor. The test bed was able to deliver the following to devices mounted to the rotating table: Conditioned DC electrical power through three separate power supplies, 120 VAC power, temperature-controlled ethylene glycol coolant, and electrical signals for analog or digital control. In addition, electrical signals were

collected from instruments on the table and stored in a data acquisition computer. The radial acceleration could exceed $a_r$ = 12 g, with a maximum onset of approximately $\dot{a}_r$ = 10 g/s, inducing a tangential acceleration. The acceleration field could be varied manually using a potentiometer, or controlled digitally using a signal generator in the data acquisition system. The acceleration field was measured using an orthogonal triaxial accelerometer (Columbia SA-307HPTX) with an uncertainty of ± 0.01 g.

Power was supplied to heaters on the table by three precision power supplies (Kepco ATE150-7M, Kepco ATE150-3.5M, and HP 6290A) through power slip rings. These slip rings were separated from the instrumentation slip rings to reduce electrical noise. The heater power was calculated by multiplying the voltage drop across the heater by the current. The current was determined from the voltage drop across a precision resistor in series with the heater. This type of measurement was required due to the voltage drop between the control room and the table. The uncertainty in this measurement was less than 2.0%

Heat was rejected from the centrifuge table using an ethylene-glycol/water mixture that was delivered to the rotating centrifuge table via a double-pass hydraulic rotary coupling (Deublin 1690-000-115). The temperature of the coolant was maintained at a constant setting by a recirculating chiller (Neslab HX-300). The volumetric flow rate of the coolant mixture was controlled using a high-pressure booster pump, which aided the low-pressure pump in the recirculating chiller. Throughout experimentation the flow rate was held constant at $\dot{V}_{eg}$ = 2.4 L/min.

Instrumentation signals generated on the table were acquired through a custom-built forty-channel instrumentation slip ring using a data acquisition system. Temperatures, mass flow rates, accelerations, and voltages were all measured using a data acquisition mainframe (Agilent VXI E8408A) with a command module (Agilent E1406A), 5½ digit multimeter module (Agilent E1411B), and a 64-channel 3-wire multiplexer module (Agilent E1476A). The rotational speed of the centrifuge table, heater power, and other low voltage control devices on the table were controlled using an 8/16-channel D/A converter module (Agilent E1418A). Communication between the data acquisition unit and the computer was established using a general purpose interface bus (GPIB) coupled with a custom-designed LabVIEW virtual instrument.

Gathering temperature data from rotating machinery using slip rings presents unique problems. First, when the thermocouple wires are connected to the wires leading to a slip ring, at least one extra junction is created, depending on the materials of the thermocouple wires. To avoid this problem, a Type E thermocouple amplifier was installed on the centrifuge table (Omega OM7-47-E-07-2-C) with internal cold junction compensation. This converted the millivoltage signals from the thermocouples to 0 to 10 V signals without the creation of extra junctions. Another problem that is present when slip rings are used is electrical noise. This problem was reduced (not eliminated) by the use of a low-pass filter for each of the thermocouple signals coming from the table before the data acquisition system.

The test article, a titanium-water loop heat pipe, was developed for AFRL/RZPS by Advanced Cooling Technologies (ACT), Inc., in Lancaster, PA, under contract FA8601-06-P-0076. Initial design parameters set by AFRL/RZPS were to develop a loop heat pipe capable of a minimum heat load of 500 W and minimum heat flux of 3 W/cm$^2$. The minimum transport line length was 2 m to simulate relevant aircraft geometries. An evaporator operating temperature of 200°C and condenser operating temperature between 5 and 140°C were selected to match relevant acquisition and rejection temperatures aboard aircraft. The evaporator and condenser dimensions were selected to be 20.32 × 10.16 cm and 30.48 × 28.56 cm, respectively, to match commercial off-the-shelf heaters and cold plates. A summary of the requested design parameters can be seen in Table 2.1. After several design iterations, ACT delivered the loop heat pipe shown in Figure 2.4. A summary of the loop heat pipe specifications can be seen in Table 2.2. The LHP was instrumented with twelve type E exposed tip thermocouples as seen in Figure 2.5. A summary of their locations can be seen in Table 2.3.

The loop heat pipe was mounted onto the centrifuge table such that the centerline of the tubing coincided with the outer table radius as much as possible. Small deviations existed since the condenser section and the evaporator/compensation chamber were both straight. This induced a non-uniform radial acceleration field over the lengths of these sections that needed to be quantified. Stands were designed using G-7 phenolic to mount the loop heat pipe with support at the compensation chamber, evaporator, condenser, and transport lines (Figure 2.6). The tops of these stands were anchored to the table to reduce

deflection when the table was rotating. A survey was taken at 22 locations on the loop heat pipe to determine how far various portions of the loop heat pipe were from the centerline radius. The loop heat pipe had a minimum radius to centerline of 119.2 cm and a maximum radius to centerline of 123.3 cm. The entire loop heat pipe fitted within 4.6 cm for a percent acceleration difference of 3.8%. Complete survey data can be seen in Appendix D. To minimize heat loss to the environment, the entire assembly was thoroughly insulated using Kaowool blankets and aluminum foil. The assembly was placed inside an aluminum frame (80/20, Inc.) for structural support and enclosed with sheet metal sides to minimize convective heat losses.

During operation, heat was applied to the LHP at the evaporator while the heat transfer to the compensation chamber was independently controlled. A mica heater (Minco) was located between the evaporator body and a ceramic fiber insulative layer, followed by the evaporator stand. A flexible electric heat tape (Thermolyne) was wound around the compensation chamber and surrounded by Kaowool insulation and aluminum foil to minimize heat losses. In normal operation, the compensation chamber is not insulated and the temperature is closely controlled during operation. For these experiments, insulating the LHP, including the compensation chamber, was selected to mimic a typical configuration of a LHP in an aircraft environment where bay temperatures could be higher than the LHP temperatures. This would minimize parasitic heat gain, and reduce the use of external heaters or coolers on the compensation chamber. As a result, the LHP compensation chamber was allowed to “float” into equilibrium with the evaporator and condenser, rather than controlling the temperature of the evaporator by controlling the compensation chamber temperature.

As previously mentioned, the centrifuge table was equipped with an on-board fluid loop for dissipating heat from sources on the table, which used ethylene glycol as its working fluid. In the present experiment, it was desired to have the option of operating the LHP condenser section at elevated temperatures, so a high-temperature fluid loop was constructed and mounted to the centrifuge table to act as an interface between the LHP and the low-temperature fluid loop, as shown in Figure 2.7. The high-temperature working fluid (Brayco Micronic 889 polyalphaolefin or PAO oil) flowed from the custom-made copper reservoir into a positive displacement gear pump (Tuthill). After

passing through a filter and a flow-straightening section, the PAO was directed through the turbine flow meter (Omega FTB-9506). An electrical tape heater was mounted to the copper tubing after the flow meter to allow for preheating the PAO prior to reaching the calorimeter on the condenser section, which consisted of three heat exchangers plumbed in series and mounted to the condenser section. Type E thermocouple probes were installed at the inlet and outlet of the three heat exchangers for calorimetry (TC00 and TC01), and another was placed prior to the flow meter (TC03). This was needed due to the dependence of the viscosity of PAO on temperature. After the PAO exited the three heat exchangers on the condenser, it flowed to a liquid/liquid heat exchanger that transferred heat from the high-temperature coolant loop to the low-temperature ethylene glycol loop. The PAO then returned to the reservoir.

Four grounded probe thermocouples for the high temperature loop and twelve exposed tip type E thermocouples mounted on the LHP were used in the experiment. Thermocouple calibrations were conducted over two temperature ranges depending on the anticipated operating temperatures. The grounded probe thermocouples were used for calorimetry, coolant flow meter calibration and the measurement of the ambient temperature, where the error needed to be minimized. These four thermocouples were calibrated over the anticipated range of 20 to 145°C in 5°C intervals. The twelve exposed tip thermocouples were mounted on the LHP in various locations and needed to be calibrated over the full range of 20 to 230°C in 5°C increments. The calibration procedure consisted of using two separate recirculating chiller baths (Brinkmann Lauda RCS 20-D, $T$ = 20 to 140°C; Hart Scientific 6330, $T$ = 40 to 230°C) with PAO as the working fluid to achieve the required temperature range. The temperature readings from the sixteen thermocouples were compared to a NIST-traceable platinum resistance temperature detector (Hart Scientific RTD 1502A) with a resolution of ± 0.009°C. To ensure that the bath had reached steady state at a given temperature, the RTD temperature was continuously monitored. When the standard deviation of 100 readings dropped below the specified threshold of 0.005°C, 100 readings from the thermocouples were sampled, stored in an array, and the bath temperature was changed. For repeatability, the bath temperature was first incremented from the lowest temperature to the highest temperature, and then decremented from highest to lowest, and the two sets of 100 data

points collected for each thermocouple at a given temperature were used to determine two average readings. Plots of the RTD temperature versus each thermocouple temperature were generated, and polynomial trend lines were fitted for each thermocouple as can be seen in Appendix C. A fifth-order polynomial was selected since it reduced the maximum deviation from the data by approximately a factor of four over a first-order trend line. The uncertainty associated with each thermocouple was determined by accounting for four sources of error: the stated uncertainty of the RTD, the confidence interval of the RTD average reading at a confidence level of 0.95, the confidence interval of the thermocouple average reading at a confidence level of 0.95, and the maximum deviation of the temperature calculated using the polynomial curve fit from the actual measured temperature.

The turbine flow meter used in the high-temperature fluid loop was calibrated to achieve accurate results for the amount of heat extracted from the LHP. This was critical for the calculation of the evaporative heat transfer coefficient and the thermal resistance of the LHP. Since the viscosity of the PAO, used in the high-temperature fluid loop, changes significantly with temperature, a “calibration surface” was generated that related the output voltage of the flow meter and the temperature of the PAO at the entrance of the flow meter to the mass flow rate. The calibration setup consisted of a recirculating chiller bath (Brinkmann Lauda RCS 20-D) filled with PAO from the same source as used in the high-temperature fluid loop. The gear pump, inline filter (Whitey SS56S6 140 micron) and a calibrated grounded thermocouple probe, from the high-temperature fluid loop, were installed in a line from the bath to the turbine flow meter (Omega FTB-9506) and signal conditioner (Omega FLSC-61). Flow straightening sections upstream and downstream were placed according to the manufacturer's instructions. A three-way valve was installed after the flow meter, which allowed the entire flow system to reach a steady temperature. Once the temperature was steady, the flow was diverted to a catch basin for a specified amount of time. The voltage from the flow meter and the temperature from the thermocouple were recorded during this time, and when the basin was full, the flow was again diverted to recirculating the PAO back to the chiller bath. All of the data was collected through the instrumentation slip rings on the centrifuge table to the data acquisition system to capture all errors inherent to the centrifuge table test bed. A lab

scale (Mettler PC4400) was used to determine the mass collected during a given test run to within ± 0.3 gm. During each measurement, as many data points as possible were collected across the time span with the limiting factor being the iteration time on the LabVIEW software. The minimum number of data points collected for any given run was 437. The voltages and temperatures were averaged and a confidence interval was calculated based on a confidence level of 0.95 for each test run. The test was repeated for a total of five averaged data points for each nominal temperature and flow rate. These tests were completed over the range of $T$ = 20 to 120°C in intervals of 25°C and flow rates ranging from $\dot{m}$ = 0.0064 to 0.025 kg/s in intervals of approximately 0.002 kg/s. A 3-D paraboloid regression equation was generated using SigmaPlot to relate temperature, flow meter voltage, and mass flow rate, and was given by

$$\dot{m}_{\mathrm{cp}} = y_0 + aT + bV + cT^2 + dV^2 \tag{2.1}$$

where $y_0$, $a$, $b$, $c$, and $d$ are calibration constants (Appendix C). The general root-sum-square uncertainty equation used for all uncertainties was given by

$$\Delta y = \left[\left(\left(\frac{\partial y}{\partial x_1}\right)\Delta x_1\right)^2 + \left(\left(\frac{\partial y}{\partial x_2}\right)\Delta x_2\right)^2 + \cdots\right]^{1/2} \tag{2.2}$$

where $y = f(x_1, x_2, \ldots)$. The uncertainty of the mass flow rate measurement was affected by the maximum deviation of the regression equation from the actual data, the confidence interval for the temperature and flow meter voltage measurements, the root-sum-square total error associated with the scale and stopwatch given by

$$\Delta\dot{m}_{\mathrm{m/t}} = \left[\left(\left(\frac{1}{t}\right)\Delta m\right)^2 + \left(\left(-\frac{m}{t^2}\right)\Delta t\right)^2\right]^{1/2} \tag{2.3}$$

and the root-sum-square error associated with the temperature and voltage measurements given by

$$\Delta\dot{m}_{\mathrm{V/T}} = \left[\left((a + 2cT)\Delta T\right)^2 + \left((b + 2dV)\Delta V\right)^2\right]^{1/2} \tag{2.4}$$

The percent error on the mass flow rate decreased with increasing flow rate. Since the mass flow rate was kept constant at $\dot{m}_{cp}$ = 0.0077 kg/s, the uncertainty associated with that setting was 4.0%.

The heat transferred from the LHP condenser to the cold plate, $Q_{out}$, was defined as

$$Q_{out} = \dot{m}_{cp} C_{p,PAO} (T_{out} - T_{in}) \tag{2.5}$$

A linear fit equation for $C_{p,PAO}$ as a function of temperature was developed by Ghajar et al. (1994) and used in equation (2.5) (Appendix E). The average evaporative heat transfer coefficient was defined as

$$\bar{h} \equiv \frac{Q_{out}}{\pi D L (\bar{T}_e - T_v)} \tag{2.6}$$

where $D$ is the inside diameter of the evaporator shell, $L$ is the length of the evaporator, $\bar{T}_e$ is the average evaporator temperature measured by the four thermocouples embedded in the wall between the heater and the wick (Figure 2.5(b)), and $T_v$ is the external temperature of the vapor line at the outlet of the evaporator. The heat rejected to the cold plate, $Q_{out}$, was selected as it was the best estimate of heat actually transported by the LHP. The thermal resistance of the loop heat pipe, $R$, was determined using the average evaporator temperature and the average temperature of the cold plate, and was defined as

$$R \equiv \frac{\bar{T}_e - \bar{T}_{cp}}{Q_{out}} \tag{2.7}$$

where $\bar{T}_{cp}$ is the average cold plate temperature. The root-sum-square uncertainty of $Q_{out}$, $\bar{h}$, and $R$ are given by

$$\begin{aligned} \Delta Q_{out} = \Big[ &\left(C_{p,PAO}(T_{out} - T_{in})\Delta\dot{m}_{cp}\right)^2 + \left(\dot{m}_{cp}(T_{out} - T_{in})\Delta C_{p,PAO}\right)^2 \\ &+ \left(\dot{m}_{cp} C_{p,PAO} \Delta T_{out}\right)^2 + \left(-\dot{m}_{cp} C_{p,PAO} \Delta T_{in}\right)^2 \Big]^{1/2} \end{aligned} \tag{2.8}$$

$$\Delta\bar{h} = \left[\left(\frac{1}{\pi DL(\bar{T}_{\mathrm{e}} - T_{\mathrm{v}})}\Delta Q_{\mathrm{out}}\right)^2 + \left(\frac{Q_{out}}{\pi D^2 L(\bar{T}_{\mathrm{e}} - T_{\mathrm{v}})}\Delta D\right)^2 + \left(\frac{Q_{\mathrm{out}}}{\pi DL^2(\bar{T}_{\mathrm{e}} - T_{\mathrm{v}})}\Delta L\right)^2 + \left(\frac{Q_{\mathrm{out}}}{\pi DL(\bar{T}_{\mathrm{e}} - T_{\mathrm{v}})^2}\Delta\bar{T}_{\mathrm{e}}\right)^2 + \left(\frac{Q_{\mathrm{out}}}{\pi DL(\bar{T}_{\mathrm{e}} - T_{\mathrm{v}})^2}\Delta T_{\mathrm{v}}\right)^2\right]^{1/2} \tag{2.9}$$

$$\Delta R = \left[\left(\frac{(\bar{T}_{\mathrm{e}} - \bar{T}_{\mathrm{cp}})}{Q_{\mathrm{out}}^2}\Delta Q_{\mathrm{out}}\right)^2 + \left(\frac{1}{Q_{\mathrm{out}}}\Delta\bar{T}_{\mathrm{e}}\right)^2 + \left(\frac{1}{Q_{\mathrm{out}}}\Delta\bar{T}_{\mathrm{cp}}\right)^2\right]^{1/2} \tag{2.10}$$

The uncertainty of $C_{\mathrm{p,PAO}}$ was estimated by Ghajar et al. to be 0.5% of the value. For each steady state condition, 151 data points were collected from each sensing device representing five minutes of data. Measured values were averaged and uncertainties were calculated based on the fixed error of each instrument and the confidence interval for the average at a confidence level of 0.95. A summary of the uncertainties for this experiment can be found in Table 2.4. Details of the uncertainty analysis can be found in Appendix B.

## 2.4. Results and Discussion

The purpose of this series of experiments was to determine the operating characteristics of a titanium-water loop heat pipe subjected to changes in evaporator heat input, compensation chamber heat input, and radial acceleration. Steady state and transient temperature data were collected which provided insight into the fluid-thermal behavior of the LHP. The raw data was reduced to obtain the evaporative heat transfer coefficient, thermal resistance, and evaporator wall superheat in terms of the heat transported and radial acceleration level. Quasi-steady phenomena and dry-out of the LHP were observed and quantified in a performance map.

Figure 2.8 presents a typical stationary ($a_z$ = 1.0 g, $a_r$ = 0.0 g) cold-start test of the LHP, which consisted of the following: With the LHP at ambient conditions, the recirculating chiller in the low-temperature fluid loop was set to $T_{\mathrm{eg}}$ = 35°C. Heat was applied as a step function to the evaporator section (in this case, $Q_{\mathrm{in}}$ = 600 W) while the pump for the high-temperature fluid loop was simultaneously turned on ($\dot{m}_{\mathrm{cp}}$ = 0.0077

kg/s). The mass flow rate of the high-temperature fluid loop was maintained constant at this value throughout this series of experiments to minimize the uncertainty associated with the calorimetry of the cold plate. Figure 2.8(a) shows the transient temperature response of the evaporator, vapor line, and calorimeter inlet and outlet. The temperatures appear to become steady after approximately 6000 s. However, in order to determine when steady state occurred the time rate of change of the temperatures was averaged over 15 min. intervals and plotted with respect to time as shown in Figure 2.8(b). It was observed that d$T$/d$t$ approached zero shortly after 6000 s, but for times greater than 6000 s, significant oscillations occurred. The oscillations in d$T$/d$t$ were not apparent in the raw temperature traces, but steady state was found to occur at approximately 18,000 s. This was further demonstrated by calculating the thermal resistance and heat transfer coefficient for this test at different times, as shown in Figure 2.8(c). This methodology was used throughout testing to ensure that a repeatable steady state was reached.

Figure 2.9 also shows transient temperature traces during the $Q_{in}$ = 600 W test described in the previous paragraph. In Figure 2.9(a), the evaporator temperature (TC04) increased very quickly while the rest of the LHP did not react. After approximately 60 s, the thermocouple located on the vapor line nearest to the exit of the evaporator (TC08) suddenly increased. This was followed in turn by increases in temperature reflected by the thermocouples located throughout the condenser section. This shows the progression of the saturated vapor clearing the condenser section of liquid, which was subsequently displaced into the evaporator section and the compensation chamber via the bayonet tube. Figure 2.9(b) shows that the evaporator temperature was significantly higher than the condenser temperatures, which led to a relatively high value of thermal resistance, which will be discussed in detail below.

Figure 2.10 shows temperature traces in the condenser (TC09 through TC13) and at the bayonet inlet (TC14). Each figure shows the transient temperature after the stationary LHP reached steady state conditions at heat inputs ranging from $100 \leq Q_{in} \leq 600$ W. In Figure 2.10(a), with $Q_{in}$ = 100 W, the liquid entering the bayonet tube was highly subcooled at approximately 40°C. At this heat input level, the majority of the condenser was flooded with subcooled liquid. In fact, only TC09 (condenser inlet) indicated two-phase flow. Figure 2.10(b), with $Q_{in}$ = 200 W, was a unique case that is

described further in the following paragraph (Figure 2.11). Figure 2.10(c) to Figure 2.10(f) shows that the 2φ-1φ point progressed through the liquid line as heat input increased until it reached the bayonet inlet. If the heat input at the evaporator is high enough, saturated vapor will pass through the bayonet tube and reach the evaporator section. This point represents a performance limit to the LHP operation because if vapor enters the evaporator, the wick will dry out and the LHP will overheat.

Figure 2.11 shows the oscillatory behavior of the LHP for the heat input of $Q_{in}$ = 200 W. Initially, at $t$ = 0, the evaporator temperatures (TC04, TC05, TC06, and TC07) ranged from 66 to 68°C. The evaporator temperature nearest to the bayonet tube outlet (TC07) was the lowest, which indicated that the subcooled liquid that entered the evaporator tended to reduce the evaporator temperature at this point. The vapor line and condenser temperatures (TC08 through TC13) ranged from 46 to 58°C. The vapor line (TC08) was the highest, with the first three thermocouples in the condenser (TC09, TC10, TC11) decreasing slightly. The vapor became saturated within the condenser, and condensation formed on the interior walls of the tubing. From the point at which the quality of the working fluid was $x$ = 1 (saturated vapor) to where it reached $x$ = 0 (saturated liquid), the temperature should have been constant, except for the fact that the pressure dropped slightly due to viscous losses. This drop in the saturation pressure in turn decreased the saturation temperature. Past TC11, the other condenser temperatures (TC12, TC13) dropped significantly. This showed that the 2φ-1φ point, where $x$ = 0, occurred between TC11 and TC12. The working fluid after this point became a subcooled liquid, where the temperature drop was due to sensible heat extraction by the cold plates. Interestingly, at $t$ = 0, the temperature at the bayonet inlet (TC14) was higher than the outlet of the condenser. Under typical operation, this was not the case due to convective losses from the liquid lines.

As time progressed from $t$ = 0 (Figure 2.11(a)), several things occurred nearly simultaneously. The evaporator thermocouple nearest to the vapor manifold (TC07) suddenly decreased, which indicated movement of subcooled liquid from the exit of the bayonet tube into the evaporator. The junction between the evaporator and the compensation chamber (TC15) increased and then decreased in temperature over a relatively short period. This was due to warm liquid in the evaporator section being

pushed through the grooves into the compensation chamber, followed by cooler liquid from the bayonet tube exit. The inlet of the bayonet tube (TC14) decreased, and the two thermocouples measuring the subcooled liquid in the condenser increased (TC12 and TC13). Again, this was indicative of movement of the slug of liquid that existed from the 2φ-1φ point in the condenser to the meniscus within the grooves of the secondary wick inside the evaporator section, as shown in Figure 2.2(a). The dramatic increase in the condenser section (TC12) shows that the 2φ-1φ point moved from between TC11 and TC12, across the TC12 location, and then between TC12 and TC13 as shown schematically in Figure 2.11(b). In fact, TC12 increased to the saturated vapor temperature existing within the first half of the condenser.

At approximately $t$ = 80 s, the temperatures in the evaporator and the bayonet tube inlet (TC14) started to increase, while the condenser temperatures TC12 and TC13 decreased. This behavior indicated that the liquid slug had reversed direction; i.e. the 2φ-1φ point re-crossed thermocouple location TC12 in the condenser. The significant rise in the bayonet inlet temperature TC14 shows that warm liquid originally in the evaporator was now flooding back through the bayonet tube into the liquid line. This movement of liquid out of the evaporator may be due to the sudden appearance of a vapor bubble within the wick structure of the evaporator section which would tend to drive the heated liquid in the evaporator in the opposite direction. As can be seen in Figure 2.11(a), the period of the oscillation was approximately 150 s. This type of percolation is not typical of a fully operational LHP, but is actually closer to the behavior of a pulsating heat pipe. Discussion of flow reversal within LHPs in the literature was limited to startup and shutdown operation. Douglas et al. (1999) discussed flow reversal in LHPs as a phenomenon that occurred during startup and continued until the capillary pressure in the secondary wick could no longer maintain the system pressure drop. Cimbala et al. (2004) used neutron radiography to visualize LHP operation and observed flow reversal only occurred when the heat input was reduced to $Q_{in}$ = 0 W. It was concluded that with no heat input, convective and radiative heat transfer from the LHP to the ambient caused the flow reversal. In general, flow reversal was not discussed as part of normal operation. However, in the present experiment, flow reversal was found at some operating points.

Figure 2.12 shows the various steady state LHP temperatures versus transported heat for the stationary case. The four evaporator temperatures in Figure 2.12(a) increased monotonically with heat transported, but diverged from the vapor outlet temperature. The behavior of the condenser temperatures with heat transported was slightly different, as shown in Figure 2.12(b). At the lowest heat input value ($Q_{in}$ = 100 W), a significant temperature drop was present between the inlet of the condenser (TC09) and the thermocouples within the condenser. This shows that the 2φ-1φ point resided between TC09 and TC10, which means that very little of the available condenser was being used for two-phase condensation. This condition also shows that the liquid returning to the evaporator section (TC14) was highly subcooled. As the heat input increased to $Q_{in}$ = 200 W, the temperatures measured at TC10 and TC11 rose to match that at TC09, which means that the time averaged location of the 2φ-1φ point moved farther into the condenser (between TC11 and TC12). At a heat input of $Q_{in}$ = 300 W, the 2φ-1φ point traveled past the end of the condenser into the liquid lines such that all of the condenser temperatures matched the evaporator outlet temperature (TC08). As the heat input increased, the condenser temperatures continued to rise. However, the evaporator outlet temperature increased at a faster rate, which is indicative of an increased superheat penalty.

Figure 2.13 shows the thermal performance of the stationary LHP for heat inputs ranging from $Q_{in}$ = 100 to 600 W. The evaporative heat transfer coefficient, Figure 2.13(a), decreased monotonically with transported heat. This behavior was controlled by the slope of the average evaporator temperature versus that of the evaporator outlet, as shown in Figure 2.12(a). The temperature difference $\left(\overline{T}_e - T_v\right)$ defined in equation (2.6) increased more rapidly than $Q_{out}$, which resulted in an overall decrease in $\overline{h}$. As dry-out was approached, more of the wick in the evaporator section was depleted of liquid, which tended to increase the evaporator temperature. The thermal resistance of the stationary LHP versus heat transported is presented in Figure 2.13(b), where it is seen to decrease, reach a minimum, and then increase. At low power inputs, the relatively large temperature drop defined by equation (2.7), $\left(\overline{T}_e - \overline{T}_{cp}\right)$, drives the thermal resistance to a high value. This temperature drop was a result of the fact that most of the condenser

section was flooded by subcooled liquid which was close to the cold plate temperature. As the 2φ-1φ point moved through and then exited the condenser, the temperature drop decreased with transported heat, which decreased the thermal resistance. The minimum $R$ corresponds to the point in Figure 2.12(b) where the 2φ-1φ point just exited the condenser. Past this point, the evaporator section increased in temperature more rapidly than the condenser section, which resulted in the thermal resistance increasing with transported heat. The wall superheat, defined as the difference between the average evaporator temperature and the temperature of the evaporator/compensation chamber junction, was found to monotonically increase with an increasing amount of transported heat. With respect to the evaporative heat transfer coefficient, thermal resistance, and wall superheat, no notable difference was observed between starting the LHP while the unit was at ambient temperature versus a step change in the evaporator heat input from a lower to higher value or a higher to lower value. A summary of the stationary steady state data points and the path to reach steady state can be seen in Table 2.5.

Figure 2.14 shows the operating characteristics and performance of the stationary LHP for an evaporator heat input of $Q_{in}$ = 500 W while varying the compensation chamber heat input from $Q_{cc}$ = 0 to 50 W. For this particular test, the LHP was allowed to achieve steady state conditions for the given evaporator heat input, after which the compensation chamber heat input was incremented in steps of 5 W. In Figure 2.14(a) and Figure 2.14(b), for $Q_{cc}$ = 0 W, the evaporator temperatures were relatively uniform, where the vapor exiting the evaporator was slightly superheated and the 2φ-1φ point was out of the condenser. When a small amount of heat was input to the system through the compensation chamber ($Q_{cc}$ = 5 W), the evaporator temperatures and the evaporator exit temperature both decreased while the condenser temperatures remained constant. This trend continued until approximately $Q_{cc}$ = 15 W, at which point the evaporator temperature leveled off, the evaporator exit temperature decreased to the saturation temperature within the condenser, and the condenser outlet temperature dropped below the saturation temperature. The decrease in the average evaporator temperature significantly affected the evaporative heat transfer coefficient and the thermal resistance, as shown in Figure 2.14(c). In fact, $\bar{h}$ increased by 68% with an increase in the overall heat input of only 3%. The drop in the condenser outlet temperature indicated that the

2φ-1φ point moved from the liquid line into the condenser section. For $Q_{cc} \geq 20$ W, the evaporator temperatures increased and the 2φ-1φ point continued to move toward the evaporator which resulted in an increase in the thermal resistance. Ku (1999) indicated that operating the compensation chamber at a higher temperature by using an external heater in effect increases the amount of subcooling in the condenser and liquid return line. According to Ku (1999), this subcooling is necessary to balance the additional heat input and results in underutilizing the condenser and a degradation of the thermal conductance. In the present experiment, this conclusion held true for $Q_{cc} \geq 20$ W, as the amount of subcooling increased the thermal resistance and decreased the evaporative heat transfer coefficient by way of an increased superheat penalty. This did not hold true for $Q_{cc} < 20$ W. When the LHP operated at $Q_{in} = 500$ W, the 2φ-1φ interface was located in the liquid return line. Increasing the heat input to the compensation chamber moved the 2φ-1φ interface to the condenser outlet at $Q_{cc} = 15$ W. Operation at this point maximized the amount of heat transfer due to condensation with the added benefit of cooler liquid in the compensation chamber and evaporator which decreased the thermal resistance and increased the evaporative heat transfer coefficient.

Also of interest is the temperature increase at the bayonet inlet (TC14) starting when $Q_{cc} = 35$ W seen in Figure 2.14(b). Figure 2.15 shows the transient temperature traces of the condenser, bayonet tube, and evaporator/compensation chamber junction for $Q_{cc} = 25$ to 50 W. In Figure 2.15(a) and Figure 2.15(b), with $Q_{cc} = 25$ and 30 W, subcooled liquid moved through the bayonet inlet as seen in typical operation. In Figure 2.15(c) through Figure 2.15(f), with $Q_{cc} = 35$ through 50 W, a sudden increase in temperature at the bayonet inlet (TC14) showed that flow reversal occurred in the evaporator section. This was similar to the oscillating phenomena described for $Q_{in} = 200$ W except that the liquid-vapor meniscus in the secondary wick was driven backward by the elevated vapor pressure within the compensation chamber, which was due to the heat input at the shell of the compensation chamber. In addition, the temperature of the evaporator/compensation chamber interface (TC15) did not vary appreciably, which was different than that seen at $Q_{in} = 200$ W. The liquid-vapor meniscus moved backward due to the increased pressure within the compensation chamber until a point at which the pressure was balanced. Forward flow then resumed and heat was lost through the liquid

line, shown by the slow decrease in temperature at the bayonet inlet (TC14) to the temperature of the subcooled liquid at the condenser outlet (TC13). A summary of the steady state data points for $Q_{cc}$ = 0 to 50 W can be seen in Table 2.6.

To further explore compensation chamber heat input and heat loss to the ambient, Table 2.7 shows the effect of operating the stationary LHP for $Q_{in}$ = 500 W with the compensation chamber uninsulated, insulated, temperature controlled to $T_{cc}$ = 72.8°C via simultaneous heat input to the compensation chamber ($Q_{cc}$ = 20 W) and evaporator, and preconditioning the temperature to $T_{cc}$ = 72.8°C via heat input ($Q_{cc}$ = 100 W reduced to $Q_{cc}$ = 20 W) prior to heat input to the evaporator. For this series of tests, thermocouple TC15 was relocated to the top side of the compensation chamber to directly monitor its operating temperature. It was observed that the average evaporator temperature increased, the evaporative heat transfer coefficient decreased, and the thermal resistance increased in the uninsulated state when compared to the insulated case. The uninsulated compensation chamber operated at a temperature 3.6°C lower than the insulated case as expected due to free convection and radiative heat loss. To estimate the amount of heat loss to the ambient in the uninsulated case, the exposed compensation chamber was modeled as a cylinder in free convection with radiation. The average Nusselt number for free convection was given by (Incropera and DeWitt, 2002)

$$\overline{\mathrm{Nu}}_{\mathrm{D}} = \left\{0.60 + \frac{0.387\mathrm{Ra}_{\mathrm{D}}^{1/6}}{[1 + (0.559/\mathrm{Pr})^{9/16}]^{8/27}}\right\}^2 \tag{2.11}$$

where

$$\mathrm{Ra}_{\mathrm{D}} = \frac{g\beta(T_{\mathrm{s}} - T_{\infty})D^3}{\nu\alpha} \tag{2.12}$$

with air properties evaluated at the average temperature of the freestream and the surface. The average heat transfer coefficient was given by

$$\bar{h} = \frac{k}{D}\overline{\mathrm{Nu}}_{\mathrm{D}} \tag{2.13}$$

The total heat loss per unit length from the compensation chamber was given by

$$q'_{\mathrm{tot}} = q'_{\mathrm{conv}} + q'_{\mathrm{rad}} = \bar{h}\pi D(T_{\mathrm{s}} - T_{\infty}) + \epsilon\pi D\sigma(T_{\mathrm{s}}^4 - T_{\mathrm{surr}}^4) \tag{2.14}$$

The emissivity of grade 2 titanium used in this calculation was $\varepsilon$ = 0.3 (Boyer et al., 1994). The heat loss from the compensation chamber for the uninsulated case was found to be $Q_{cc}$ = -6.2 W. When the uninsulated case was included with the previous compensation chamber heat input data, it was found that evaporative heat transfer coefficient and thermal resistance followed the trends shown in Figure 2.14(c). These results were expected since removing the insulation from the compensation chamber in effect provided cooling, which moved the 2φ-1φ point away from the condenser. The average evaporator and cold plate temperatures were significantly different which was likely due a 10°C higher ambient temperature during the test involving the variation of compensation chamber heat input from $Q_{cc}$ = 0 to 50 W. As a result, for this particular case, it was advantageous to operate the LHP compensation chamber insulated for improved performance. For controlling the temperature of the compensation chamber, the evaporative heat transfer coefficient, thermal resistance, and operating temperatures were nearly identical between simultaneous compensation chamber and evaporator heat input startup and compensation chamber temperature preconditioning, demonstrating that the startup procedure had no impact on steady state conditions. However, preconditioning the compensation chamber required approximately one hour less time to reach steady state conditions over the simultaneous heat input startup.

Figure 2.16 presents transient LHP temperatures for a typical test at elevated acceleration ($a_z$ = 1.0 g, $a_r$ > 0 g). With the LHP at ambient conditions, the recirculating chiller in the low temperature loop was set to $T_{eg}$ = 35°C. Heat was applied as a step function (in this case, $Q_{in}$ = 600 W) while simultaneously starting the pump for the high-temperature loop ($\dot{m}_{cp}$ = 0.0077 kg/s). In addition, the radial acceleration was increased to $a_r$ = 0.1 g, which was a nominally small value to prevent damage to the power slip rings (Figure 2.16(a)). The LHP was allowed to achieve steady state conditions at $a_r$ = 0.1 g, indicated by d$T$/d$t$ (Figure 2.16(c)) decreasing to below the threshold of 0.01 K/min, then the acceleration was increased to the next desired radial acceleration value (in this case, $a_r$ = 10.0 g). The LHP was again allowed to achieve steady state conditions at the given acceleration (Figure 2.16(b)), then the acceleration was reduced back to $a_r$ = 0.1 g for a minimum of thirty min. If another elevated acceleration was desired, steady state at $a_r$ = 0.1 g was reached before increasing the acceleration level. When the

acceleration was increased to $a_r$ = 10.0 g at $t$ = 15,000 s in Figure 2.16(b), the average evaporator temperature increased by 11°C. The 2φ-1φ point moved to the condenser outlet from the liquid line with increasing acceleration, indicated by the small oscillations in temperature at the TC13. The amount of subcooling increased overall as indicated by the decrease in temperature at the bayonet inlet (TC14). These phenomena may be due in part to fluid redistribution in the LHP and is discussed in the following paragraph.

As the rotational velocity of the centrifuge increased, the resultant acceleration vector magnitude and direction changed (Figure 2.17(a)) which influenced the distribution of fluid in the LHP. Subcooled liquid entering the primary wick of the evaporator was forced to the outboard side of the evaporator body, opposite of the heat source, and perhaps leading to a partial dry-out of the wick (Figure 2.17(b)). The elevated acceleration also hindered the ability of the secondary wick in the compensation chamber to supply the evaporator with liquid due to pooling. In the condenser, pooling occurred in the bends of the condenser coil, again due to the acceleration gradient. Depending on the acceleration vector direction, this pooling could either open or close the passage to vapor flow (Figure 2.17(c)). All of these phenomena are a result of centrifuge testing. Due to the short radius, strong acceleration gradients occur that could have advantageous or adverse effects on the LHP operation. Operation in an aircraft environment, with significantly larger radii during turns, will provide a more uniform acceleration gradient across the LHP and potentially yield different temperature profiles, evaporative heat transfer coefficients, and thermal resistances.

Figure 2.18 shows the thermal performance of the LHP for radial accelerations ranging from $a_r$ = 0.1 to 10.0 g and heat inputs ranging from $Q_{in}$ = 100 to 600 W. The evaporative heat transfer coefficient, Figure 2.18(a), again decreased with transported heat, similar to the trend in Figure 2.13(a) for the stationary LHP. The thermal resistance of the LHP (Figure 2.18(b)), was found to decrease to a minimum, then increase, again similar to the stationary test results shown in Figure 2.13(b). In fact, when combining the stationary and elevated acceleration test data, it was found that the evaporative heat transfer coefficient and thermal resistance data were in close agreement with each other, regardless of the radial acceleration. This indicated that bench top testing of the LHP was a reliable method for determining the evaporative heat transfer coefficient and thermal

resistance of a LHP in an elevated acceleration environment. However, it will be shown that this was not true with respect to finding the dry-out limit. The wall superheat (Figure 2.18(c)) was higher at elevated accelerations when compared to $a_r$ = 0 g. This was possibly due to fluid redistribution in the evaporator forcing liquid away from the heater. A summary of all elevated acceleration steady state data points can be seen in Table 2.8.

Ku et al. (2000a and 2000b) observed that radial acceleration changed the fluid distribution throughout the LHP which changed operating temperatures and that acceleration could either increase or decrease LHP operating temperatures. In addition, temperature overshoots were observed for mid-range heat inputs and the wall superheat, defined as the temperature difference between the evaporator and compensation chamber, was independent of heat input and acceleration during startup. In the present elevated acceleration tests, it was observed that the accelerating force changed the fluid distribution within the LHP, causing the operating temperatures to change. However, in all instances, it was observed that elevated acceleration forces increased operating temperatures over those at $a_r$ = 0.1 g. Significant temperature overshoots were not observed in any of the elevated acceleration tests.

Figure 2.19 shows the transient response of the LHP during a series of dry-out events. Dry-out was indicated by a steady increase in the evaporator temperature and a decrease in the heat extracted by the calorimeter $Q_{out}$. In addition, the position of the 2φ-1φ point in the condenser moved toward the evaporator as indicated by a sequential decrease in the condenser temperatures. This occurred because the evaporator no longer generated a sufficient flow of vapor which changed the operating point of the LHP. In Figure 2.19(a), the LHP reached steady state while rotating slowly at $a_r$ = 0.1 g and $Q_{in}$ = 400 W. The rotational speed of the centrifuge table was increased until the radial acceleration reached $a_r$ = 8.0 g at $t$ = 300 s. After the evaporator temperature TC06 reached $T_{e,max}$ = 150°C, the radial acceleration was reduced back to $a_r$ = 0.1 g. At this time, the evaporator temperature continued to increase, but then leveled off and then decreased back to nearly the same temperature as the previous steady state. In fact, all of the LHP temperatures returned to within 1°C of the original steady state except for TC13 (condenser outlet), which returned to within 4°C of the previous steady state. This larger temperature difference in TC13 was attributable to a slight change in the location of the

2φ-1φ point in the condenser. This recovery behavior shows that the LHP was capable of repriming at the end of an acceleration burst even if the heat input remained constant. In Figure 2.19(b) and Figure 2.19(c), the radial acceleration was again increased from $a_r$ = 0.1 to 8.0 g with the same heat input ($Q_{in}$ = 400 W). In fact, all of the experiments presented in Figure 2.19 were performed sequentially. In Figure 2.19(b), the evaporator temperature TC06 was allowed to reach $T_{e,max}$ = 175°C before decreasing the radial acceleration to $a_r$ = 0.1 g, and in Figure 2.19(c), the evaporator temperature TC06 reached $T_{e,max}$ = 200°C before decelerating. In each instance, the evaporator temperature continued to increase, reached a maximum, and then decreased to the original steady state. However, the intensity of dry-out did seem to have an impact on the ability of the LHP to reprime. In Figure 2.19(c), with a maximum evaporator temperature at deceleration of $T_{e,max}$ = 200°C, the evaporator temperature reached two maximums before finally decreasing back to the previous steady state, whereas in Figure 2.19(a) and Figure 2.19(b), the maximum evaporator temperatures reached a peak and then monotonically decreased. This indicated that if the evaporator temperature were much higher than 200°C, the LHP may not have recovered, which would have required that the heat input be reduced to zero.

Figure 2.20 shows the temperature traces associated with the test at $Q_{in}$ = 200 W and $a_r$ = 0.1 and $a_r$ = 4.0 g. Following the previously mentioned startup procedures, the LHP reached a quasi-steady state while the centrifuge table rotated slowly for $a_r$ = 0.1 g, as shown in Figure 2.20(a). Similar to the stationary case at this heat input, the LHP temperatures oscillated, showing that the heat pipe was operating during reversals in the liquid flow due to the liquid-vapor meniscus in the secondary wick moving back and forth. Overall, the temperatures shown in Figure 2.20(a) were quite close to the case shown in Figure 2.11(b), as presented in Table 2.9. In addition, the period of the oscillation of the $a_r$ = 0.1 g case was nearly identical to the $a_r$ = 0 g case (approximately 175 s). The only significant differences in the independent variables between the two tests were the ambient temperature ($\Delta T_{amb}$ = 5.3°C), and the relatively small value of the radial acceleration. Of note, however, was the location of the 2φ-1φ point in the condenser: For $a_r$ = 0 g, this point resided close to TC12, whereas for the case in which $a_r$ = 0.1 g, the 2φ-1φ point was near TC10. The linear distance between these two points

was approximately 143 cm. While it was impossible to know the exact location of the 2φ-1φ point due to the coarse resolution of the thermocouples in the condenser, it was obvious that the location had changed significantly between the two cases. In addition, the evaporative heat transfer coefficient decreased and the thermal resistance increased from $a_r$ = 0 to 0.1 g. It was believed that this small value of the radial acceleration resulted in a significant change in location of the 2φ-1φ point due to the pooling of liquid.

After achieving the quasi-steady state at $a_r$ = 0.1 g, the radial acceleration was increased to $a_r$ = 4.0 g, and the LHP again reached a quasi-steady state, as shown in Figure 2.20(b). The average evaporator temperature increased by more than 30°C, and the temperature in the bayonet inlet ranged from $37 \leq T_{\text{bayonet inlet}} \leq 70$°C, which was a much larger range than that for $a_r$ = 0.1 g. Oscillations were again seen at this acceleration level, but the period of the oscillations increased to approximately 350 s. This may be due to the distance that the meniscus travelled within the evaporator, which resulted in wider swings in the evaporator temperatures and significant oscillations of the cold plate outlet temperature, which was nearly steady in the $a_r$ = 0.1 g case.

Figure 2.21 shows the steady state performance map for the LHP relating radial acceleration and heat transported for $a_r$ = 2.0 to 10.0 g and $Q_{in}$ = 100 to 600 W. It was observed that dry-out conditions occurred at varying radial accelerations for $Q_{in}$ = 100 to 400 W. Dry-out conditions were not observed through $a_r$ = 10.0 g at $Q_{in}$ = 500 and 600 W. Quasi-steady state conditions were observed at $Q_{in}$ = 200 W and $a_r$ = 4.0 g. This demonstrated that bench-top testing cannot be used to determine the dry-out limit with respect to elevated acceleration.

## 2.5. Conclusions

The effect of changes in evaporator heat input, compensation chamber heat input, and radial acceleration on a titanium-water loop heat pipe were investigated for $Q_{in}$ = 100 to 600 W, $Q_{cc}$ = 0 to 50 W, and $a_r$ = 0.0 to 10.0 g. A transient temperature rate of change method was developed to ensure steady state had been achieved. For evaporator heat input $Q_{in}$ = 100 to 600 W, it was observed that the evaporative heat transfer coefficient decreased monotonically, thermal resistance decreased to a minimum, then increased over the same range, and wall superheat monotonically increased. Flow reversal was observed at $Q_{in}$ = 200 W due to vapor bubble generation in the evaporator.

When examining the effect of compensation chamber heat input for $Q_{in}$ = 500 W, it was found that the average evaporator temperatures dropped by 15°C and evaporative heat transfer coefficient improved by 68% with only a 3% increase in heat load. These results differ from Ku (1999) in that an improvement was observed for compensation chamber heat input up to the point where subcooling was occurring in the condenser. Flow reversal was observed starting at $Q_{cc}$ = 35 W due to the increased pressure in the compensation chamber driving the liquid/vapor meniscus backwards. Operating the LHP compensation chamber uninsulated at $Q_{in}$ = 500 W was found to degrade the LHP performance for this particular case and preconditioning the compensation chamber temperature prior to evaporator heat input shortened the time to steady state.

When examining the effect of radial acceleration, it was found that dry-out conditions occurred more readily at lower heat inputs ($Q_{in}$ = 100 to 400 W) than at higher heat inputs ($Q_{in}$ = 500 to 600 W). The LHP was found to be able to reprime after an acceleration event that caused dry-out without the heat input being reduced to zero. It was also observed that radial acceleration had little effect on the evaporative heat transfer coefficient and thermal resistance of the LHP. Wall superheat was found to be higher at steady state elevated accelerations when compared to $a_r$ = 0 g. This led to conclusion that bench top testing of the LHP is a reliable method for determining the evaporative heat transfer coefficient and thermal resistance of a LHP in an elevated acceleration environment induced by a centrifuge table, but is not sufficient for determining the wall superheat and dry-out limit. These results may or may not actually occur in an aircraft environment as centrifuge operation can induce artifacts in the data due to the short radius of operation.

## 2.6. Future Work

Experimentation in this thesis has been conducted using strict regimented procedures for repeatability and to allow comparisons across data sets. Typical operation of LHPs is not along regimented schedules but in transient environments where heat sources, heat sinks, and accelerating forces are varying with respect to time. As such, experimentation should be conducted using transient profiles to more closely mimic actual aircraft environments. Experimentation should also be conducted with tighter

control over the compensation chamber temperature to enhance repeatability and tailor operation to specific heat sources and sinks.

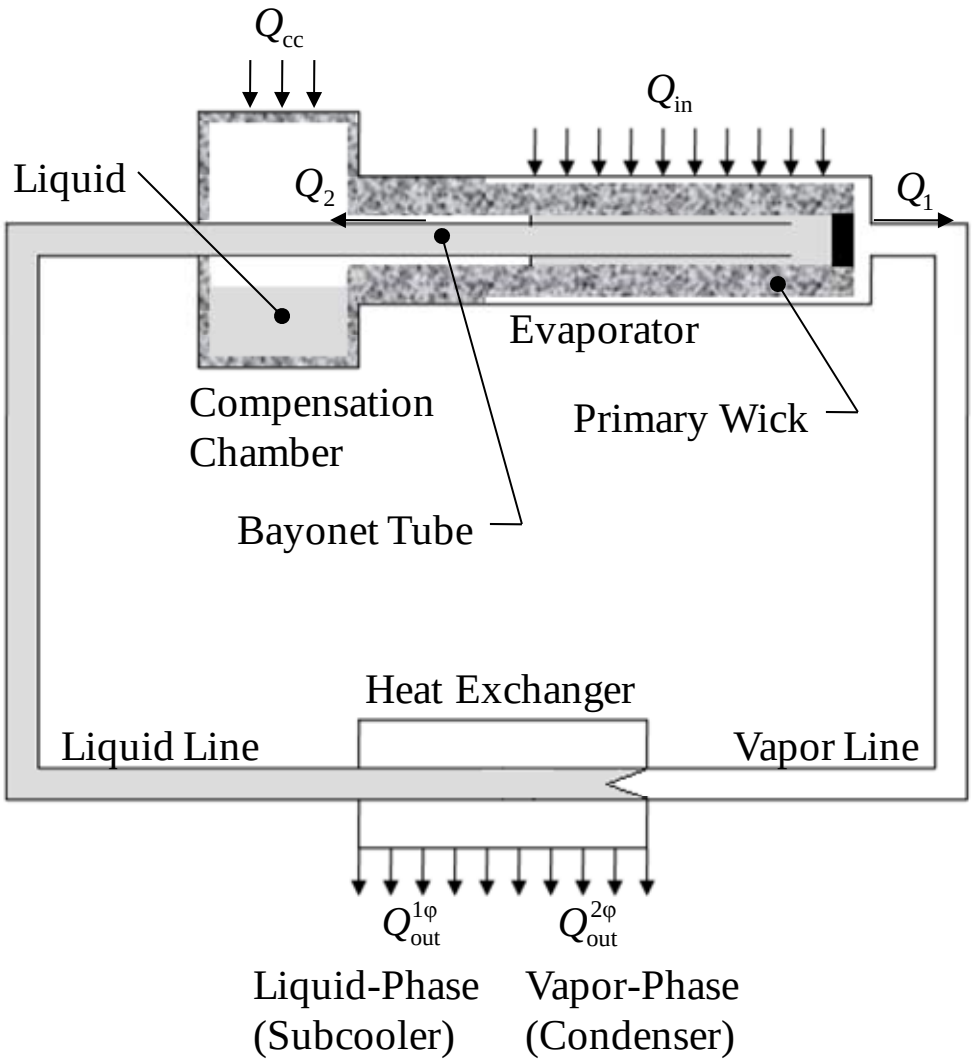


Figure 2.1. Loop heat pipe operation. Adapted and reprinted with permission from AIAA (Hoang and Ku, 2003).

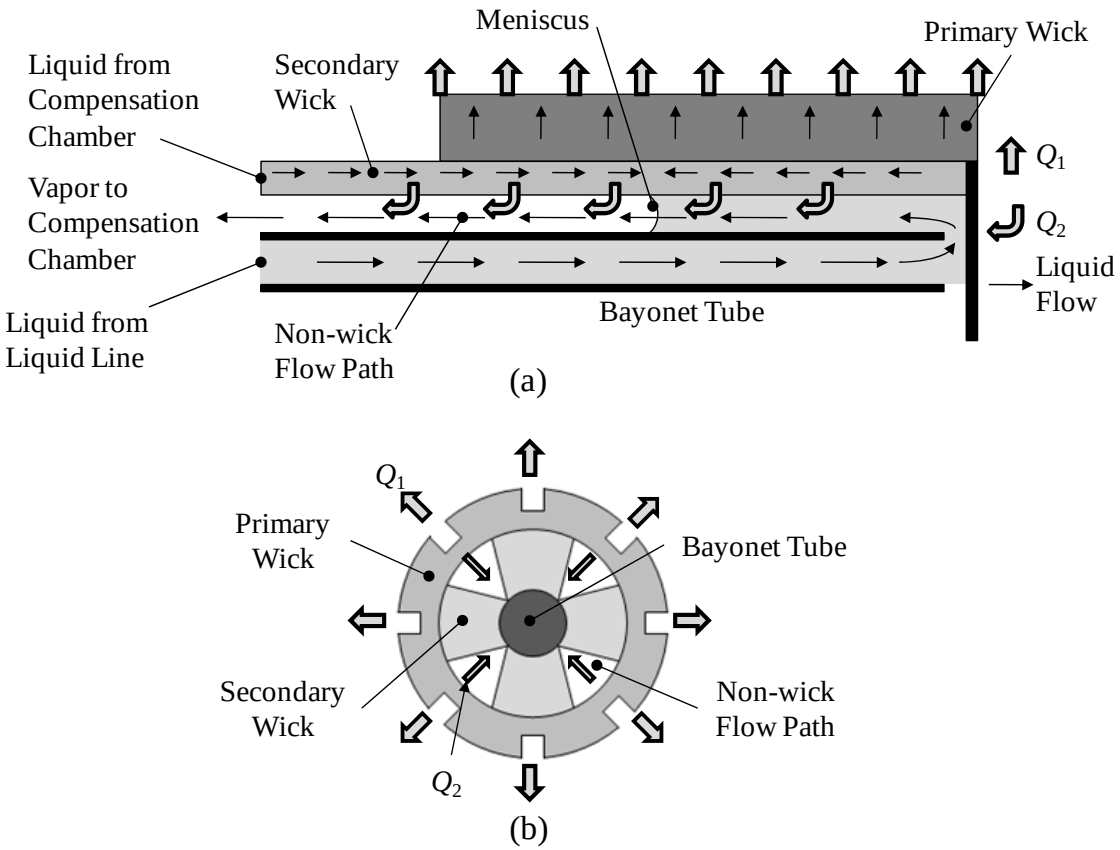


Figure 2.2. Evaporator schematic: (a) Side view; (b) Cross-sectional view. Adapted and reprinted with permission from AIAA (Hoang and Ku, 2003).

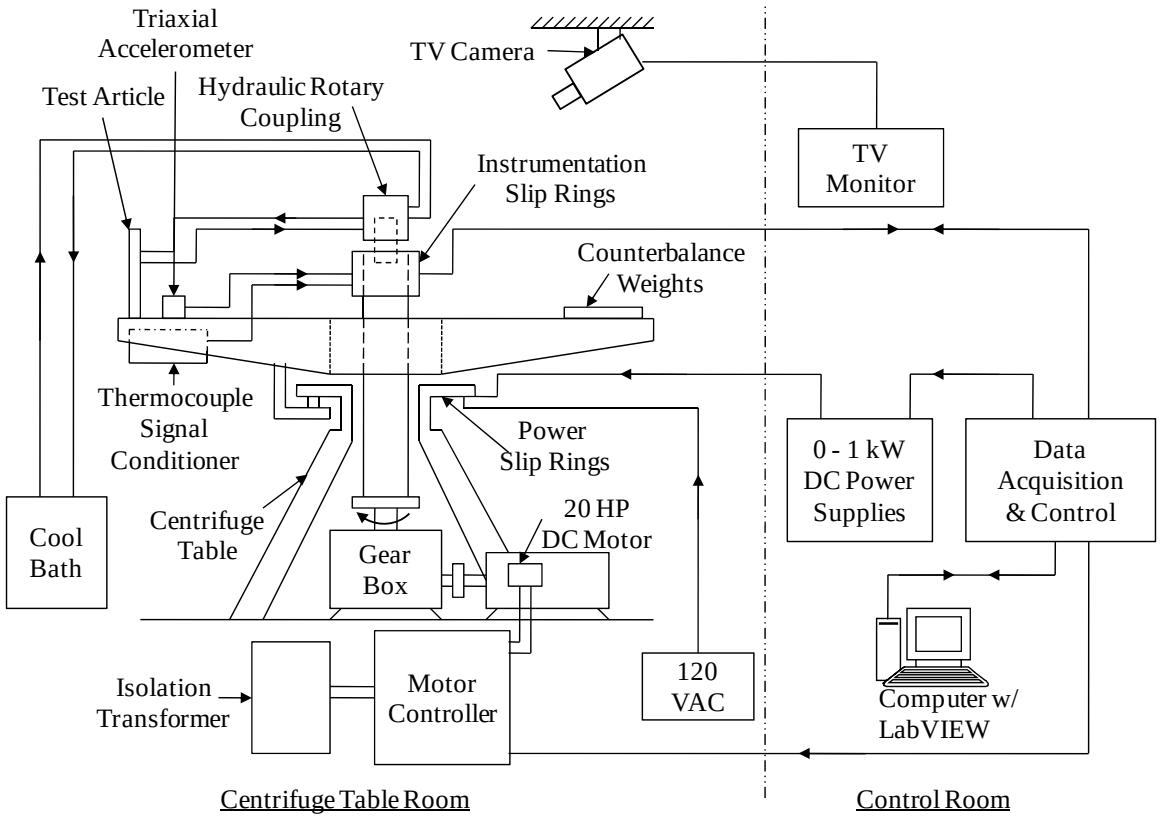


Figure 2.3. Schematic of Centrifuge Table Test Bed.

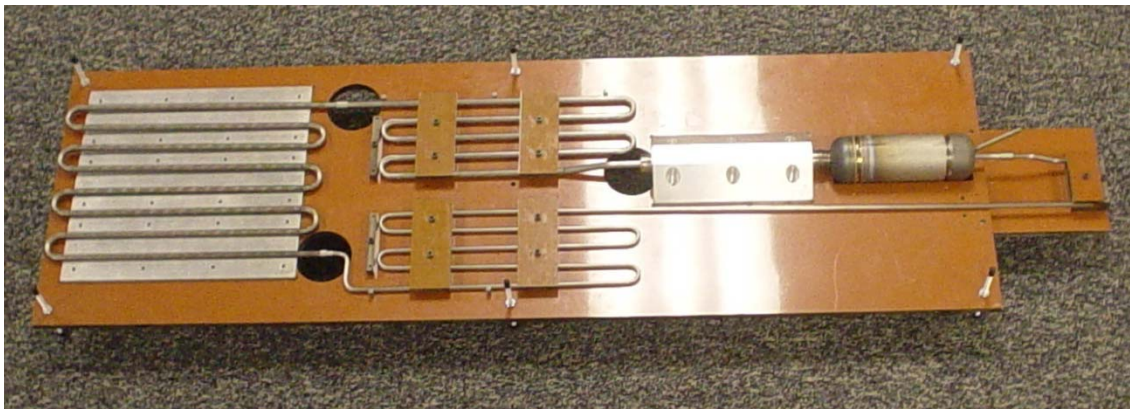

Figure 2.4. Titanium-water loop heat pipe test article as delivered.

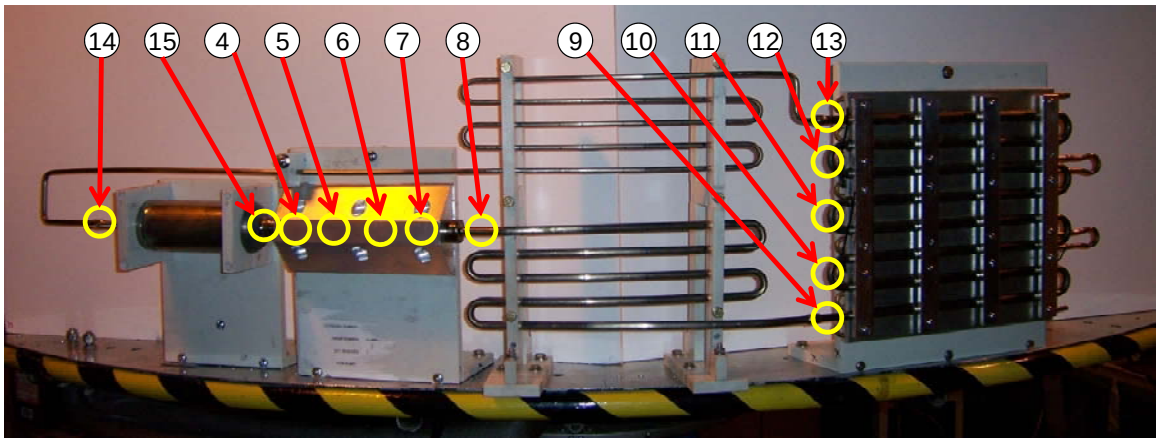


(a)

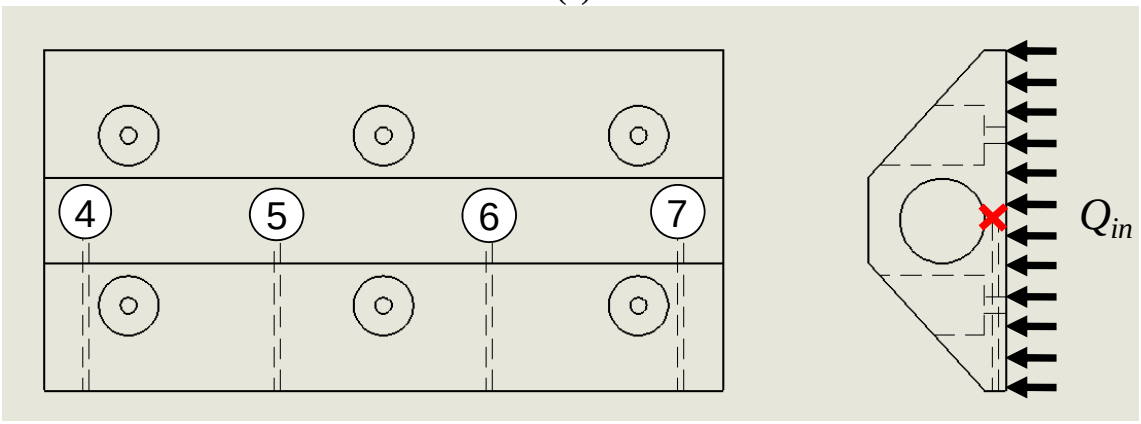


(b)

Figure 2.5. Thermocouple locations on the LHP: (a) Locations of thermocouples TC04 through TC15 across the LHP; (b) Locations of TC04 through TC07 within the evaporator.

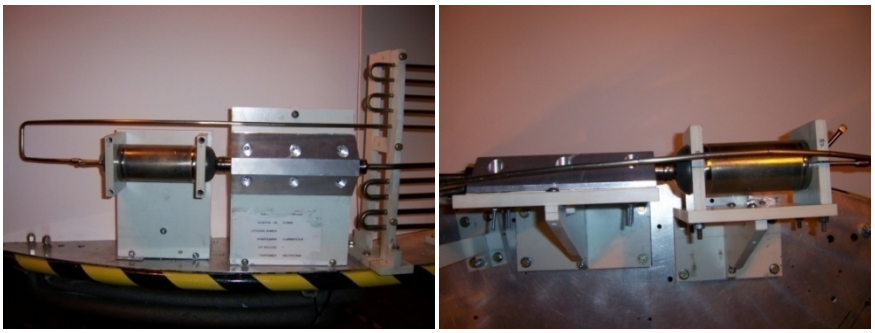

(a)

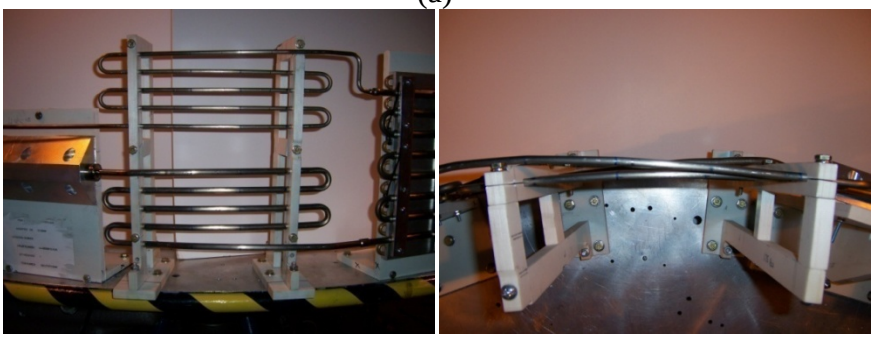

(b)

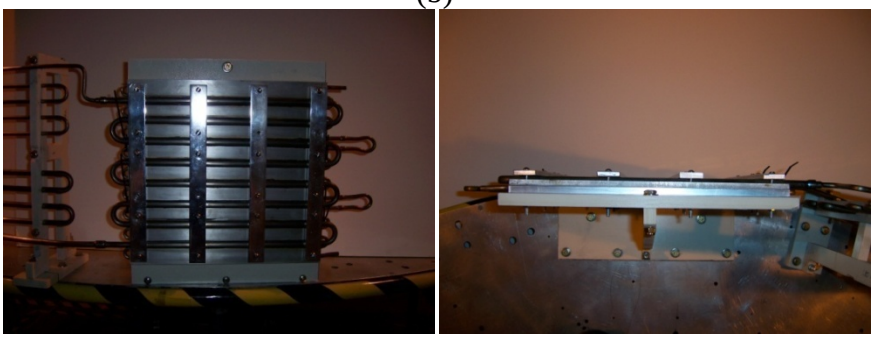

(c)

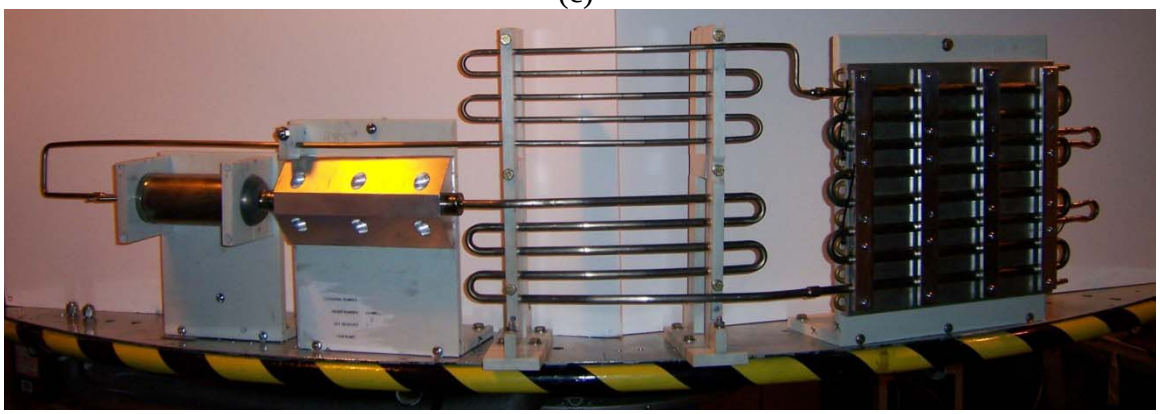

(d)

Figure 2.6. Mounting of loop heat pipe to centrifuge table, front and top views: (a) Evaporator and compensation chamber: (b) Transport lines; (c) Condenser with cold plate; (d) Complete loop heat pipe.

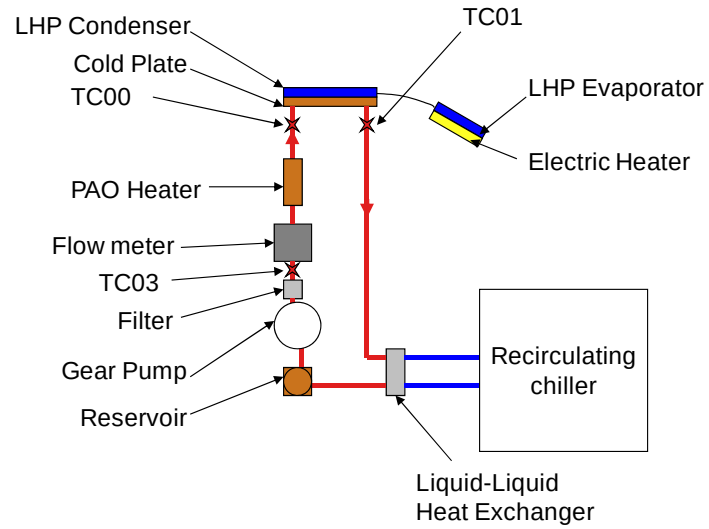


(a)

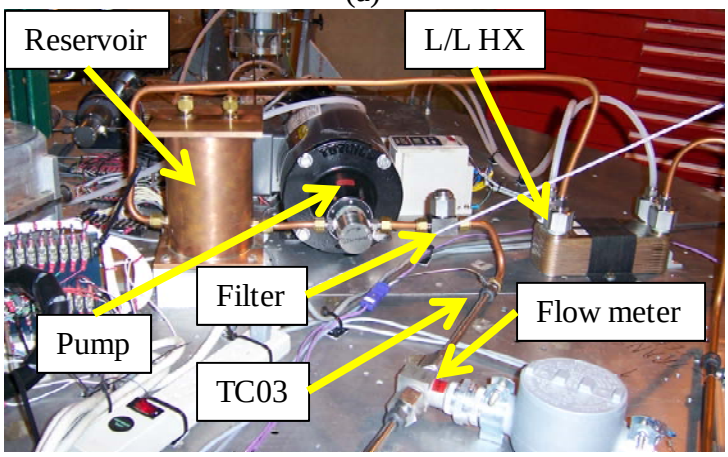


(b)

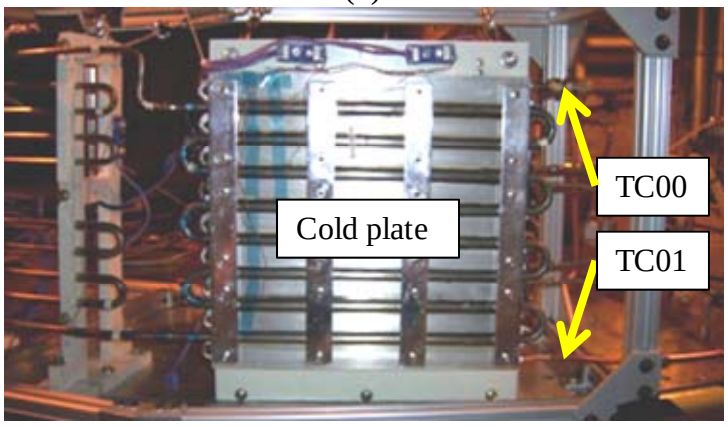


(c)

Figure 2.7. High temperature fluid loop: (a) Schematic; (b) Reservoir, pump, filter, flowmeter, TC03, and liquid/liquid heat exchanger; (c) Cold plate, TC00, and TC01.

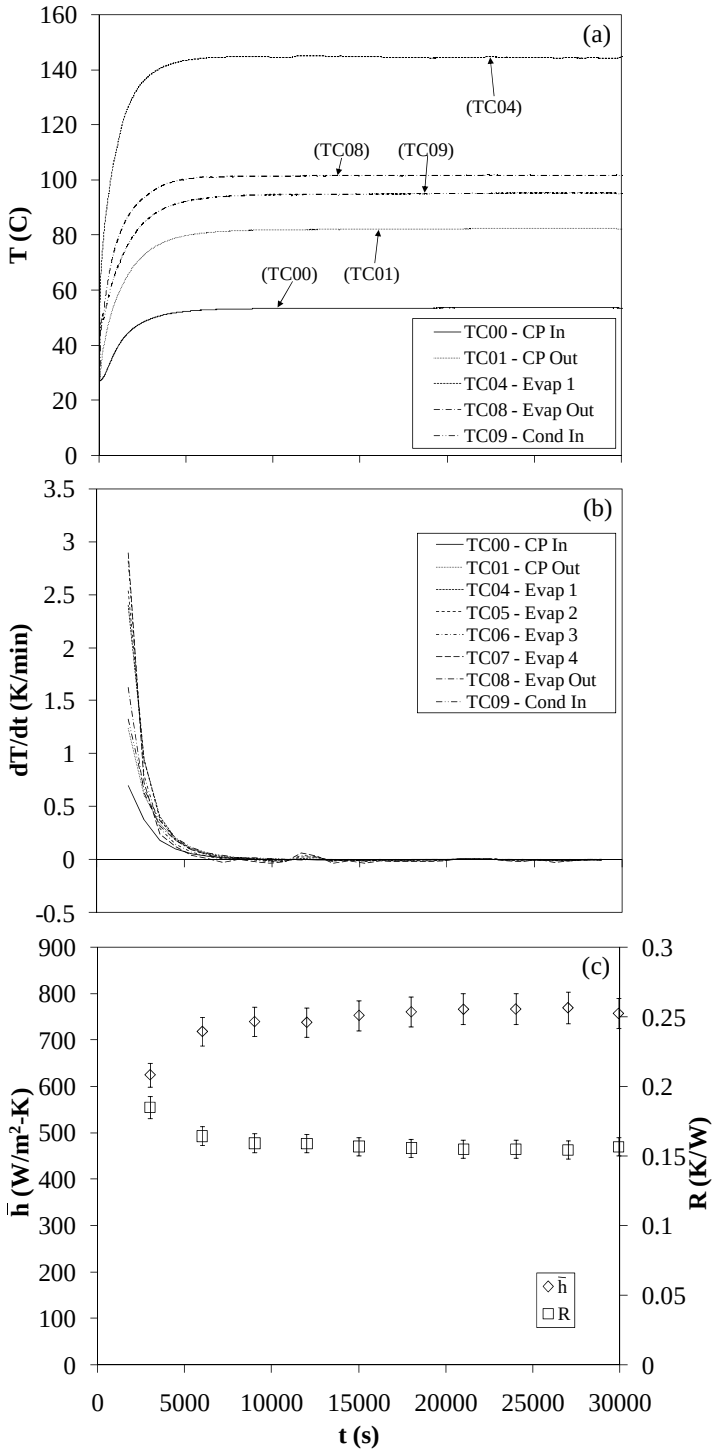


Figure 2.8. Use of a cold-start test to determine when steady state occurred for the stationary LHP ($Q_{in}$ = 600 W, $Q_{cc}$ = 0 W, $a_r$ = 0 g, $\dot{m}_{cp}$ = 0.0077 kg/s, $\overline{T}_{cp}$ = 67.7°C, $T_{amb}$ = 38.1°C): (a) Transient temperature traces; (b) Transient rate of change of temperatures; (c) Transient thermal resistance and evaporative heat transfer coefficient.

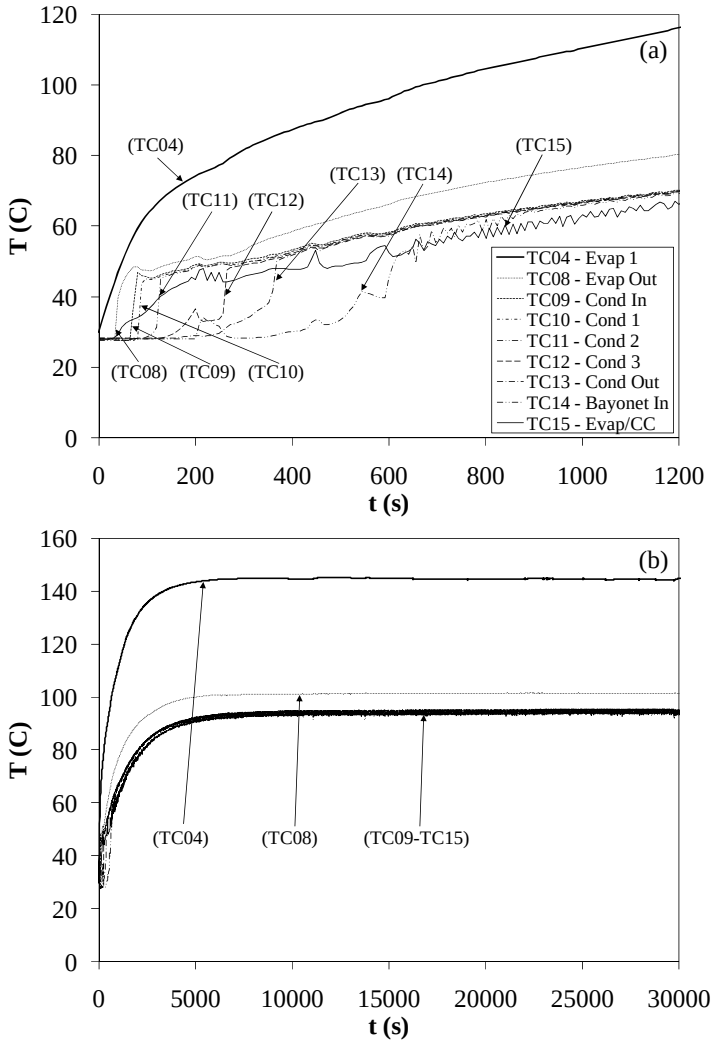


Figure 2.9. Transient startup of the stationary LHP ($Q_{in}$ = 600 W, $Q_{cc}$ = 0 W, $a_r$ = 0 g, $\dot{m}_{cp}$ = 0.0077 kg/s, $\overline{T}_{cp}$ = 67.7°C, $T_{amb}$ = 38.1°C): (a) Initial startup; (b) Complete startup until steady state.

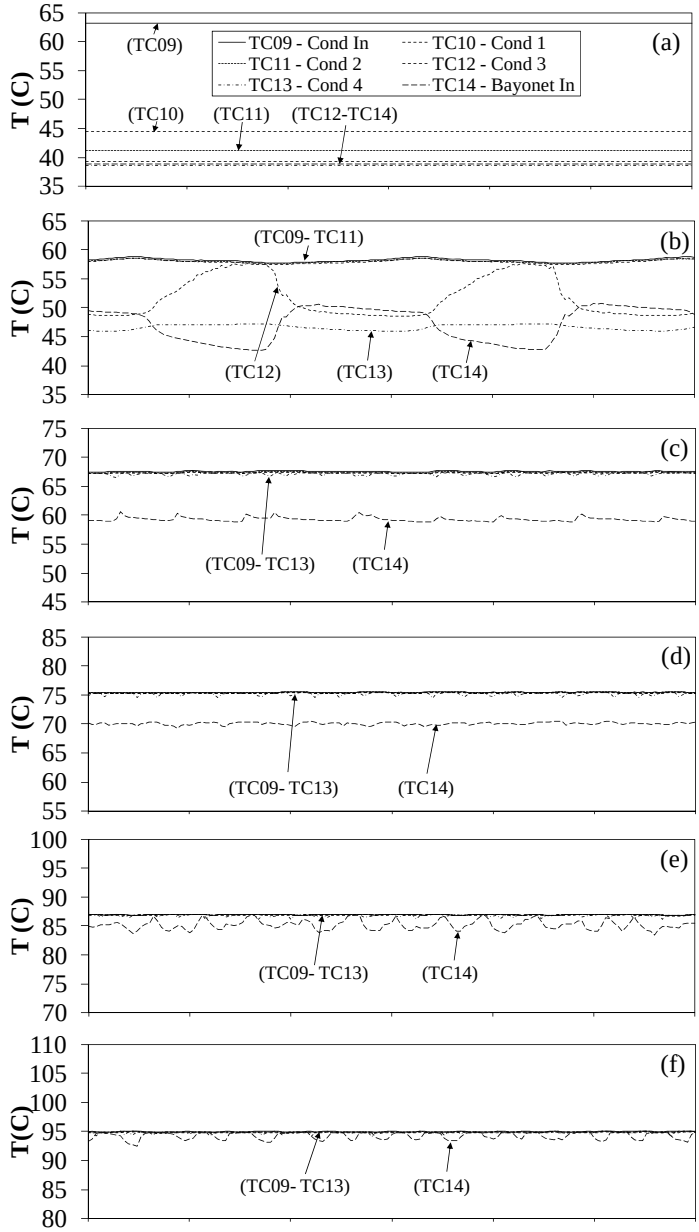


Figure 2.10. Transient temperature profiles in the condenser and bayonet tube of the stationary LHP ($Q_{cc}$ = 0 W, $a_r$ = 0 g, $\dot{m}_{cp}$ = 0.0077 kg/s, $36.8 \leq \overline{T}_{cp} \leq 71.6$°C, $31.7 \leq T_{amb} \leq 38.1$°C): (a) $Q_{in}$ = 100 W; (b) $Q_{in}$ = 200 W; (c) $Q_{in}$ = 300 W; (d) $Q_{in}$ = 400 W; (e) $Q_{in}$ = 500 W; (f) $Q_{in}$ = 600 W.

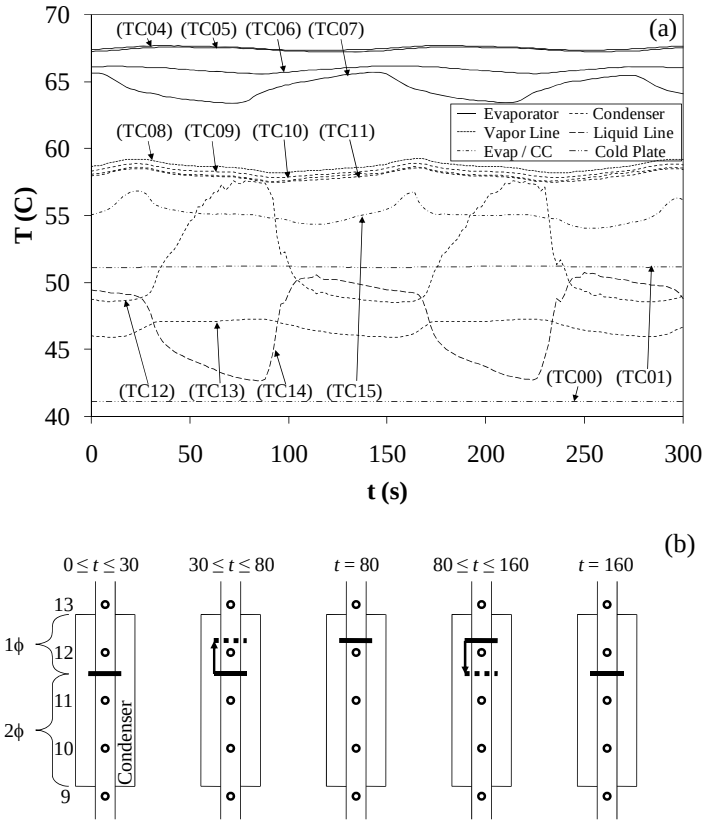


Figure 2.11. Transient temperature profiles of the stationary LHP for $Q_{in}$ = 200 W ($Q_{cc}$ = 0 W, $a_r$ = 0 g, $\dot{m}_{cp}$ = 0.0077 kg/s, $\overline{T}_{cp}$ = 46.1°C, $T_{amb}$ = 31.7°C): (a) Transient temperature profiles; (b) 2φ-1φ point oscillation in the condenser.

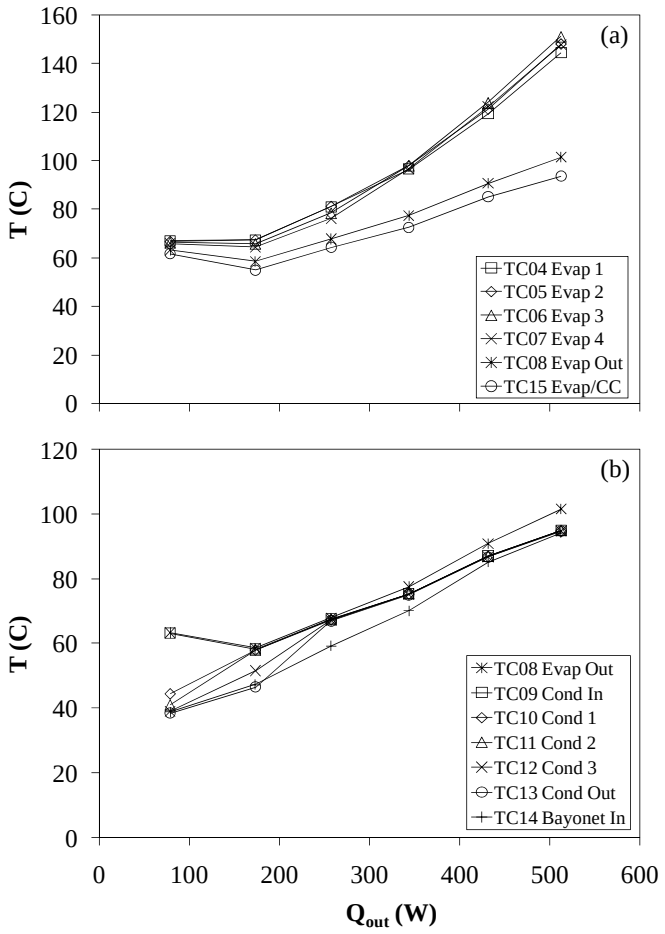


Figure 2.12. Steady state temperature distribution versus transported heat for the stationary LHP ($Q_{cc}$ = 0 W, $a_r$ = 0 g, $\dot{m}_{cp}$ = 0.0077 kg/s, 36.8 ≤ $\overline{T}_{cp}$ ≤ 71.6°C, 31.7 ≤ $T_{amb}$ ≤ 38.1°C): (a) Evaporator section; (b) Condenser section.

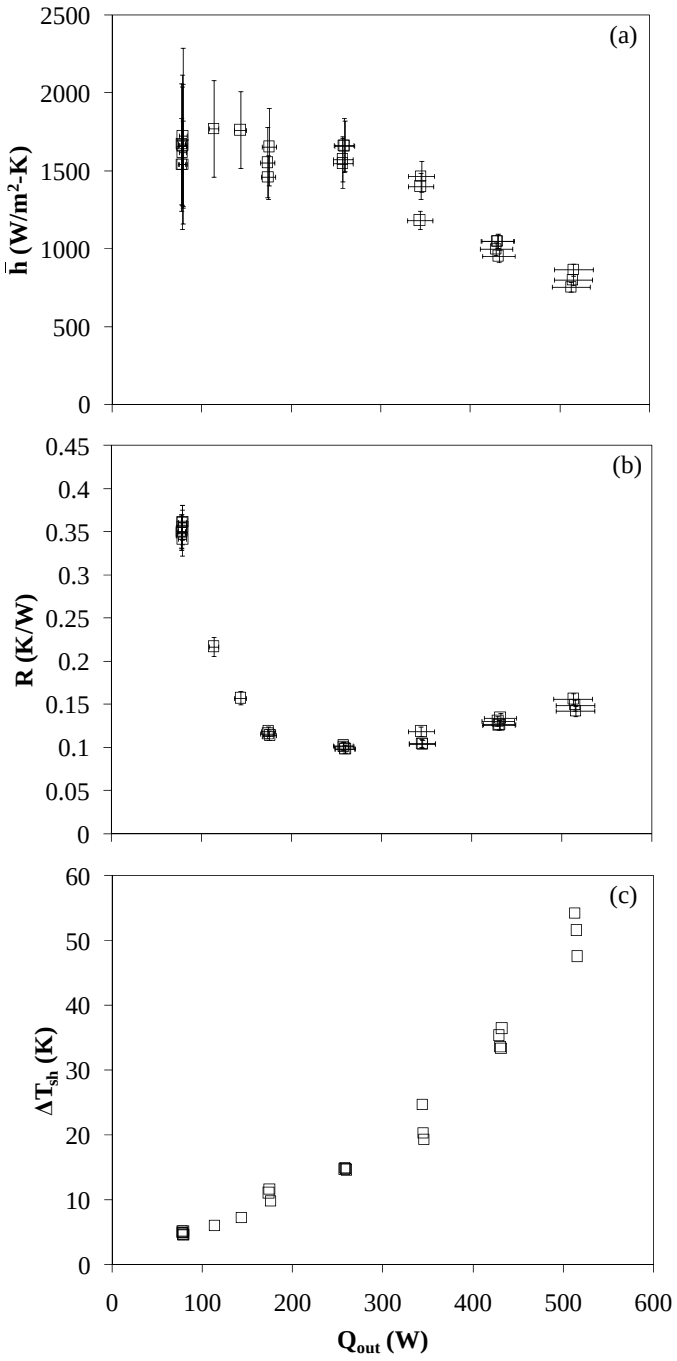


Figure 2.13. Steady state performance characteristics of the stationary LHP versus transported heat ($Q_{cc}$ = 0 W, $a_r$ = 0 g, $\dot{m}_{cp}$ = 0.0077 kg/s, $36.8 \leq \overline{T}_{cp} \leq 67.7$°C, $27.6 \leq T_{amb} \leq 38.7$°C): (a) Evaporative heat transfer coefficient; (b) Thermal resistance; (c) Wall superheat

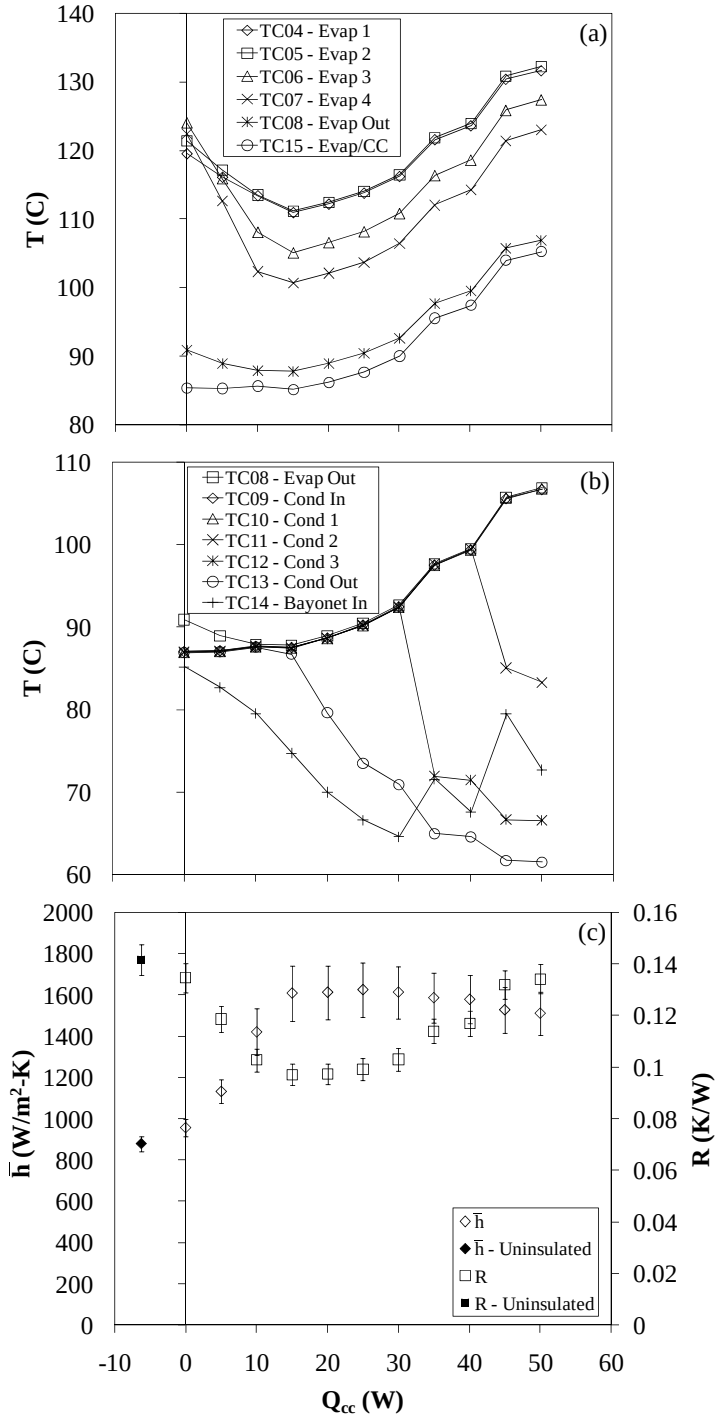


Figure 2.14. Steady state performance characteristics of the stationary LHP versus compensation chamber heat input ($Q_{in}$ = 500 W, $a_r$ = 0 g, $\dot{m}_{cp}$ = 0.0077 kg/s, 63.4 ≤ $\overline{T}_{cp}$ ≤ 64.8°C, 36.1 ≤ $T_{amb}$ ≤ 38.1°C): (a) Evaporator temperatures; (b) Condenser temperatures; (c) Evaporative heat transfer coefficient and thermal resistance.

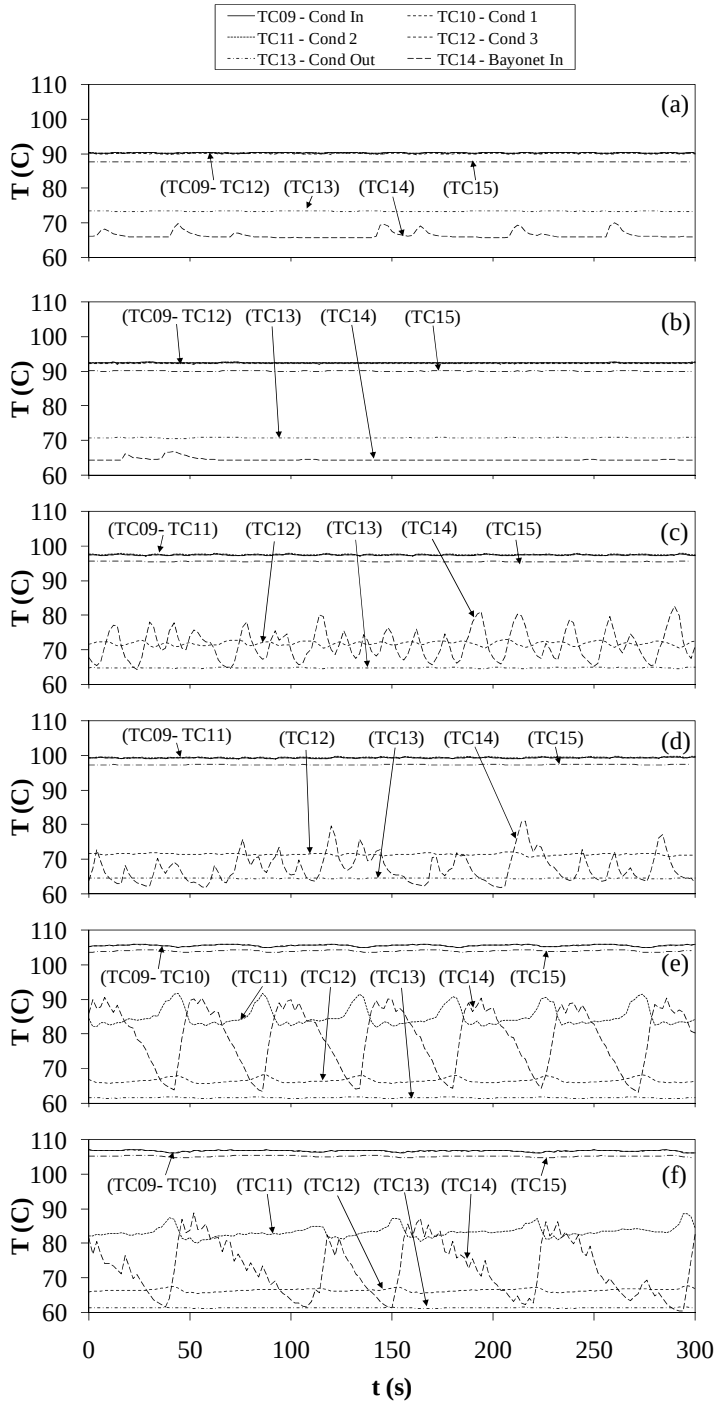


Figure 2.15. Transient temperature profiles in the condenser and bayonet tube of the stationary LHP for $Q_{cc}$ = 25 to 50 W ($Q_{in}$ = 500 W, $a_r$ = 0 g, $\dot{m}_{cp}$ = 0.0077 kg/s, 63.4 ≤ $\overline{T}_{cp}$ ≤ 64.8°C, 36.1 ≤ $T_{amb}$ ≤ 38.1°C): (a) $Q_{cc}$ = 25 W; (b) $Q_{cc}$ = 30 W; (c) $Q_{cc}$ = 35 W; (d) $Q_{cc}$ = 40 W; (e) $Q_{cc}$ = 45 W; (f) $Q_{cc}$ = 50 W.

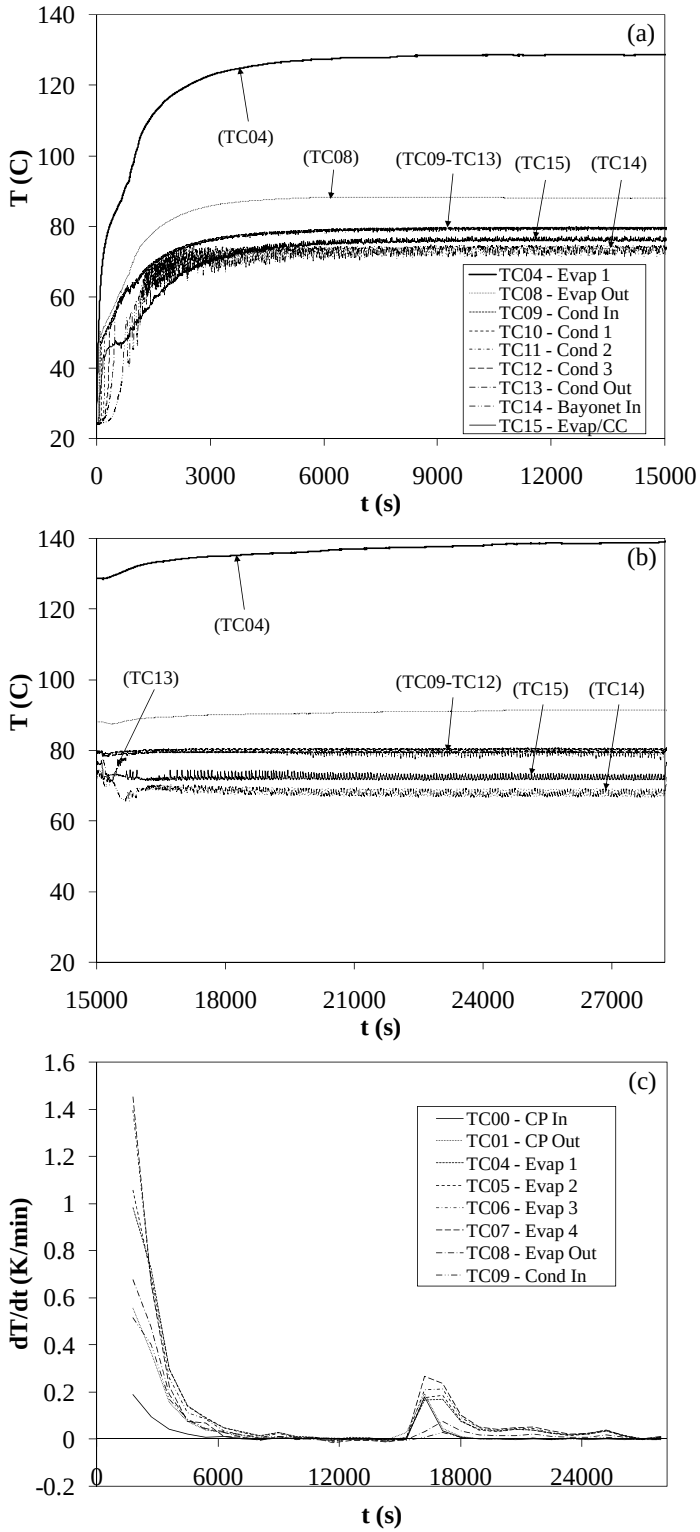


Figure 2.16. Transient temperature traces of the LHP at elevated acceleration ($Q_{in}$ = 600 W, $Q_{cc}$ = 0 W, $\dot{m}_{cp}$ = 0.0077 kg/s, 55.2 ≤ $\overline{T}_{cp}$ ≤ 59.7°C, 27.9 ≤ $T_{amb}$ ≤ 30.1°C): (a) $a_r$ = 0.1 g startup phase; (b) Transition to and steady state at $a_r$ = 10.0 g; (c) Transient rate of change of temperatures.

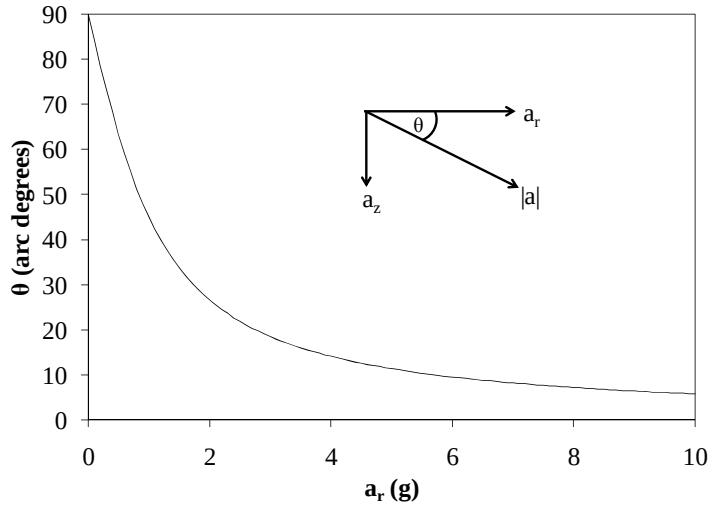


(a)

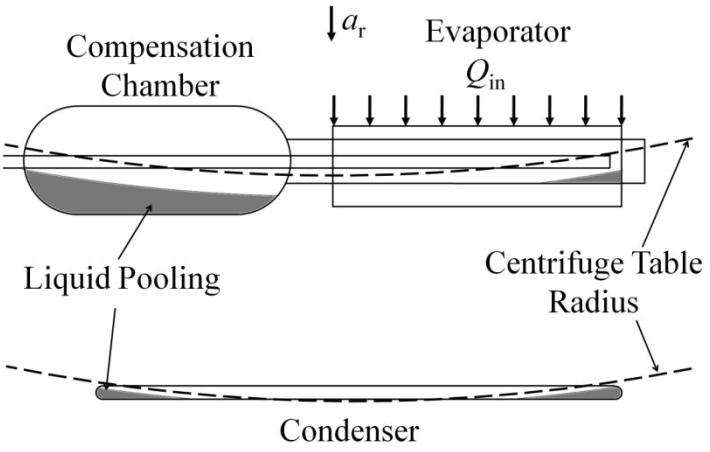


(b)

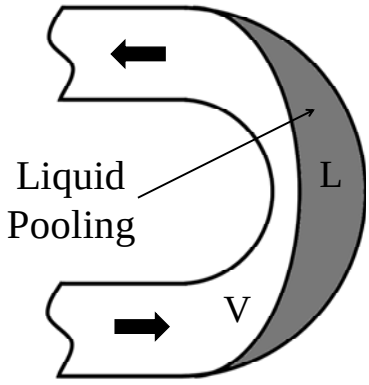


(c)

Figure 2.17. Effect of resultant acceleration vector direction on fluid distribution within the LHP: (a) Resultant acceleration vector orientation versus radial acceleration; (b) Liquid pooling in the evaporator, compensation chamber, and condenser under elevated acceleration (to scale, top view); (c) Liquid pooling in the condenser bends.

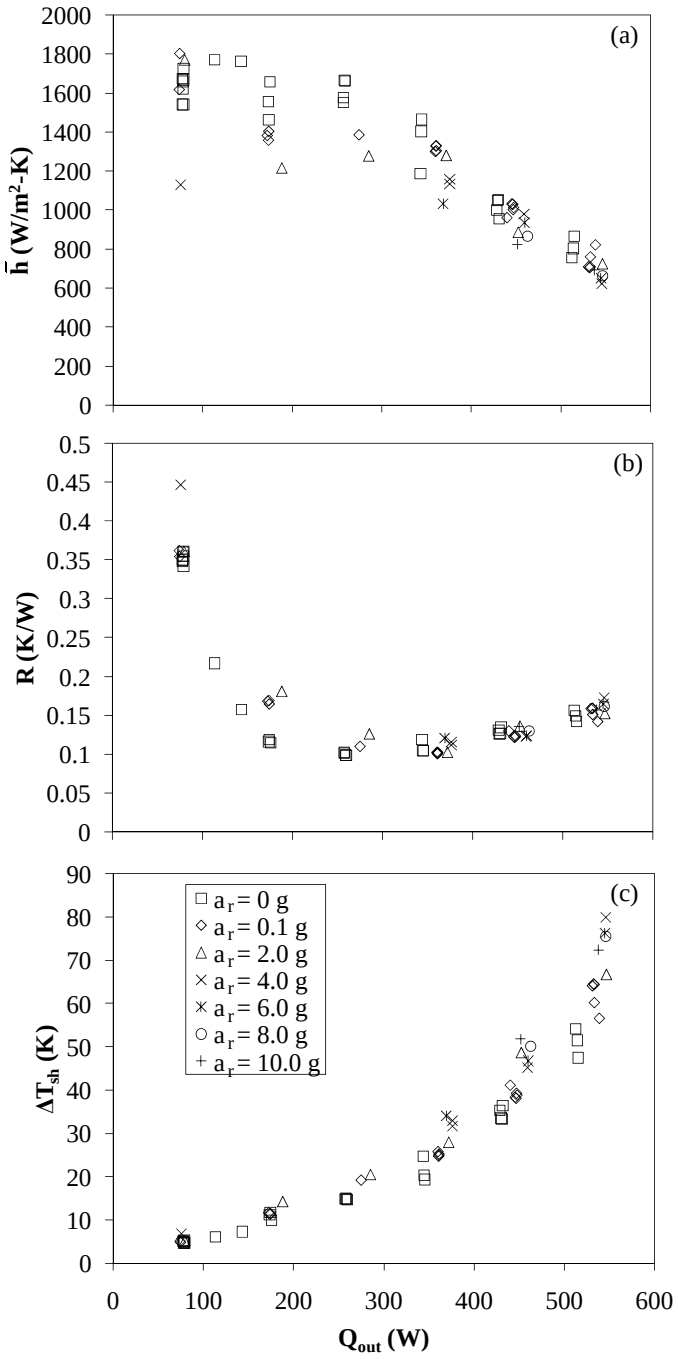


Figure 2.18. Steady state performance characteristics of the LHP versus transported heat at stationary and elevated acceleration ($Q_{cc}$ = 0 W, $\dot{m}_{cp}$ = 0.0077 kg/s, 37.2 ≤ $\overline{T}_{cp}$ ≤ 67.7°C, 25.1 ≤ $T_{amb}$ ≤ 38.7°C): (a) Evaporative heat transfer coefficient; (b) Thermal resistance; (c) Wall superheat.

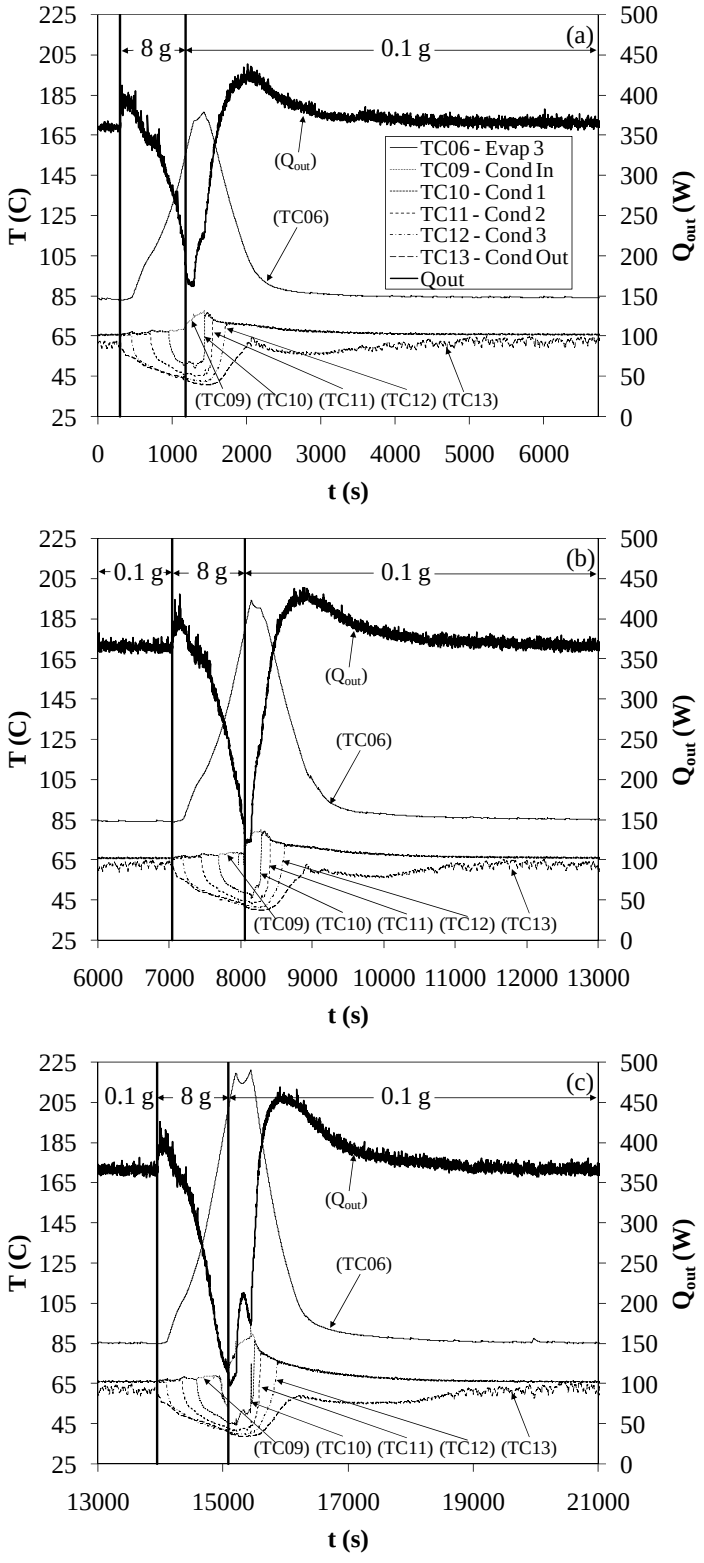


Figure 2.19. Transient temperature traces of the LHP at elevated acceleration showing dry-out behavior ($Q_{in}$ = 400 W, $Q_{cc}$ = 0 W, $\dot{m}_{cp}$ = 0.0077 kg/s, $37.2 \leq \overline{T}_{cp} \leq 59.7$°C, $T_{amb}$ = 28.0°C): (a) $T_{e,max}$ = 150°C; (b) $T_{e,max}$ = 175°C; (c) $T_{e,max}$ = 200°C.

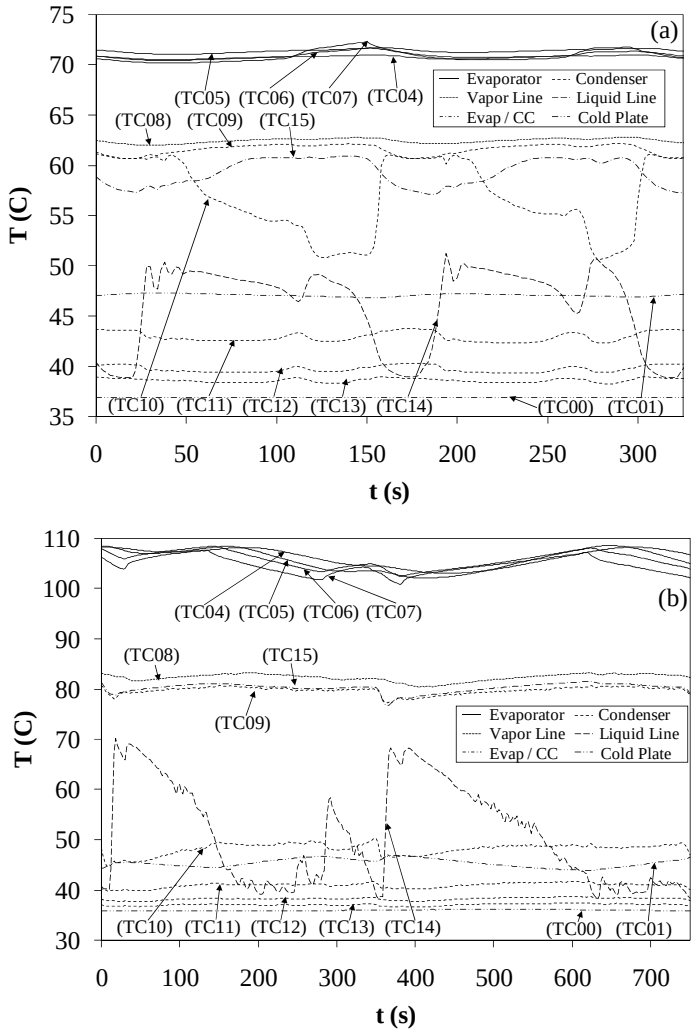


Figure 2.20. Quasi-steady state temperature traces of the LHP and cold plate at elevated acceleration for $Q_{in}$ = 200 W ($Q_{cc}$ = 0 W, $\dot{m}_{cp}$ = 0.0077 kg/s, $\overline{T}_{cp}$ = 41.9°C, $T_{amb}$ = 26.4°C): (a) Transient temperature trace at $a_r$ = 0.1 g and $t$ = 13834 s; (b) Transient temperature trace at $a_r$ = 4.0 g and $t$ = 31240 s.

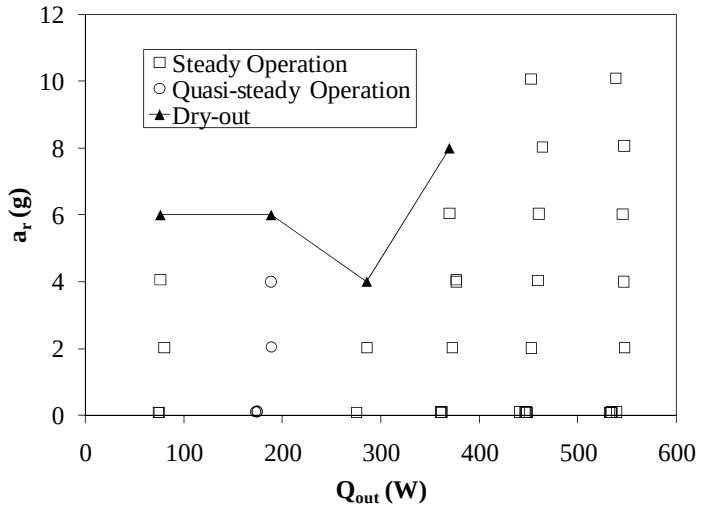


Figure 2.21. Steady state performance map of the LHP relating radial acceleration and heat transported ($Q_{cc}$ = 0 W, $\dot{m}_{cp}$ = 0.0077 kg/s, 37.2 $\leq \overline{T}_{cp} \leq$ 59.7°C, 25.1 $\leq T_{amb} \leq$ 30.2°C).

Table 2.1. AFRL/RZPS design requirements.

| Requirement | Parameter |
|---|---|
| Thermal | |
| Minimum Heat Load | 500 W |
| Minimum Heat Flux | 3 W/cm$^2$ |
| Operating Temperature | 200°C |
| Condenser Heat Sink Temperature | 5 to 140°C |
| Tilt in One G | ± 0 inches, horizontal |
| Conductance | 50°C/W |
| Proof of Pressure Test | 3102 psi (200°C) |
| Materials | |
| Evaporator Envelope Material | Titanium, CP Grade 2 |
| Evaporator Wick Material | Titanium, CP Grade 2 |
| Transport Line Material | Titanium, CP Grade 2 |
| Working Fluid | Water |
| LHP Dimensions | |
| Evaporator Configuration | 2.54 cm OD up to 25.4 cm long |
| Evaporator Footprint | 20.32 × 10.16 cm |
| Condenser Footprint | 30.48 × 28.58 cm |
| Transport Line Lengths | Approx. 243.8 cm |

Table 2.2. ACT LHP geometric design parameters.

| Transport Lines | |
|---|---|
| Vapor Line Length | Approx. 243.8 cm |
| Vapor Line Diameter | 0.9525 OD × 0.0889 cm wall |
| Liquid Line Length | Approx. 335.3 cm |
| Liquid Line Diameter | 0.6350 OD × 0.0889 cm wall |
| Condenser Line Length | Approx. 279.4 cm |
| Condenser Line Diameter | 0.9525 OD × 0.0889 cm wall |
| Compensation Chamber | |
| Diameter | 6.033 cm OD |
| Length | 11.43 cm |
| Chamber Location | Coaxial with evaporator |
| Wick Properties | |
| Effective Pore Radius | 9.1μm |
| Permeability | $1.2\times10^{-12}$ $m^2$ |
| Outside Diameter | 2.286 cm |
| Length | 20.32 cm |
| Inside Diameter | 0.8001 cm |
| Grooves | 6 |
| Groove Depth | 0.1524 cm |
| Groove Width | 0.1524 cm |

Table 2.3. Summary of LHP thermocouple locations

| Thermocouple | Location |
|---|---|
| TC04 | Evaporator 1 |
| TC05 | Evaporator 2 |
| TC06 | Evaporator 3 |
| TC07 | Evaporator 4 |
| TC08 | Evaporator Outlet |
| TC09 | Condenser Inlet |
| TC10 | Condenser 1 |
| TC11 | Condenser 2 |
| TC12 | Condenser 3 |
| TC13 | Condenser Outlet |
| TC14 | Bayonet Inlet |
| TC15 | Compensation Chamber / Evaporator |

Table 2.4. Summary of uncertainties.

| | Quantity | Uncertainty |
|---|---|---|
| Measured | Temperature | ± (fixed value + confidence interval) °C |
| | Acceleration | + (0.01 + confidence interval + ($a_{r,oe} - a_{r,cl}$)) g<br>- (0.01 + confidence interval + ($a_{r,cl} - a_{r,ie}$)) g |
| | Voltages | ± (0.00025V + 0.005 + confidence interval) V |
| Constant | Resistors | ± 0.02%$R$ Ω |
| | Wick $D$, $L$ | ± 0.0000254 m |
| Calculated | $\overline{T}_{cp}$ | ± max($\Delta T_{out}$, $\Delta T_{in}$) |
| | $\overline{T}_{e}$ | ± max(Δ(TC04), Δ(TC05), Δ(TC06), Δ(TC07)) |
| | $\Delta T_{sh}$ | ± 1.28°C |
| | $C_{p,PAO}$ | $\pm\ 0.5\% * C_p\left(\overline{T}_{cp}\right) + \left(C_p\left(\overline{T}_{cp} + \Delta\overline{T}_{cp}\right) - C_p\left(\overline{T}_{cp}\right)\right)$ |
| | $Q_{out}$ | Equation (2.8) |
| | $\overline{h}$ | Equation (2.9) |
| | $R$ | Equation (2.10) |

Table 2.5. Steady state operating characteristics for the stationary LHP ($Q_{cc}$ = 0 W, $a_r$ = 0 g, $\dot{m}_{cp}$ = 0.0077 kg/s, 36.8 ≤ $\overline{T}_{cp}$ ≤ 71.6°C, 27.6 ≤ $T_{amb}$ ≤ 38.7°C) showing effect of startup path.

| Final $Q_{in}$ (W) | Path to Final $Q_{in}$ | $\overline{T}_e$ (°C) | $T_{e/cc}$ (°C) | $\overline{T}_{cp}$ (°C) | $Q_{out}$ (W) | $\overline{h}$ (W/m$^2$-K) | $R$ (K/W) |
|---|---|---|---|---|---|---|---|
| 100 | 0-100 | 66.6 ± 0.34 | 61.8 ± 0.86 | 39.5 ± 0.12 | 79.1 ± 4.3 | 1670 ± 390 | 0.342 ± 0.019 |
| | 0-100 | 64.9 ± 0.34 | 59.9 ± 0.86 | 37.4 ± 0.12 | 78.4 ± 4.3 | 1660 ± 380 | 0.351 ± 0.020 |
| | 0-100 | 64.8 ± 0.34 | 59.8 ± 0.86 | 37.6 ± 0.12 | 77.9 ± 4.3 | 1670 ± 390 | 0.348 ± 0.020 |
| | 0-100 | 65.4 ± 0.34 | 60.1 ± 0.86 | 36.8 ± 0.12 | 79.0 ± 4.2 | 1540 ± 280 | 0.361 ± 0.020 |
| | 0-100 | 65.4 ± 0.34 | 60.2 ± 0.86 | 38.2 ± 0.12 | 77.9 ± 4.3 | 1540 ± 300 | 0.350 ± 0.020 |
| | 0-100-300-100 | 66.9 ± 0.34 | 62.2 ± 0.86 | 38.8 ± 0.12 | 79.1 ± 4.3 | 1730 ± 560 | 0.355 ± 0.020 |
| | 0-100-500-100 | 67.4 ± 0.34 | 62.6 ± 0.86 | 39.0 ± 0.12 | 78.8 ± 4.3 | 1620 ± 500 | 0.361 ± 0.020 |
| 133 | 0-100-133 | 65.1 ± 0.34 | 59.0 ± 0.86 | 40.4 ± 0.12 | 114 ± 5.5 | 1770 ± 310 | 0.217 ± 0.011 |
| 166 | 0-100-133-166 | 65.6 ± 0.34 | 58.3 ± 0.86 | 43.0 ± 0.12 | 143 ± 6.5 | 1760 ± 250 | 0.158 ± 0.0076 |
| 200 | 0-200 | 66.3 ± 0.46 | 66.3 ± 0.86 | 46.1 ± 0.12 | 174 ± 7.7 | 1560 ± 230 | 0.116 ± 0.0058 |
| | 0-200 | 66.4 ± 0.35 | 66.4 ± 0.86 | 45.7 ± 0.12 | 174 ± 7.7 | 1460 ± 140 | 0.119 ± 0.0057 |
| | 0-200 | 65.5 ± 0.34 | 65.5 ± 0.86 | 45.4 ± 0.12 | 176 ± 7.8 | 1660 ± 250 | 0.114 ± 0.0055 |

Table 2.5, continued. Steady state operating characteristics for the stationary LHP ($Q_{cc}$ = 0 W, $a_r$ = 0 g, $\dot{m}_{cp}$ = 0.0077 kg/s, 36.8 ≤ $\overline{T}_{cp}$ ≤ 71.6°C, 27.6 ≤ $T_{amb}$ ≤ 38.7°C) showing effect of startup path.

| Final $Q_{in}$ (W) | Path to Final $Q_{in}$ | $\overline{T}_e$ (°C) | $T_{e/cc}$ (°C) | $\overline{T}_{cp}$ (°C) | $Q_{out}$ (W) | $\overline{h}$ (W/m$^2$-K) | $R$ (K/W) |
|---|---|---|---|---|---|---|---|
| 300 | 0-100-300 | 77.1 ± 0.39 | 62.4 ± 0.86 | 51.6 ± 0.12 | 260 ± 11 | 1660 ± 160 | 0.0985 ± 0.0045 |
| | 0-100-300 | 75.8 ± 0.40 | 60.9 ± 0.86 | 50.2 ± 0.12 | 259 ± 11 | 1670 ± 170 | 0.0988 ± 0.0045 |
| | 0-200-300 | 78.1 ± 0.38 | 63.1 ± 0.86 | 52.0 ± 0.12 | 258 ± 11 | 1580 ± 140 | 0.101 ± 0.0046 |
| | 0-300 | 79.3 ± 0.40 | 64.4 ± 0.86 | 52.8 ± 0.12 | 258 ± 11 | 1550 ± 160 | 0.103 ± 0.0047 |
| 400 | 0-200-400 | 94.0 ± 0.34 | 73.6 ± 0.86 | 57.8 ± 0.12 | 345 ± 14 | 1400 ± 85 | 0.105 ± 0.0045 |
| | 0-300-400 | 94.3 ± 0.35 | 75.0 ± 0.86 | 58.4 ± 0.12 | 345 ± 14 | 1470 ± 98 | 0.104 ± 0.0045 |
| | 0-400 | 97.4 ± 0.34 | 72.6 ± 0.86 | 56.5 ± 0.12 | 344 ± 14 | 1190 ± 60 | 0.119 ± 0.0051 |
| 500 | 0-100-300-500 | 116 ± 0.34 | 82.4 ± 0.86 | 61.7 ± 0.12 | 430 ± 18 | 1050 ± 45 | 0.126 ± 0.0053 |
| | 0-100-500 | 119 ± 0.34 | 83.8 ± 0.86 | 63.1 ± 0.12 | 429 ± 18 | 999 ± 41 | 0.131 ± 0.0055 |
| | 0-400-500 | 117 ± 0.34 | 83.6 ± 0.86 | 62.4 ± 0.12 | 431 ± 18 | 1050 ± 47 | 0.127 ± 0.0053 |
| | 0-500 | 122 ± 0.34 | 85.3 ± 0.86 | 63.7 ± 0.12 | 432 ± 18 | 956 ± 42 | 0.135 ± 0.0057 |
| 600 | 0-200-400-600 | 145 ± 0.36 | 93.1 ± 0.86 | 67.8 ± 0.12 | 515 ± 21 | 803 ± 33 | 0.149 ± 0.0062 |
| | 0-400-500-600 | 141 ± 0.34 | 93.3 ± 0.86 | 67.5 ± 0.12 | 515 ± 21 | 867 ± 37 | 0.142 ± 0.0060 |
| | 0-600 | 148 ± 0.36 | 93.7 ± 0.86 | 67.7 ± 0.12 | 513 ± 21 | 757 ± 33 | 0.157 ± 0.0066 |

Table 2.6. Steady state operating characteristics for the stationary LHP showing effect of heat input to the compensation chamber ($Q_{in}$ = 500 W, $a_r$ = 0 g, $\dot{m}_{cp}$ = 0.0077 kg/s, 63.4 ≤ $\overline{T}_{cp}$ ≤ 64.8°C, 36.1 ≤ $T_{amb}$ ≤ 38.1°C).

| $Q_{cc}$ (W) | $\overline{T}_e$ (°C) | $T_{e/cc}$ (°C) | $\overline{T}_{cp}$ (°C) | $Q_{out}$ (W) | $\overline{h}$ (W/m$^2$-K) | $R$ (K/W) |
|---|---|---|---|---|---|---|
| 0 | 122 ± 0.34 | 85.3 ± 0.86 | 63.7 ± 0.12 | 432 ± 18 | 956 ± 42 | 0.135 ± 0.0057 |
| 5 | 115 ± 0.35 | 85.3 ± 0.86 | 63.6 ± 0.12 | 438 ± 18 | 1130 ± 58 | 0.118 ± 0.0050 |
| 10 | 109 ± 0.35 | 85.6 ± 0.86 | 63.8 ± 0.12 | 444 ± 18 | 1420 ± 110 | 0.103 ± 0.0044 |
| 15 | 107 ± 0.35 | 85.1 ± 0.86 | 63.4 ± 0.12 | 449 ± 19 | 1610 ± 130 | 0.0970 ± 0.0041 |
| 20 | 108 ± 0.34 | 86.1 ± 0.86 | 64.0 ± 0.12 | 456 ± 19 | 1610 ± 130 | 0.0972 ± 0.0041 |
| 25 | 110 ± 0.34 | 87.7 ± 0.86 | 64.2 ± 0.12 | 461 ± 19 | 1620 ± 130 | 0.0991 ± 0.0042 |
| 30 | 112 ± 0.34 | 90.0 ± 0.86 | 64.5 ± 0.12 | 466 ± 19 | 1610 ± 130 | 0.103 ± 0.0044 |
| 35 | 118 ± 0.35 | 95.5 ± 0.86 | 64.6 ± 0.12 | 468 ± 19 | 1580 ± 120 | 0.114 ± 0.0048 |
| 40 | 120 ± 0.34 | 97.4 ± 0.86 | 64.8 ± 0.12 | 473 ± 20 | 1580 ± 120 | 0.117 ± 0.0049 |
| 45 | 127 ± 0.34 | 104 ± 0.86 | 64.5 ± 0.12 | 475 ± 20 | 1530 ± 110 | 0.132 ± 0.0055 |
| 50 | 129 ± 0.35 | 105 ± 0.86 | 64.5 ± 0.12 | 477 ± 20 | 1510 ± 110 | 0.134 ± 0.0056 |

Table 2.7. The effect of compensation chamber temperature control on LHP operation ($Q_{in}$ = 500 W, $a_r$ = 0 g, $\dot{m}_{cp}$ = 0.0077 kg/s, $\overline{T}_{cp}$ = 52.5°C, $T_{amb}$ = 26.4°C)

| Compensation Chamber Conditions | $Q_{cc}$ (W) | $\overline{T}_e$ (°C) | $\overline{T}_{cp}$ (°C) | $T_{cc}$ (°C) | $Q_{out}$ (W) | $\overline{h}$ (W/m$^2$-K) | $R$ (K/W) | Time to Steady State |
|---|---|---|---|---|---|---|---|---|
| Uninsulated, no temperature control | 0 | 115 | 52.4 | 59.3 | 442 ± 19 | 878 ± 37 | 0.142 ± 0.0060 | 300 min. |
| Insulated, no temperature control | 0 | 107 | 52.6 | 62.9 | 447 ± 19 | 1050 ± 51 | 0.122 ± 0.0052 | 375 min. |
| Insulated, temperature controlled to $T_{cc}$ = 72.8°C, simultaneous heat input startup | 20 | 103 | 53.5 | 72.8 | 470 ± 20 | 1340 ± 77 | 0.106 ± 0.0045 | 310 min. |
| Insulated, temperature controlled to $T_{cc}$ = 72.8°C, preconditioned CC | 100 decreased to 20 | 103 | 53.4 | 72.8 | 467 ± 19 | 1350 ± 77 | 0.106 ± 0.0045 | 250 min. |

Table 2.8. Steady state operating characteristics of the rotating LHP ($Q_{cc}$ = 0 W, $\dot{m}_{cp}$ = 0.0077 kg/s, 37.2 ≤ $\overline{T}_{cp}$ ≤ 59.7°C, 25.1 ≤ $T_{amb}$ ≤ 30.2°C).

| $Q_{in}$ (W) | $a_r$ (g) | $\overline{T}_e$ (°C) | $T_{e/cc}$ (°C) | $\overline{T}_{cp}$ (°C) | $Q_{out}$ (W) | $\overline{h}$ (W/m$^2$-K) | $R$ (K/W) |
|---|---|---|---|---|---|---|---|
| 100 | 0.1 ± 0.012 | 64.9 ± 0.34 | 59.8 ± 0.86 | 38.0 ± 0.12 | 74.2 ± 4.2 | 1620 ± 340 | 0.362 ± 0.021 |
| 100 | 0.1 ± 0.012 | 64.6 ± 0.34 | 59.8 ± 0.86 | 38.1 ± 0.12 | 74.6 ± 4.2 | 1810 ± 510 | 0.355 ± 0.020 |
| 100 | 2.0 ± 0.050 | 66.4 ± 0.34 | 61.2 ± 0.86 | 37.5 ± 0.12 | 79.9 ± 4.5 | 1770 ± 420 | 0.361 ± 0.021 |
| 100 | 4.1 ± 0.091 | 71.2 ± 0.44 | 64.3 ± 0.86 | 37.2 ± 0.16 | 76.1 ± 4.8 | 1130 ± 150 | 0.446 ± 0.029 |
| 200 | 0.1 ± 0.012 | 70.8 ± 0.41 | 59.3 ± 0.86 | 42.0 ± 0.13 | 174 ± 7.8 | 1400 ± 110 | 0.165 ± 0.0078 |
| 200 | 0.1 ± 0.012 | 71.1 ± 0.43 | 59.5 ± 0.86 | 41.9 ± 0.13 | 172 ± 7.8 | 1380 ± 110 | 0.169 ± 0.0081 |
| 200 | 0.1 ± 0.012 | 71.5 ± 0.38 | 60.3 ± 0.86 | 42.0 ± 0.12 | 174 ± 7.8 | 1360 ± 110 | 0.170 ± 0.0079 |
| 200 | 2.0 ± 0.050 | 75.8 ± 0.65 | 61.6 ± 0.86 | 41.7 ± 0.21 | 188 ± 9.2 | 1220 ± 86 | 0.181 ± 0.0096 |
| 300 | 0.1 ± 0.012 | 76.4 ± 0.48 | 57.2 ± 0.86 | 46.0 ± 0.12 | 275 ± 12 | 1390 ± 100 | 0.111 ± 0.0051 |
| 300 | 2.0 ± 0.050 | 81.7 ± 0.76 | 61.2 ± 0.86 | 45.6 ± 0.16 | 285 ± 13 | 1280 ± 80 | 0.126 ± 0.0063 |
| 400 | 0.1 ± 0.012 | 86.4 ± 0.39 | 60.6 ± 0.86 | 49.3 ± 0.12 | 360 ± 15 | 1300 ± 82 | 0.103 ± 0.0045 |
| 400 | 0.1 ± 0.012 | 86.6 ± 0.39 | 61.3 ± 0.86 | 49.3 ± 0.12 | 361 ± 15 | 1300 ± 81 | 0.103 ± 0.0045 |
| 400 | 0.1 ± 0.012 | 86.1 ± 0.39 | 61.1 ± 0.86 | 49.3 ± 0.12 | 361 ± 15 | 1330 ± 84 | 0.102 ± 0.0044 |
| 400 | 0.1 ± 0.012 | 85.8 ± 0.42 | 61.1 ± 0.86 | 49.3 ± 0.12 | 361 ± 15 | 1330 ± 89 | 0.101 ± 0.0044 |
| 400 | 2.0 ± 0.050 | 87.6 ± 0.42 | 59.7 ± 0.86 | 49.3 ± 0.12 | 372 ± 16 | 1280 ± 74 | 0.103 ± 0.0045 |
| 400 | 4.0 ± 0.089 | 91.5 ± 0.43 | 59.8 ± 0.86 | 49.3 ± 0.12 | 376 ± 16 | 1160 ± 56 | 0.112 ± 0.0051 |
| 400 | 4.1 ± 0.091 | 93.0 ± 0.63 | 60.0 ± 0.86 | 49.3 ± 0.15 | 376 ± 17 | 1130 ± 59 | 0.116 ± 0.0055 |
| 400 | 6.0 ± 0.13 | 94.8 ± 0.34 | 60.7 ± 0.86 | 49.9 ± 0.12 | 369 ± 16 | 1030 ± 46 | 0.122 ± 0.0053 |

Table 2.8, continued. Steady state operating characteristics of the rotating LHP ($Q_{cc}$ = 0 W, $\dot{m}_{cp}$ = 0.0077 kg/s, 37.2 ≤ $\overline{T}_{cp}$ ≤ 59.7°C, 25.1 ≤ $T_{amb}$ ≤ 30.2°C).

| $Q_{in}$ (W) | $a_r$ (g) | $\overline{T}_e$ (°C) | $T_{e/cc}$ (°C) | $\overline{T}_{cp}$ (°C) | $Q_{out}$ (W) | $\overline{h}$ (W/m$^2$-K) | $R$ (K/W) |
|---|---|---|---|---|---|---|---|
| 500 | 0.1 ± 0.012 | 110 ± 0.36 | 69.3 ± 0.86 | 52.9 ± 0.12 | 440 ± 18 | 960 ± 43 | 0.131 ± 0.0055 |
| 500 | 0.1 ± 0.012 | 107 ± 0.35 | 69.0 ± 0.86 | 52.6 ± 0.12 | 446 ± 19 | 1030 ± 48 | 0.123 ± 0.0052 |
| 500 | 0.1 ± 0.012 | 107 ± 0.41 | 69.2 ± 0.86 | 52.7 ± 0.12 | 447 ± 19 | 1030 ± 50 | 0.122 ± 0.0052 |
| 500 | 0.1 ± 0.012 | 109 ± 0.42 | 69.5 ± 0.86 | 52.9 ± 0.12 | 447 ± 19 | 1000 ± 46 | 0.125 ± 0.0053 |
| 500 | 0.1 ± 0.012 | 108 ± 0.35 | 68.9 ± 0.86 | 52.6 ± 0.12 | 448 ± 19 | 1010 ± 47 | 0.123 ± 0.0052 |
| 500 | 2.0 ± 0.050 | 114 ± 0.42 | 65.5 ± 0.86 | 52.5 ± 0.12 | 452 ± 19 | 887 ± 37 | 0.136 ± 0.0058 |
| 500 | 4.0 ± 0.090 | 110 ± 0.34 | 64.4 ± 0.86 | 53.1 ± 0.13 | 459 ± 19 | 982 ± 43 | 0.123 ± 0.0053 |
| 500 | 6.0 ± 0.13 | 111 ± 0.34 | 64.6 ± 0.86 | 54.0 ± 0.13 | 460 ± 20 | 934 ± 42 | 0.125 ± 0.0055 |
| 500 | 8.0 ± 0.17 | 115 ± 0.34 | 65.1 ± 0.86 | 54.8 ± 0.12 | 463 ± 20 | 865 ± 38 | 0.131 ± 0.0058 |
| 500 | 10 ± 0.21 | 117 ± 0.34 | 64.7 ± 0.86 | 55.2 ± 0.12 | 452 ± 20 | 824 ± 35 | 0.136 ± 0.0060 |
| 600 | 0.1 ± 0.012 | 137 ± 0.36 | 76.6 ± 0.86 | 56.0 ± 0.12 | 533 ± 22 | 759 ± 32 | 0.152 ± 0.0063 |
| 600 | 0.1 ± 0.012 | 141 ± 0.43 | 76.6 ± 0.86 | 55.9 ± 0.12 | 533 ± 22 | 707 ± 29 | 0.160 ± 0.0067 |
| 600 | 0.1 ± 0.012 | 141 ± 0.43 | 76.3 ± 0.86 | 55.8 ± 0.12 | 533 ± 22 | 703 ± 29 | 0.160 ± 0.0067 |
| 600 | 0.1 ± 0.012 | 140 ± 0.42 | 76.2 ± 0.86 | 55.8 ± 0.12 | 531 ± 22 | 707 ± 30 | 0.159 ± 0.0067 |
| 600 | 0.1 ± 0.012 | 133 ± 0.34 | 76.2 ± 0.86 | 56.0 ± 0.12 | 539 ± 23 | 821 ± 35 | 0.143 ± 0.0060 |
| 600 | 2.0 ± 0.050 | 140 ± 0.34 | 72.9 ± 0.86 | 56.3 ± 0.12 | 547 ± 24 | 726 ± 31 | 0.152 ± 0.0066 |
| 600 | 4.0 ± 0.090 | 152 ± 0.50 | 71.7 ± 0.86 | 57.1 ± 0.12 | 546 ± 23 | 621 ± 26 | 0.173 ± 0.0075 |
| 600 | 6.0 ± 0.13 | 148 ± 0.34 | 71.5 ± 0.86 | 57.8 ± 0.12 | 545 ± 24 | 651 ± 27 | 0.165 ± 0.0072 |
| 600 | 8.1 ± 0.17 | 147 ± 0.34 | 71.8 ± 0.86 | 58.8 ± 0.12 | 546 ± 24 | 662 ± 28 | 0.162 ± 0.0072 |
| 600 | 10 ± 0.21 | 145 ± 0.34 | 72.2 ± 0.86 | 59.7 ± 0.13 | 538 ± 24 | 691 ± 29 | 0.158 ± 0.0070 |

Table 2.9. Comparison of quasi-steady states for $Q_{in}$ = 200 W ($Q_{cc}$ = 0 W, $\dot{m}_{cp}$ = 0.0077 kg/s).

| $a_r$ (g) | 0 | 0.1 | Δ |
|---|---|---|---|
| $T_{amb}$ (°C) | 31.7 | 26.4 | -5.3 |
| $T_{cp,in}$ (°C) | 41.1 | 36.9 | -4.2 |
| $T_{cp,out}$ (°C) | 51.1 | 47.0 | -4.1 |
| $\overline{T}_{cp}$ (°C) | 46.1 | 41.9 | -4.2 |
| $\overline{T}_{e}$ (°C) | 66.3 | 71.1 | 4.8 |
| $T_{bayonet\ inlet,max}$ (°C) | 50.7 | 51.2 | 0.5 |
| $T_{bayonet\ inlet,min}$ (°C) | 42.6 | 38.9 | -3.7 |
| $T_{e/cc,max}$ (°C) | 56.8 | 60.9 | 4.1 |
| $T_{e/cc,min}$ (°C) | 54.0 | 57.1 | 3.1 |
| $h$ (W/m$^2$-K) | 1560 | 1380 | -180 |
| $R$ (W/K) | 0.116 | 0.169 | 0.053 |
| $\Delta T_{sh}$ (°C) | 11.2 | 11.6 | 0.4 |

## REFERENCES


Anderson, J. *Introduction to Flight.* Boston: McGraw-Hill, 2000.

Boyer, R., Welsch, G., Collings, E. *Materials Properties Handbook: Titanium Alloys.* Materials Park, OH: ASM International, 1994.

Cimbala, J., Brenizer, J., Chuang, A., Hanna, S., Conroy, C., El-Ganayni, A., Riley, D. "Study of a Loop Heat Pipe Using Neutron Radiography." *Applied Radiation and Isotopes 61*, 2004: 701-705.

Cloyd, J. "A Status of the United States Air Force's More Electric Aircraft Initiative." *Energy Conversion Engineering Conference.* Honolulu, HI: IEEE, 1997. 681-686.

DOD. *MIL-HDBK-310: Global Climatic Data for Developing Military Products.* 1997.

Douglas, D., Ku, J., Kaya, T. "Testing of the Geoscience Laser Altimeter System (GLAS) Prototype Loop Heat Pipe." *37th AIAA Aerospace Sciences Meeting and Exhibit.* Reno, NV: AIAA, 1999. AIAA 99-0473.

Faghri, A. *Heat Pipe Science and Technology.* Washington D.C.: Taylor and Francis, 1995.

Ghajar, A., Tang, W., Beam, J. "Comparison of Hydraulic and Thermal Performance of PAO and Coolanol 25R." *6th AIAA/ASME Joint Thermophysics and Heat Transfer Conference.* Colorado Springs, CO: AIAA, 1994. AIAA-94-1965.

Hoang, T., Ku, J. "Transient Modeling of Loop Heat Pipes." *1st International Energy Conversion Engineering Conference.* Portsmouth, VA: AIAA, 2003. AIAA 2003-6082.

Incropera, F., DeWitt, D. *Fundamentals of Heat and Mass Transfer.* New York City: Wiley, 2002.

Kaya, T., Hoang, T., Ku, J., Cheung, M. "Mathematical Modeling of Loop Heat Pipes." *37th AIAA Aerospace Sciences Meeting and Exhibit.* Reno, NV: AIAA, 1999. A99-16362.

Kaya, T., Ku, J. "Experimental Investigation of Performance Characteristics of Small Loop Heat Pipes." *Proceedings of 41st Aerospace Sciences Meeting and Exhibit.* Reno, NV: AIAA, 2003. AIAA 2003-1038.

Ku, J. "Operating Characteristics of Loop Heat Pipes." *29th International Conference on Environmental System.* Denver, CO: SAE, 1999. 1999-01-2007.

Ku, J., Ottenstein, L., Kaya, T., Rogers, P., Hoff, C. "Testing of a Loop Heat Pipe Subjected to Variable Accelerating Forces, Part 1: Start-Up." *SAE*, 2000a: 2000-01-2488.

Ku, J., Ottenstein, L., Kaya, T., Rogers, P., Hoff, C. "Testing of a Loop Heat Pipe Subjected to Variable Accelerating Forces, Part 2: Temperature Stability." *SAE*, 2000b: 2000-01-2489.

Maidanik, J. "Review: Loop Heat Pipes." *Applied Thermal Engineering 25*, 2005: 635-657.

Maidanik, J., Vershinin, S., Kholodov, V., Dolgirev, J. Heat Transfer Apparatus. United States Patent 4,515,209. 1985.

Montgomery, D., Runger, G. *Applied Statistics and Probability for Engineers.* New York City: Wiley, 2003.

NACA. *Report 1135: Equations, Tables, and Charts for Compressible Flow.* Washington, D.C.: U.S. Government Printing Office, 1953.

Ponnappan, R., Yerkes, K., Chang, W., Beam, J. "Analysis and Testing of Heat Pipe in Accelerating Environment." *Proceedings of the 8th International Heat Pipe Conference.* Beijing, China, 1992. B-19-1 - B-19-6.

Quigley, R. "More Electric Aircraft." *Applied Power Electronics Conference and Exposition.* San Diego, CA: IEEE, 1993. 906-911.

Thomas, S., Klasing, K., Yerkes, K. "The Effects of Transverse Acceleration-Induced Body Forces on the Capillary Limit of Helically Grooved Heat Pipes." *ASME Journal of Heat Transfer, 120*, 1998: 441-451.

Thomas, S., Yerkes, K. "Quasi-Steady-State Performace of a Heat Pipe Subjected to Transient Acceleration Loadings." *AIAA Journal of Thermophysics, Vol. 11, No. 2*, 1996: 306-309.

Vrable, D., Yerkes, K. "A Thermal Management Concept for More Electric Aircraft Power System Applications." *Aerospace Power Systems Conference Proceedings.* Williamsburg, VA: SAE, 1998. P-322.

White, F. *Heat and Mass Transfer*. New York City: Addison-Wesley, 1988.

Yerkes, K., Beam, J. "Arterial Heat Pipe Performance in a Transient Heat Flux and Body Force Environment." *SAE*, 1992: 921944.

Zaghdoudi, M., Sarno, C. "Investigation of the Effects of Body Force Environment on Flat Heat Pipes." *AIAA Journal of Thermophysics and Heat Transfer, Vol. 15, No. 4*, 2001: 384-394.

# APPENDIX A. OPERATING PROCEDURES

## A.1. Standard Operating Procedure

0. Ensure the main power breaker is in the "OFF" position. The breaker is located on the 71B H-bay second floor landing. See Figure A.1 for picture. Ensure the control panel box is in "Man" mode, potentiometer is set to zero (turned completely counter-clockwise), and the E-stop button has been depressed. The control panel box is located in Control Room 2. See Figure A.2 for picture of control panel box.

1. Mount test payload with sufficient factor of safety to ensure a reliable mounting configuration consistent with the generated forces. The retaining method will be designed for a payload mass subjected to a maximum table capacity of 12 g.

2. Mount the appropriate counter balance weight at the appropriate location to place the centroid in the center of the table and level each spoke to minimize vibrational noise and table runout.

3. Ensure all centrifuge maintenance has been completed.

4. Software Startup Procedure
    a. Open the LabVIEW VI file needed to control the data acquisition and table voltage.
    b. It is up to the experimentalist to write the program used to control data acquisition and table voltage. Sample programs that perform these tasks are available. See Figure A.3 for sample.
    c. Press the 'SYSTEM ENABLED' button on the front panel so that it is illuminated.
    d. Press the 'Run' button located in the top-left of the LabVIEW toolbar. This will cause the program to become functional.

5. Prior to each set of experimental testing:
    a. Check all bolts to ensure all experimental apparatus are tightened properly.

b. Clear the table of foreign objects, including removing all tools and placing in the appropriate CTK. Ensure all free standing equipment and furniture are securely placed along the perimeter of the room.

c. Turn table power switch on. This provides power to the instrumentation and devices on the table. See Figure A.4 for location.

d. Check out instrumentation for proper operation.

e. Turn on recirculating chiller located on the east wall. See Figure A.5 for picture. Check chill bath coolant flows and flow rates of any intermediate flow loops. A booster pump for the chill bath coolant is available. Follow the chill bath plumbing schematic in Figure A.6 to enable operation. The booster pump control is remotely located in Control Room 2. See Figure A.7 for picture.

f. Lock inter-connect door.

g. Check camera operation.

h. Make final check on the table for tools or loose objects.

6. Unlock main power breaker and flip to 'ON' position. See Figure A.1 for location.

a. Ensure the emergency stop button is activated and the potentiometer is turned completely counter-clockwise on the control panel box prior to proceeding with powering the centrifuge table motor.

b. Turn on warning beacon and evacuate personnel. Warning beacon switches are located outside Test Cell 4 and on the west wall of control room 1.

c. Engage table motor control switch on the north wall (cooling motor will be operational). See Figure A.8 for location.

d. Secure outer doors.

e. Place "Test in Progress Do Not Enter" sign on the outer door.

7. Controlling the System

a. To control the voltage supplied to the table, turn the mode switch from 'MAN' to 'AUTO' on the control panel box and flip the 'Table Voltage' switch to the 'ON' position. While the 'Table Voltage' switch is 'ON',

the voltage can be adjusted using the slider bar on the left side called 'Table Voltage'. Table voltage can be turned on and off as often as desired while the system is engaged.

8. Conduct test procedure. Test procedures are experiment dependent and up to the experimentalist to develop.

9. Shutdown

   a. Slowly reduce the table voltage to zero using the slider bar. Flip the 'Table Voltage' switch to the 'OFF' position on the LabVIEW VI.

   b. On the control panel box, turn the switch from 'AUTO' to 'MAN' and press the 'STOP' button. Wait for the table to stop rotating then press the 'E-STOP' button.

   c. Press the 'SYSTEM ENABLED' button on the LabVIEW VI so that it is no longer illuminated. The program will stop.

10. Emergency Shutdown

   a. If for any reason an emergency should occur press the 'E-STOP' on the control panel box. Should the table "run away" or suddenly accelerate the motor will automatically shutdown. Contact the appropriate personnel prior to a restart after an emergency shutdown.

      - Andrew Fleming 58942
      - Larry Byrd 53238
      - Travis Michalak 64429

**A.2. Test Procedures**

1. Stationary Operation

   a. Set chiller to $T_{eg}$ = 35°C. Allow to come to steady state.

   b. Turn high temperature coolant loop on and set to $\dot{m}$ = 0.0077 kg/s. Simultaneously, apply desired heat load to evaporator.

   c. Allow LHP to achieve steady state operation by examining d$T$/d$t$ plot of TC00, TC01, TC04, TC05, TC06, TC07, TC08, and TC09. Steady state is achieved when all of these thermocouples are bracketed by $-0.01 \leq dT/dt \leq 0.01$ K/min.

d. Remove heat load from the evaporator and turn off the high temperature coolant loop or adjust to next desired heat load and repeat (c).

2. Rotational Operation

a. Set chiller to $T_{eg}$ = 35°C. Allow to come to steady state.

b. Increase radial acceleration to $a_r$ = 0.1 g.

c. Turn high temperature coolant loop on and set to $\dot{m}$ = 0.0077 kg/s. Simultaneously, apply desired heat load to evaporator.

d. Allow LHP to achieve steady state operation by examining d$T$/d$t$ plot of TC00, TC01, TC04, TC05, TC06, TC07, TC08, and TC09. Steady state is achieved when all of these thermocouples are bracketed by $-0.01 \leq dT/dt \leq 0.01$ K/min.

e. Increase radial acceleration to desired level.

f. Again, allow LHP to achieve steady state operation by examining d$T$/d$t$ plot of TC00, TC01, TC04, TC05, TC06, TC07, TC08, and TC09. Steady state is achieved when all of these thermocouples are bracketed by $-0.01 \leq dT/dt \leq 0.01$ K/min.

g. Decrease radial acceleration to $a_r$ = 0.1 g.

h. If shutting down, allow LHP to operate for 30 min., then remove heat load from the evaporator and turn off the high temperature coolant. Decrease radial acceleration to $a_r$ = 0.0 g. If continuing testing, allow LHP to achieve steady state operation by examining d$T$/d$t$ plot of TC00, TC01, TC04, TC05, TC06, TC07, TC08, and TC09. Steady state is achieved when all of these thermocouples are bracketed by $-0.01 \leq dT/dt \leq 0.01$ K/min. Repeat (e)-(h).

(a)


(b)

Figure A.1. Centrifuge table main power breaker: (a) Electrical panel MCC-6; (b) Centrifuge table main power breaker.

Figure A.2. Centrifuge table control panel box.

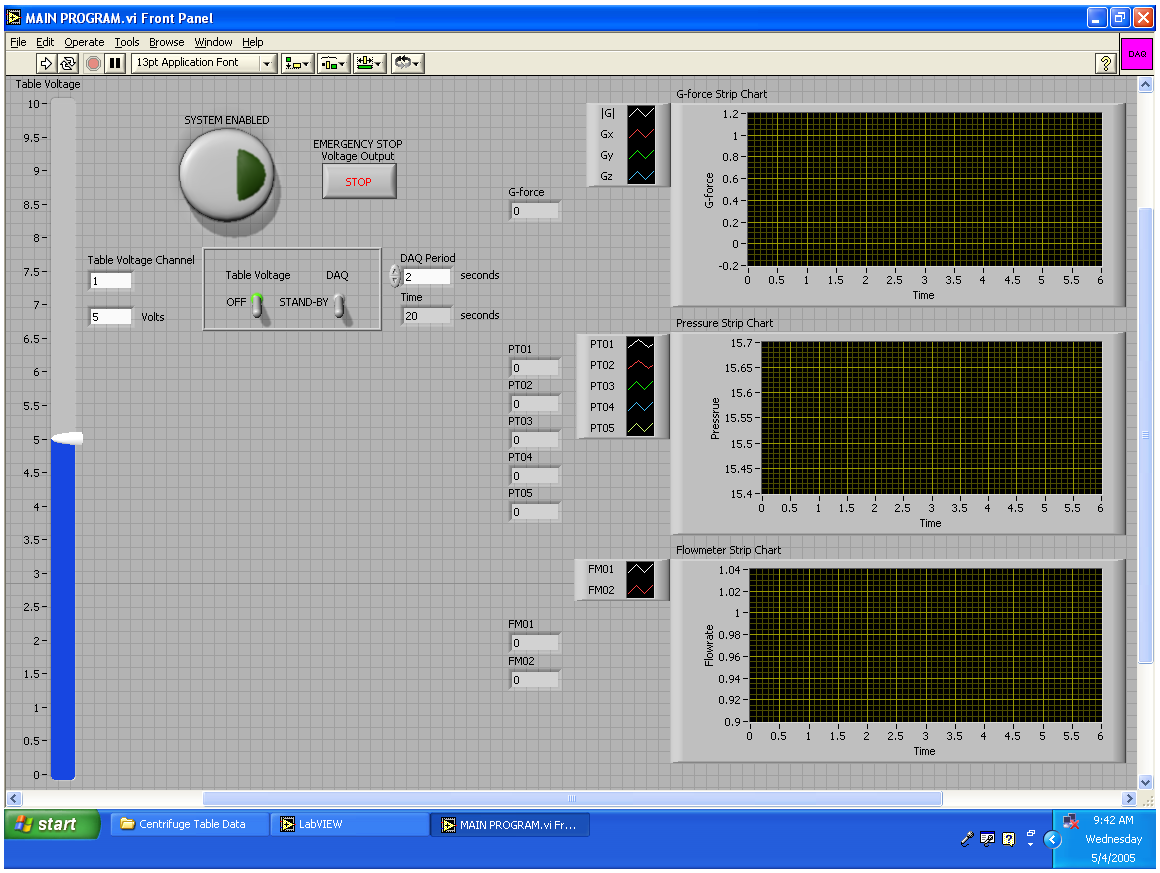

Figure A.3. Sample LabVIEW control program.

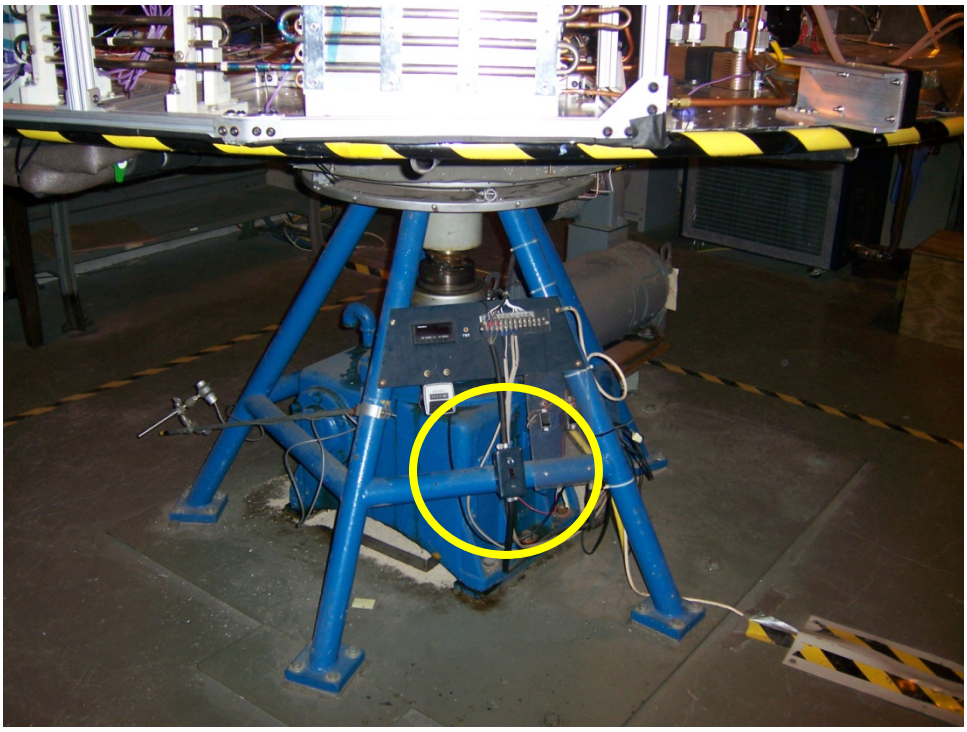

Figure A.4. Centrifuge table power switch.

Figure A.5. Neslab recirculating chiller.

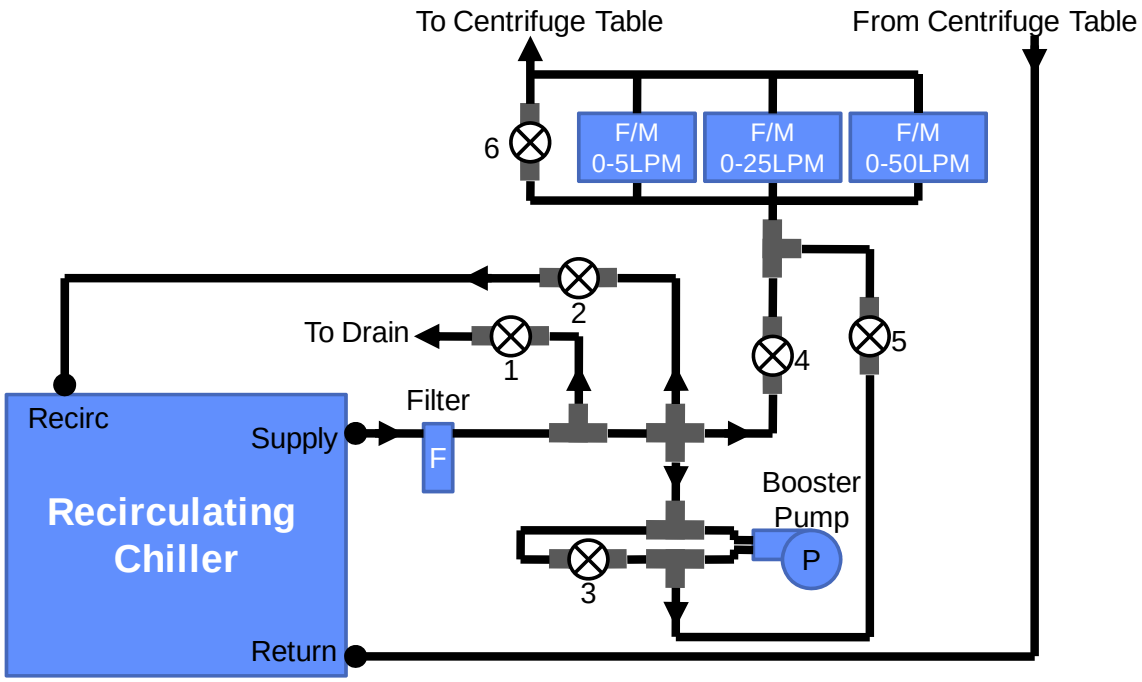


Figure A.6. Chill bath plumbing schematic.

Figure A.7. Booster pump control panel.

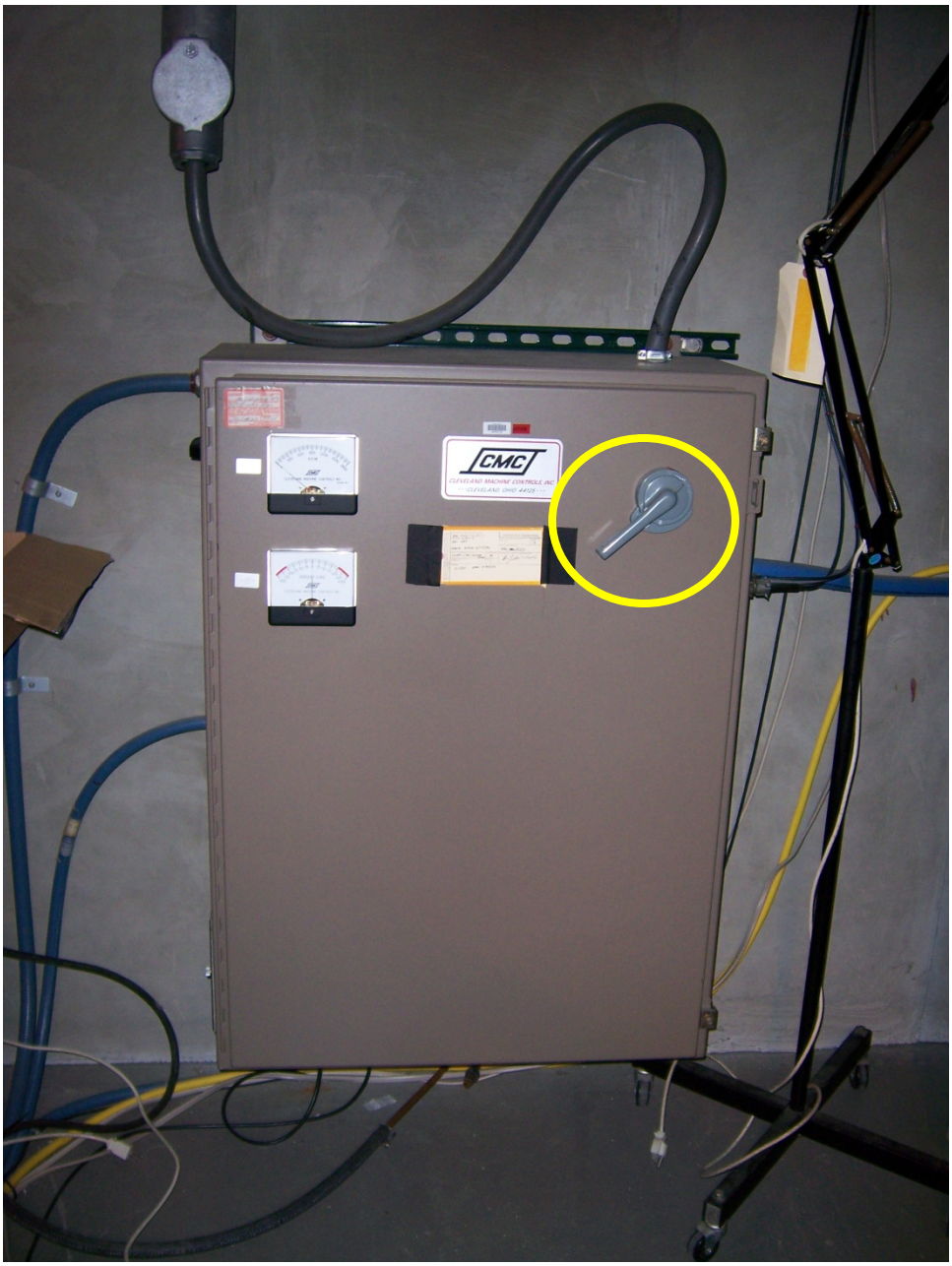

Figure A.8. Centrifuge table motor control power switch.

## APPENDIX B. UNCERTAINTY ANALYSIS

The uncertainty analysis for this experiment was broken into the following three different categories: measured, constant, and calculated quantities. For each steady state condition, 151 data points were collected representing five minutes of data. Measured values were averaged and uncertainties were calculated based on the fixed error of each instrument plus the confidence interval for the average. The fixed error for thermocouples and mass flow meter was determined via the calibration methods and can be seen in Appendix C. The fixed error of the accelerometer was ±0.1 g and ±0.00025*V + 0.005 volts for voltage measurements. The confidence interval was based off a statistical t-distribution with confidence level of 0.95 and was given by Montgomery (Montgomery, 2003)

$$\text{Confidence Interval} = \pm t\left(\frac{\sigma}{\sqrt{n}}\right) \tag{B.1}$$

where $t$ is a tabulated value based on the confidence level and number of degrees of freedom, $\sigma$ is the sample standard deviation, and $n$ is the number of data points in the sample. Constant quantities included precision resistors used for current measurement for heat input via evaporator, compensation chamber, and preheater with an uncertainty of ±0.02% and wick diameter and length measurements, with an uncertainty of ±0.0000254 m. Calculated quantities used uncertainty methods that would be the most conservative for the experiment. For averaged quantities including $\overline{T}_{\text{cp}}$, $\overline{T}_{\text{e}}$, and $\overline{h}$, the largest uncertainty of the individual measurements was used as the uncertainty of the average value. For the specific heat of PAO, the uncertainty was 0.5% of the total value plus difference between the specific heat using the upper limit of the temperature measurement and the average specific heat. The calorimetry of the cold plate, $Q_{\text{out}}$, was given by

$$Q_{\text{out}} = \dot{m} C_{\text{p,PAO}}(T_{\text{out}} - T_{\text{in}}) \tag{B.2}$$

The uncertainty of $Q_{\text{out}}$ was determined to be

$$\Delta Q_{\text{out}} = \left[\left(\frac{\partial Q_{\text{out}}}{\partial \dot{m}}\Delta\dot{m}\right)^2 + \left(\frac{\partial Q_{\text{out}}}{\partial C_{\text{p,PAO}}}\Delta C_{\text{p,PAO}}\right)^2 + \left(\frac{\partial Q_{\text{out}}}{\partial T_{\text{out}}}\Delta T_{\text{out}}\right)^2 + \left(\frac{\partial Q_{\text{out}}}{\partial T_{\text{in}}}\Delta T_{\text{in}}\right)^2\right]^{1/2} \tag{B.3}$$

where

$$\frac{\partial Q_{\text{out}}}{\partial \dot{m}} = C_{\text{p,PAO}}(T_{\text{out}} - T_{\text{in}}) \tag{B.4}$$

$$\frac{\partial Q_{\text{out}}}{\partial C_{\text{p,PAO}}} = \dot{m}(T_{\text{out}} - T_{\text{in}}) \tag{B.5}$$

$$\frac{\partial Q_{\text{out}}}{\partial T_{\text{out}}} = \dot{m}C_{\text{p,PAO}} \tag{B.6}$$

$$\frac{\partial Q_{\text{out}}}{\partial T_{\text{in}}} = -\dot{m}C_{\text{p,PAO}} \tag{B.7}$$

The average evaporative heat transfer coefficient, $\bar{h}$, was given by

$$\bar{h} = \frac{Q_{\text{out}}}{\pi DL(\bar{T}_{\text{e}} - T_{\text{v}})} \tag{B.8}$$

The uncertainty of $\bar{h}$ was given by

$$\Delta\bar{h} = \left[\left(\frac{\partial \bar{h}}{\partial Q_{\text{out}}}\Delta Q_{\text{out}}\right)^2 + \left(\frac{\partial \bar{h}}{\partial D}\Delta D\right)^2 + \left(\frac{\partial \bar{h}}{\partial L}\Delta L\right)^2 + \left(\frac{\partial \bar{h}}{\partial \bar{T}_{\text{e}}}\Delta \bar{T}_{\text{e}}\right)^2 + \left(\frac{\partial \bar{h}}{\partial T_{\text{v}}}\Delta T_{\text{v}}\right)^2\right]^{1/2} \tag{B.9}$$

where

$$\frac{\partial \bar{h}}{\partial Q_{\text{out}}} = \frac{1}{\pi DL(\bar{T}_{\text{e}} - T_{\text{v}})} \tag{B.10}$$

$$\frac{\partial \bar{h}}{\partial D} = \frac{-Q_{out}}{\pi D^2 L(\bar{T}_{\mathrm{e}} - T_{\mathrm{v}})} \tag{B.11}$$

$$\frac{\partial \bar{h}}{\partial L} = \frac{-Q_{out}}{\pi D L^2(\bar{T}_{\mathrm{e}} - T_{\mathrm{v}})} \tag{B.12}$$

$$\frac{\partial \bar{h}}{\partial \bar{T}_{\mathrm{e}}} = \frac{-Q_{out}}{\pi D L(\bar{T}_{\mathrm{e}} - T_{\mathrm{v}})^2} \tag{B.13}$$

$$\frac{\partial \bar{h}}{\partial T_{\mathrm{v}}} = \frac{-Q_{out}}{\pi D L(\bar{T}_{\mathrm{e}} - T_{\mathrm{v}})^2} \tag{B.14}$$

The thermal resistance, *R*, was given by

$$R = \frac{\bar{T}_{\mathrm{e}} - \bar{T}_{\mathrm{cp}}}{Q_{\mathrm{out}}} \tag{B.15}$$

The uncertainty of the thermal resistance was given by

$$\Delta R = \left[\left(\frac{\partial R}{\partial Q_{\mathrm{out}}}\Delta Q_{\mathrm{out}}\right)^2 + \left(\frac{\partial R}{\partial \bar{T}_{\mathrm{e}}}\Delta \bar{T}_{\mathrm{e}}\right)^2 + \left(\frac{\partial R}{\partial \bar{T}_{\mathrm{cp}}}\Delta \bar{T}_{\mathrm{cp}}\right)^2\right]^{1/2} \tag{B.16}$$

where

$$\frac{\partial R}{\partial Q_{\mathrm{out}}} = \frac{-(\bar{T}_{\mathrm{e}} - \bar{T}_{\mathrm{cp}})}{Q_{\mathrm{out}}^2} \tag{B.17}$$

$$\frac{\partial R}{\partial \bar{T}_{\mathrm{e}}} = \frac{1}{Q_{\mathrm{out}}} \tag{B.18}$$

$$\frac{\partial R}{\partial \bar{T}_{\mathrm{cp}}} = \frac{-1}{Q_{\mathrm{out}}} \tag{B.19}$$

## APPENDIX C. CALIBRATION OF THERMOCOUPLES AND FLOW METER

### C.1. Thermocouple Calibration

The calibrations of the thermocouples used on the centrifuge table required new programming since the data acquisition system was upgraded for the centrifuge table. Control of a calibration bath and RTD were integrated with the centrifuge table's data acquisition unit. A LabVIEW program was generated to simultaneously control all three devices.

The thermocouples were calibrated using a Hart Scientific 6330 Calibration Bath and Hart Scientific 1502A NIST-Traceable platinum resistance temperature detector (RTD). The bath was capable of producing steady state temperatures from 40 to 280°C. The calibration bath used Dow Corning 200.50 silicon oil. There were several steps required before a thorough calibration of the thermocouples could be determined. First, LabVIEW software needed to be written to interface with the calibration bath, RTD, and data acquisition system. Second, the characteristics of the calibration bath and RTD needed to be determined with respect to response times and temperature fluctuations. Finally, complete calibration curves for each of the thermocouples needed to be developed.

In the loop heat pipe experimental setup, there were four grounded probe thermocouples and twelve exposed tip type E thermocouples. The grounded probe thermocouples were used in the calorimetry of the cold plate, temperature measurement for the flow meter calibration, and the ambient temperature inside the box, where the error needed to be reduced as much as possible. As a result, it was decided to only calibrate these four over the anticipated temperature range, from 20 to 145°C, in 5°C intervals. The twelve exposed tip thermocouples were mounted on the loop heat pipe in various locations. They needed to be calibrated over the full 20 to 230°C temperature range. Thus, the calibration of the thermocouples needed a second calibration bath that was capable of achieving the temperature range of 20 to 40°C. The Hart Scientific 6330 Calibration Bath was not capable of maintaining a steady temperature below 40°C for

Dow Corning 200.50 bath fluid. The bath used for this portion of the calibration was a Brinkmann Lauda RCS 20-D calibration bath using Brayco Micronic 889 (polyalphaolefin or PAO) as the bath fluid. The same RTD was used as before, and the temperature set point for the calibration bath was set manually rather than through the data acquisition interface. After some examination, it was noticed that due to the limited capability of the Brinkmann bath to heat and cool, it was difficult to maintain a fairly constant temperature in the PAO. As a result, an insulated copper tube with a closed base was placed in the bath, and the copper tube was filled with PAO. This significantly reduced the temperature fluctuation in the bath temperature.

The first step in the development of the thermocouple calibrations was to write the LabVIEW software to interface with the calibration bath, RTD, and data acquisition. Initially, sub-VI's were developed to interface directly with the calibration bath for reading the current temperature and setting the bath temperature set point as well as for reading the RTD. Wire diagrams of the RTD read, calibration bath temperature set point, and calibration bath current temperature read can be found in Figure C.1 through Figure C.3, respectively. Once these sub-VI's were developed, they needed to be incorporated into a larger framework. The front panel and wire diagram for the automatic calibration program can be seen in Figure C.4 while the front panel and wire diagram for the manual calibration program can be seen in Figure C.5.

Due to electrical noise in the centrifuge table test cell and fluctuations in the calibration bath temperature, a method was devised to determine that the calibration bath had reached a steady state. The previous 100 RTD temperature values were recorded into an array, and the standard deviation of the sampling was calculated. This number of RTD readings was selected for a 95% probability and a confidence interval of 0.95 (Montgomery, 2003). When the standard deviation dropped below the specified threshold of 0.005°C, the program would indicate that the system had reached steady state and the thermocouples were then read. The bath temperature would then be incremented or decremented as necessary. First, the full calibration process began by placing the thermocouples in the Hart Scientific calibration bath for the temperature range 40 to 230°C in 5°C increments ramping up and down with a standard deviation threshold of 0.005°C. Then, the thermocouples and RTD were cleaned and placed in the

Brinkmann bath for the temperature range 20 to 35°C. The data from each process was combined to produce one composite data set constituting the entire temperature range.

For data reduction, all 100 data points constituting one nominal temperature value were averaged and the confidence interval was calculated for the RTD. After this process, due to the increment and decrement of the calibration process, there were two data points for each nominal temperature value, as shown in Figure C.6. Plots of RTD versus each thermocouple were generated, and polynomial trend lines were fit for each thermocouple. A sample plot of TC00 is given in Figure C.7. Also, in an effort to reduce maximum deviation of the actual versus calculated RTD values, higher-order polynomial trend lines, from first to fifth order, were implemented to evaluate maximum deviation. A fifth-order polynomial was selected since it reduced the maximum deviation by approximately a factor of 4 over a first-order trend line. Results from this analysis can be seen in Table C.1 for TC00. Table C.2 shows the trend line equations for each thermocouple in tabular form.

The uncertainty associated with each thermocouple was determined by accounting for four sources of error: maximum measured uncertainty inherent to the RTD, the maximum confidence interval of the RTD temperature over the 100 readings used in the calibration, the maximum deviation of the calculated temperature from the measured temperature, and the confidence interval associated with the 100 data points in the sample of the thermocouples. The error inherent to the RTD was ±0.009°C. The maximum confidence interval of the RTD from the 100 readings was ±0.0055°C over the entire temperature range. The maximum deviations of the calculated temperature and the measured temperature are thermocouple specific, and can be seen in Table C.3 along with the total error of each thermocouple.

### C.1.1. Calibration Procedure

1. Mount all of the thermocouples to the RTD probe with the thermocouple and RTD tips as close to each other as possible.
2. Place the thermocouple and RTD bundle vertically into the Hart Scientific 6330 Calibration Bath, with the probes not touching any of the bath surfaces.
3. Turn on the RTD and calibration bath, setting the bath to 40°C.
4. Turn on the centrifuge table power.

5. In the control room, turn on LabVIEW and open the thermocouple calibration program.
6. Set the lower temperature set point to 40°C and the upper temperature set point to 230°C, with a temperature increment of 5°C.
7. Set the standard deviation threshold to 0.005°C.
8. Run the VI.
9. Current temperatures can be examined while the calibration is in progress on the main screen.
10. After this calibration cycle has been completed, remove and clean the thermocouples and RTD, rebundle, and place in the copper tube that is located in the Brinkmann Lauda RCS 20-D calibration bath.
11. Turn the bath on and set to 20°C.
12. Open the manual thermocouple calibration VI.
13. Ensure the "Keep Running" button is depressed, then run the program.
14. Wait for the RTD standard deviation to reach below 0.005, the press the 'Proceed to TC Read' button.
15. Increment the bath temperature by 5°C up to 35°C and back down to 20°C, recording temperature values at each location an overall two times.
16. Take the two data files and combine to make one composite data file.

## C.2. Flow Meter Calibration

The calibration of the turbine flow meter for the high-temperature fluid loop proved to be a difficult challenge. Due to the chemistry of PAO, there is a significant difference in density and viscosity with respect to temperature. As a result, a calibration surface that was dependent on flow meter output voltage and temperature was required to determine the actual mass flow rate. An uncertainty analysis was also performed to fully characterize the flow meter.

A calibration setup was developed using a Lauda RCS-20D calibration bath filled with PAO, Tuthill pump from the high-temperature fluid loop, SS-56S6 Whitey inline filter with a 140 micron filter, calibrated type-E thermocouple that was used for measuring temperature entering the flow meter in the high temperature fluid loop, and an Omega FTB-9506 turbine flow meter with FLSC-61 signal conditioner. A LabVIEW

code was developed to aid in the calibration of the flow meter (Figure C.8). This code served as the stopwatch and data recording for the calibration. Temperature and flow meter voltage were recorded, with raw data files generated. The pump was controlled via a 0-10V input signal to a TECO FM50 motor controller. The flow meter required an input voltage between 12-28VDC and output voltage between 0-10V. All data was collected through the centrifuge table slip rings to the data acquisition to capture all error inherent to the centrifuge table test bed. A calibrated Mettler PC4400 scale was used to determine the mass collected during a given test run. Flow straightening sections upstream and downstream were placed according to the manufacturer's instructions. A three-way valve was installed after the flow meter, which allowed the entire flow system to reach a steady temperature. A schematic of the setup is shown in Figure C.9. Once the temperature was steady, the flow was diverted to a catch basin for a specified amount of time. The voltage from the flow meter and the temperature from the thermocouple were recorded during this time, and when the basin was full, the flow was again diverted to recirculating the PAO back to the chiller. During each measurement, as many data points as possible were collected across the time span with the limiting factor being the iteration time on the LabVIEW software. The minimum number of data points collected for any given run was 437. The voltages and temperatures were averaged and a confidence interval of 0.95 was calculated based on a statistical t-distribution for each test run. The test was repeated for a total of five averaged data points for each nominal temperature and flow rate. These tests were completed over the range of $T$ = 20 to 120°C in intervals of 25°C and flow rates ranging from $\dot{m}$ = 0.0064 to 0.025 kg/s in intervals of approximately 0.002 kg/s. A 3-D paraboloid regression equation was generated using SigmaPlot to relate temperature, flow meter voltage, and mass flow rate (Figure C.10). The equation can be seen in Table C.4.

During the course of developing the calibration setup and testing, several issues were encountered. Immediately from the start of working out the bugs in the system, it was noticed that the flow meter would not output a voltage linearly as expected, but rather responded in a quadratic fashion with a local maximum at approximately six volts. It was discovered that the motor housing of the pump was not properly grounded, causing electromagnetic interference to disrupt the operation of the flow meter. The output

voltage was extremely inconsistent, changing +/- 0.5 volts at apparently random times. Initially an SS-56S6 Whitey inline filter with a 140 micron filter was placed in the flow loop to catch any debris that may have been picked up by the pump. It was then noticed that on the flow loop outlet, air bubbles were being rejected. All of the fittings were retightened and the flow remained steady. At apparently random times the flow meter would start outputting random voltage readings. It was discovered that screw terminal was not tightened down on the wire connector, occasionally creating an open circuit loop. During the course of data collection, the output voltage would develop a trend, as seen in Figure C.11. When this was observed during data reduction, another data point would be collected to replace it. This was likely due to fluctuations in the flow rate and was observed more prevalently at higher flow rates.

With this type of calibration, it is critical to have a firm grasp on the uncertainty associated with the mass flow rate. Three types of uncertainty were identified associated with this calibration: error associated with the scale and time, error due to the voltage confidence interval and thermocouple error and confidence interval, and deviation of the fit equation from actual data. Each of these errors are described below.

The total error associated with this uncertainty analysis is given by

$$\Delta\dot{m}_{\text{tot}} = \Delta\dot{m}_{\text{m/t}} + \Delta\dot{m}_{\text{V/T}} + \Delta\dot{m}_{\text{dev}} \tag{C.1}$$

The error for $\Delta\dot{m}_{\text{m/t}}$ was determined by

$$\dot{m} = \frac{m}{t} \tag{C.2}$$

which yields the uncertainty

$$\Delta\dot{m}_{\text{m/t}} = \left[\left(\frac{\partial\dot{m}_{\text{m/t}}}{\partial m}\Delta m\right)^2 + \left(\frac{\partial\dot{m}_{\text{m/t}}}{\partial t}\Delta t\right)^2\right]^{1/2} \tag{C.3}$$

where

$$\frac{\partial\dot{m}_{\text{m/t}}}{\partial m} = \frac{1}{t} \tag{C.4}$$

and

$$\frac{\partial \dot{m}_{\mathrm{m/t}}}{\partial t} = -\frac{m}{t^2} \tag{C.5}$$

The error for $\Delta \dot{m}_{\mathrm{V/T}}$ was determined by performing an error analysis on the fit equation developed using SigmaPlot

$$\dot{m} = y_o + aT + bV + cT^2 + dV^2 \tag{C.6}$$

which yields the uncertainty

$$\Delta \dot{m}_{\mathrm{V/T}} = \left[ \left( \frac{\partial \dot{m}_{\mathrm{V/T}}}{\partial T} \Delta T \right)^2 + \left( \frac{\partial \dot{m}_{\mathrm{V/T}}}{\partial V} \Delta V \right)^2 \right]^{1/2} \tag{C.7}$$

where

$$\frac{\partial \dot{m}_{\mathrm{V/T}}}{\partial T} = a + 2cT \tag{C.8}$$

and

$$\frac{\partial \dot{m}_{\mathrm{V/T}}}{\partial V} = b + 2dV \tag{C.9}$$

The error associated with the deviation of the fit equation from the actual data is given by

$$\Delta \dot{m}_{\mathrm{dev}} = \left| \dot{m}_{\mathrm{a}} - \dot{m}_{\mathrm{p}} \right| \tag{C.10}$$

Applying this uncertainty analysis to the data set, a maximum error of 4.0% was calculated and imposed over the entire calibration range.

### C.2.1. Calibration Procedure

1. Connect monitor, keyboard, and mouse to extensions in Test Cell 4.
2. Activate LabVIEW code entitled “Flow meter Calibration.”
3. Ensure three-way valve is in by-pass mode (flow diverting back to tank).
4. Turn on Lauda calibration bath and set to 20°C. Turn on the motor control unit.
5. Using the LabVIEW program, increase the motor control input voltage to the desired setting (1.0).
6. Allow the flow meter to come to temperature using PAO from the calibration bath that is by-passed back to the bath.

7. Take the empty 2 L flask and place on the scale. Tare the scale. Remove the flask from the scale and place under the three-way valve.
8. When ready, quickly move the three-way valve into measurement mode while simultaneously depressing the “Timer” button on the LabVIEW front panel.
9. Allow the flask to fill for 45 seconds for pump voltage settings one to five, and for 30 seconds for pump voltages settings six to ten.
10. Quickly return the three-way valve to by-pass mode while simultaneously depressing the “Timer” button on the LabVIEW front panel.
11. User will be prompted to enter the mass collected. Carefully place the filled flask on the scale and record the mass in the program. Return the collected PAO to the calibration bath.
12. Repeat steps 6 through 12, increasing the motor control input voltage by increments of 1.0V up to 10.0V for a given temperature, then increasing the temperature by 25°C up to 120°C.

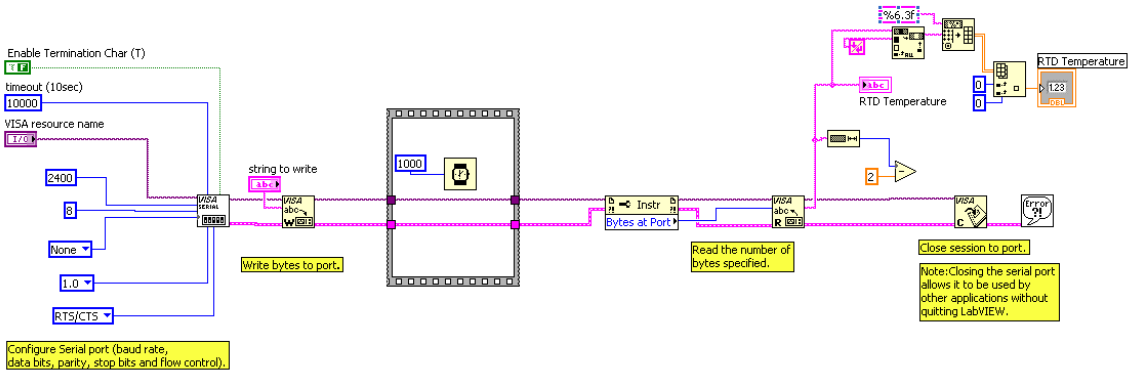


Figure C.1. LabVIEW sub-VI wire diagram for RTD read.

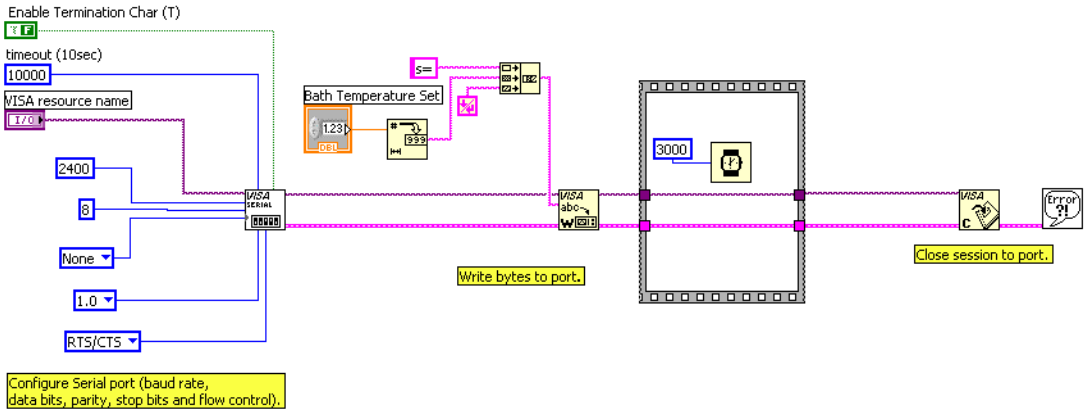


Figure C.2. LabVIEW sub-VI wire diagram for calibration bath temperature set.

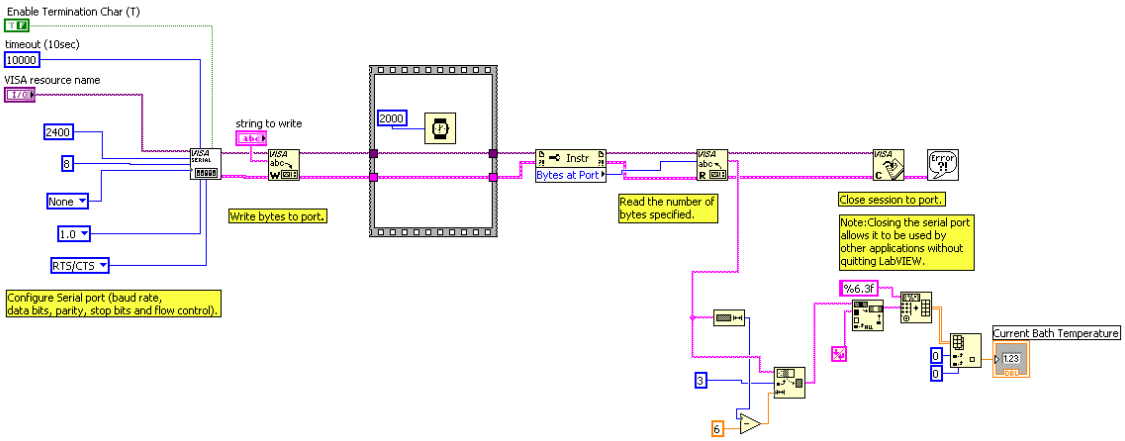


Figure C.3. LabVIEW sub-VI wire diagram for calibration bath temperature read.

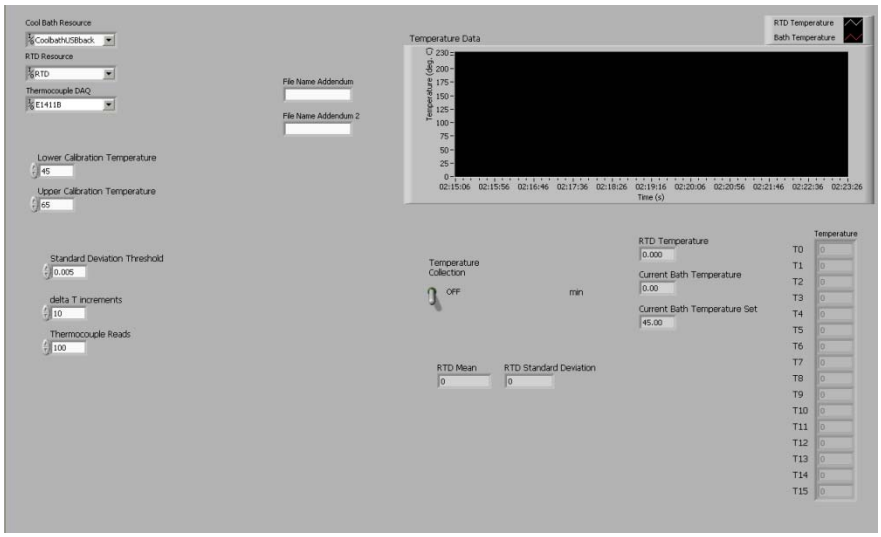


(a)

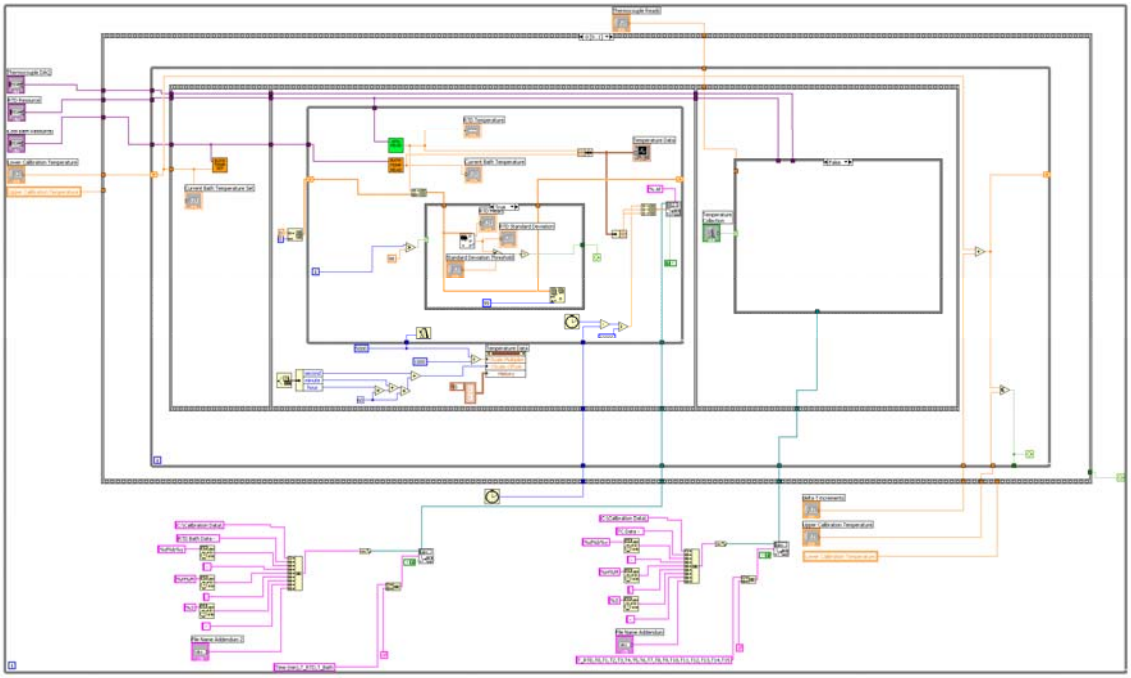

(b)

Figure C.4. LabVIEW VI for controlling the automatic thermocouple calibration: (a) Front panel; (b) Wire diagram

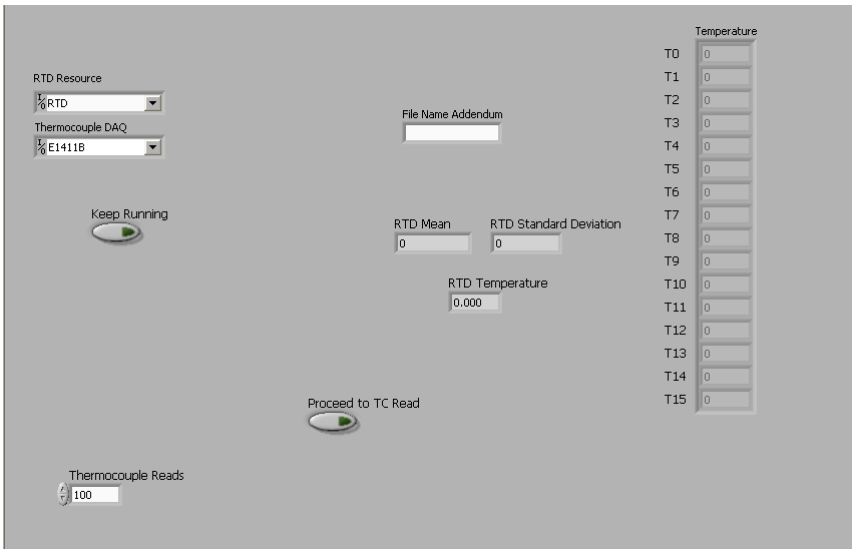


(a)

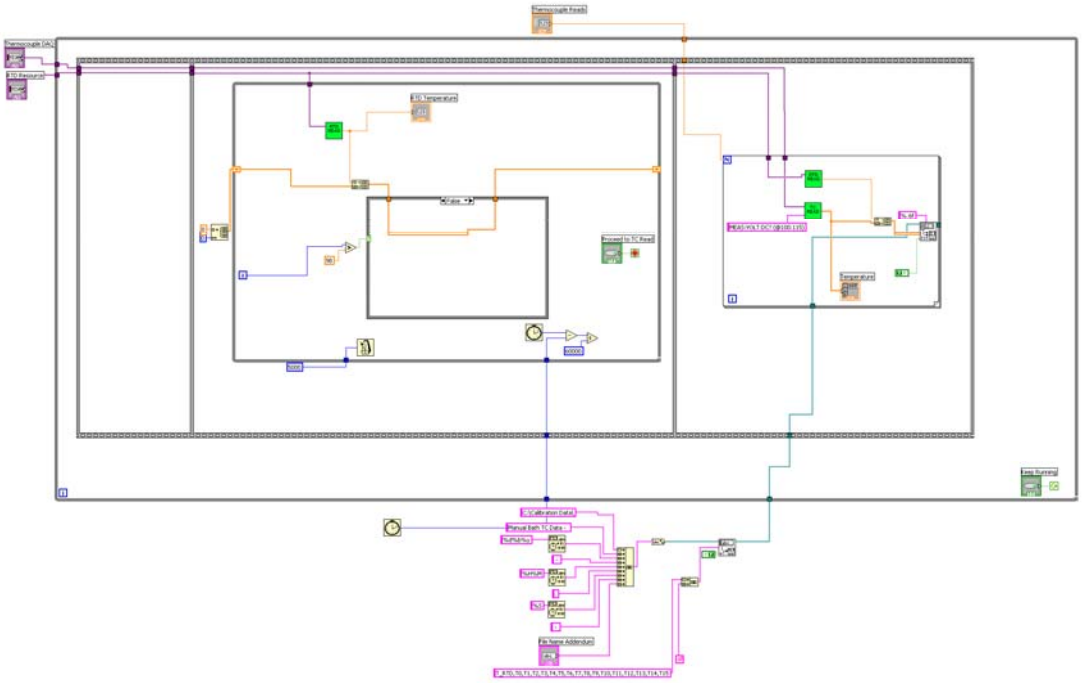

(b)

Figure C.5. LabVIEW VI for manual thermocouple calibration: (a) Front panel; (b) Wire diagram.

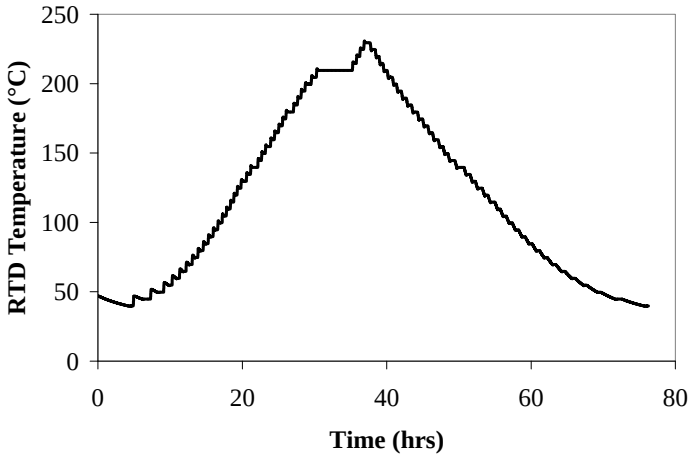


Figure C.6. RTD temperature vs. time from the thermocouple calibration procedure.

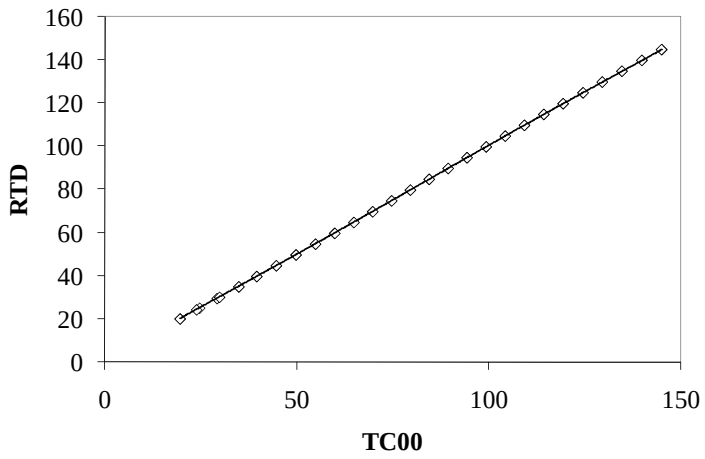


Figure C.7. Sample RTD vs. thermocouple plot for TC00.

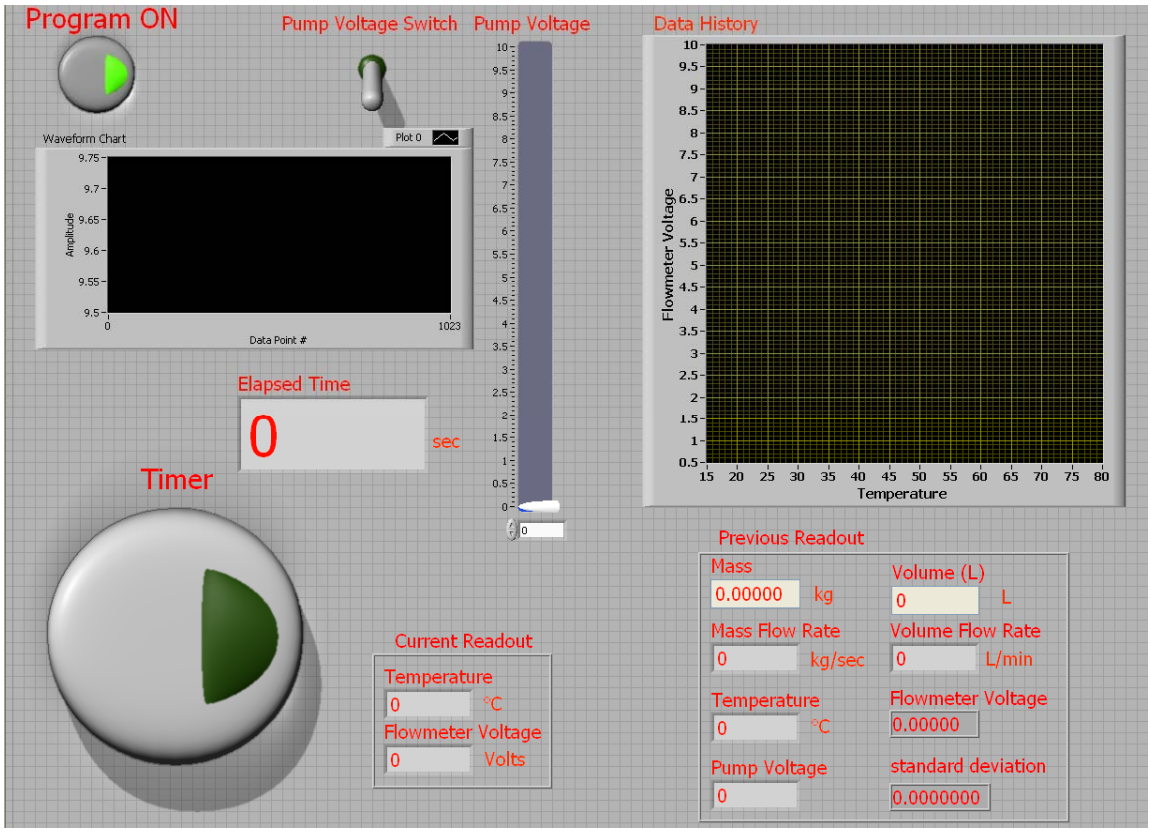


(a)

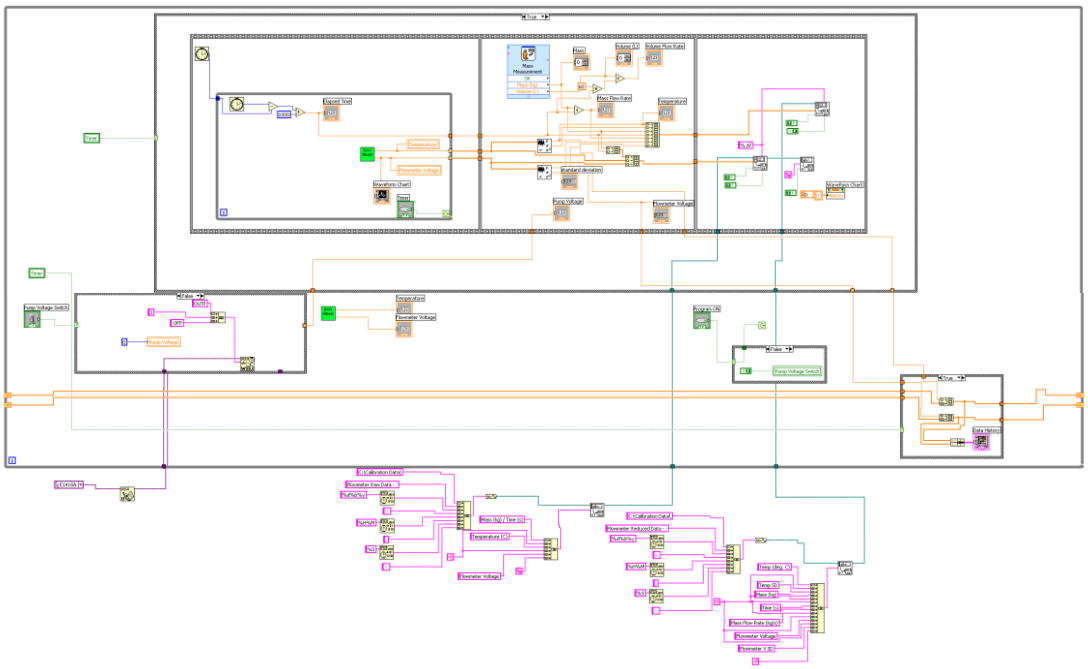

(b)

Figure C.8. LabVIEW VI for flow meter calibration program: (a) Front panel; (b) Wire diagram.

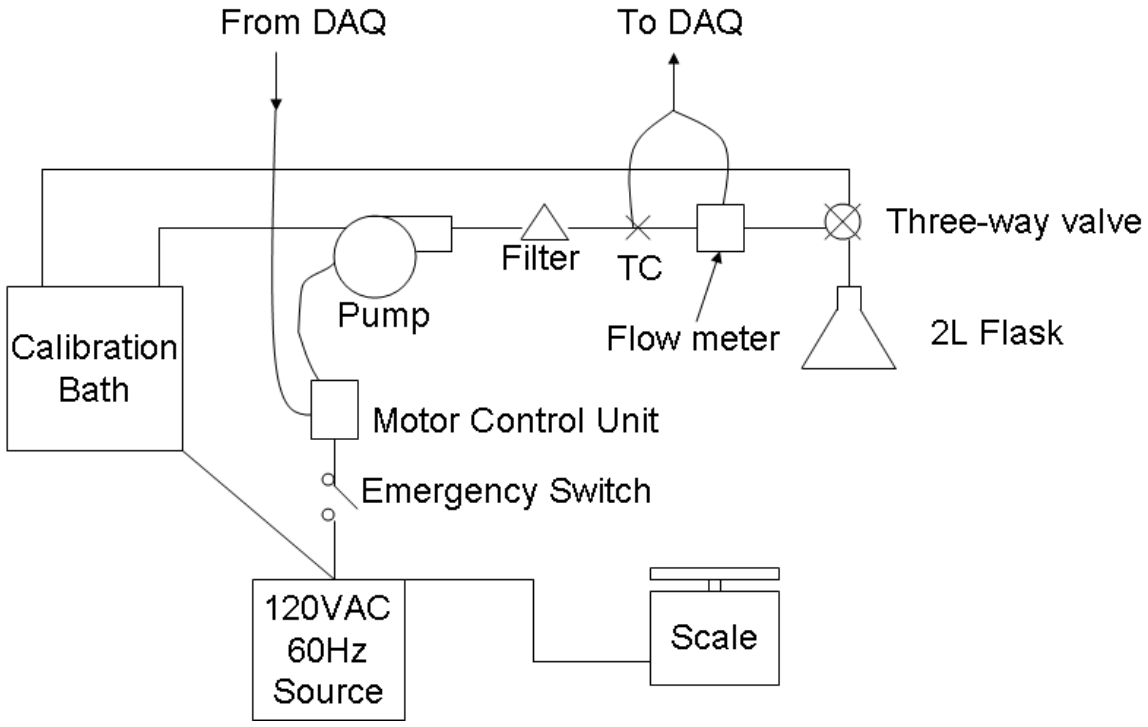

Figure C.9. Schematic of flow meter calibration loop

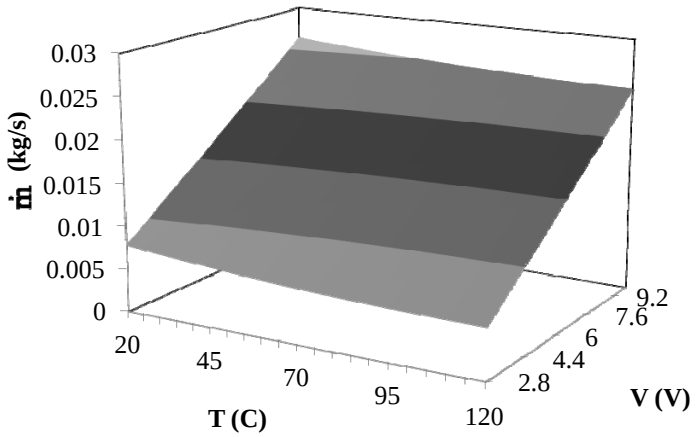


Figure C.10. Temperature and flow meter voltage versus mass flow rate calibration curve for the high-temperature fluid loop flow meter.

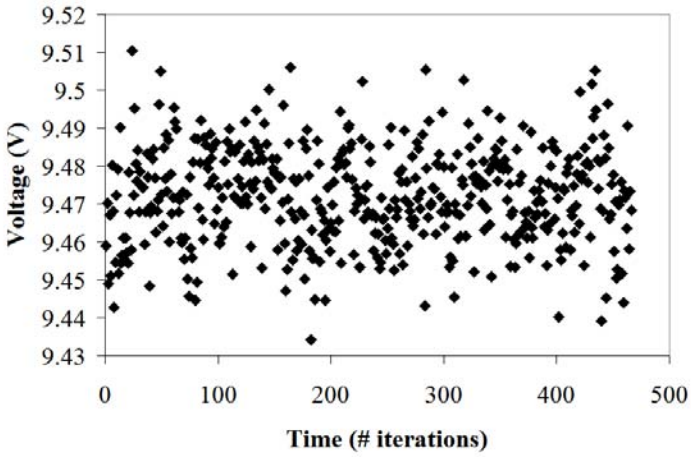


(a)

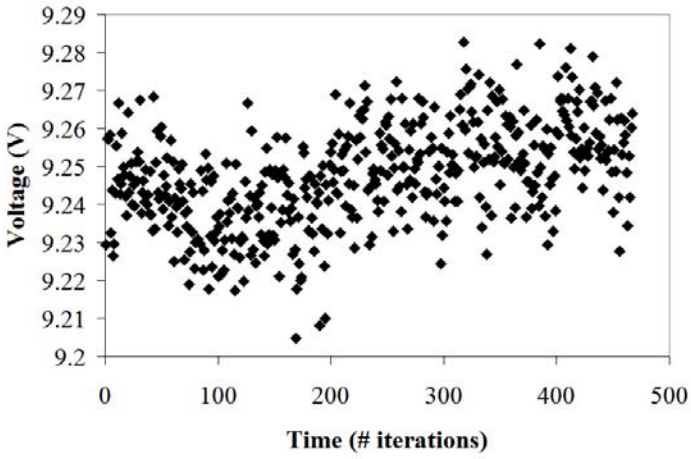


(b)

Figure C.11. Sample data collected during one time run for the flow meter calibration. (a) "Shotgun Blast" good data set; (b) "Trend" bad data set.

Table C.1. Maximum deviation of calculated RTD and experimental RTD corresponding to each order of polynomial for thermocouple TC00.

| Polynomial Order | First | Second | Third | Fourth | Fifth |
|---|---|---|---|---|---|
| Maximum Deviation (°C) | 0.48 | 0.45 | 0.16 | 0.15 | 0.11 |

Table C.2. Coefficients for the trend line of each thermocouple.

$$T_{actual} = a_0 + a_1 T_{TC} + a_2 T_{TC}^{\ 2} + a_3 T_{TC}^{\ 3} + a_4 T_{TC}^{\ 4} + a_5 T_{TC}^{\ 5}$$

| Thermocouple | $a_0$ | $a_1$ | $a_2$ | $a_3$ | $a_4$ | $a_5$ |
|---|---|---|---|---|---|---|
| TC00 (CP In) | 4.57060445428729E-01 | 1.05652835054604E+00 | -3.38190520875348E-03 | 6.02302203912097E-05 | -4.22250860114073E-07 | 1.01719370757371E-09 |
| TC01 (CP Out) | -6.71731670248675E-02 | 1.09162481723344E+00 | -4.45690722980988E-03 | 7.45596958297964E-05 | -5.12753870618840E-07 | 1.23532227941934E-09 |
| TC02 (Box Ambient) | 1.67608851857495E-01 | 1.08395588495732E+00 | -4.18132574798607E-03 | 7.07111104393385E-05 | -4.88344399395756E-07 | 1.17841766477268E-09 |
| TC03 (Flow Meter In) | 3.41571348824236E-02 | 1.11271583430979E+00 | -5.02404183034797E-03 | 8.08082585107749E-05 | -5.43858633628823E-07 | 1.29518294797893E-09 |
| TC04 (Evap 1) | 3.88538977221388E+00 | 7.96300850243819E-01 | 4.24547606721552E-03 | -3.88677461307058E-05 | 1.58255416015721E-07 | -2.34382548031174E-10 |
| TC05 (Evap 2) | 3.84666399157782E+00 | 7.79389295912649E-01 | 4.58781158427047E-03 | -4.19147483368683E-05 | 1.70607369149700E-07 | -2.53272155262545E-10 |
| TC06 (Evap 3) | 3.43144596520976E+00 | 7.80135796631358E-01 | 4.59329657844732E-03 | -4.20519229310971E-05 | 1.71478424670112E-07 | -2.54933199706354E-10 |
| TC07 (Evap 4) | 3.13979027632699E+00 | 7.90836909105568E-01 | 4.28556652723263E-03 | -3.87573183171731E-05 | 1.56271525700294E-07 | -2.29581121061401E-10 |
| TC08 (Evap Out) | 3.69915288517716E+00 | 7.82179382148322E-01 | 4.57928286232713E-03 | -4.21678343228003E-05 | 1.72786905067963E-07 | -2.58026057043238E-10 |
| TC09 (Cond In) | 3.49099219277048E+00 | 7.70780118608180E-01 | 4.85109600118292E-03 | -4.46693742753094E-05 | 1.82732284362794E-07 | -2.72411097504291E-10 |
| TC10 (Cond 1) | 3.58974962539873E+00 | 7.83472149016743E-01 | 4.59630318025552E-03 | -4.25067859755088E-05 | 1.74438732820078E-07 | -2.60500167972660E-10 |
| TC11 (Cond 2) | 3.48473325833062E+00 | 7.81222079068205E-01 | 4.52702317872843E-03 | -4.12552062722017E-05 | 1.67487608290567E-07 | -2.47827033736023E-10 |
| TC12 (Cond 3) | 3.52121560485026E+00 | 7.65772989719964E-01 | 4.98601477917870E-03 | -4.60604857830875E-05 | 1.88981194007878E-07 | -2.82525305173107E-10 |
| TC13 (Cond Out) | 3.37758528400691E+00 | 7.75690833725901E-01 | 4.63174346039307E-03 | -4.19508133665537E-05 | 1.69069414365516E-07 | -2.48342058180827E-10 |
| TC14 (Bayonet In) | 3.60233647710038E+00 | 7.75843052066857E-01 | 4.64688850212116E-03 | -4.24299704012793E-05 | 1.72539813453339E-07 | -2.55840771155446E-10 |
| TC15 (CC/Evap) | 3.48346921511447E+00 | 7.74284360401172E-01 | 4.66498637738964E-03 | -4.24414330959761E-05 | 1.72087402595724E-07 | -2.54508869559325E-10 |

Table C.3. Maximum deviation and total error for each thermocouple.

| Thermocouple | Maximum Deviation | ±Total Error |
|---|---|---|
| TC00 (CP In) | 0.106414 | 0.122388 |
| TC01 (CP Out) | 0.098267 | 0.111181 |
| TC02 (Box Ambient) | 0.097236 | 0.111085 |
| TC03 (Flow Meter In) | 0.098736 | 0.111083 |
| TC04 (Evap 1) | 0.295217 | 0.307238 |
| TC05 (Evap 2) | 0.280751 | 0.293427 |
| TC06 (Evap 3) | 0.280739 | 0.292962 |
| TC07 (Evap 4) | 0.322196 | 0.334702 |
| TC08 (Evap Out) | 0.315632 | 0.328080 |
| TC09 (Cond In) | 0.274506 | 0.288721 |
| TC10 (Cond 1) | 0.278507 | 0.291299 |
| TC11 (Cond 2) | 0.278103 | 0.290722 |
| TC12 (Cond 3) | 0.256994 | 0.269226 |
| TC13 (Cond Out) | 0.291867 | 0.304493 |
| TC14 (Bayonet In) | 0.285927 | 0.298477 |
| TC15 (CC/Evap) | 0.285186 | 0.297719 |

Table C.4. 3-D paraboloid regression equation for high-temperature fluid loop flow meter.

$$\dot{m} = y_0 + aT + bV + cT^2 + dV^2$$

| | |
|---|---|
| $y_0$ | 2.07704738E-03 |
| a | -4.69012732E-05 |
| b | 2.35000226E-03 |
| c | 1.91650117E-07 |
| d | 1.49811559E-05 |

## APPENDIX D. LOOP HEAT PIPE MOUNTING

The loop heat pipe was mounted onto the centrifuge table such that the centerline of the tubing coincided with the outer table radius as much as possible. A small deviation existed since the condenser section and the evaporator/compensation chamber were both straight. This induced a non-uniform radial acceleration field over the lengths of these sections that needed to be quantified. As shown in Figure D.1, the straight condenser section, with length $L_c$, was geometrically aligned on the table so that the centerline was as close to the table radius, $R_{ct}$, as much as possible over its length. The radius of the condenser midpoint, $R_{cm}$, was found as shown in Figure D.1 as well. The condenser endpoints were first set to coincide with the centrifuge table radius. The half-angle is given by

$$\theta = \sin^{-1}\left(\frac{L_c}{2R_{ct}}\right) \tag{D.1}$$

The length from the center of the centrifuge table to the midpoint of the condenser is

$$L_{cm} = R_{ct}\cos\theta \tag{D.2}$$

One-half of the change in radius from this point to the centrifuge table radius is used to determine the radius of the midway point of the condenser section.

$$R_{cm} = L_i + \frac{1}{2}(R_{ct} - L_{cm}) \tag{D.3}$$

The evaporator section and the compensation chamber were also straight and the method to locate these components in relation to the outer table radius is similar to that described above for the condenser section. However, the evaporator section is directly attached to the compensation chamber and the length of the evaporator is different than that of the compensation chamber. Therefore, further care was taken in determining the maximum deviation of the centerline radius of these two components from the radius of the centrifuge table.

Stands were designed using G-7 phenolic to mount the loop heat pipe vertically with support at the compensation chamber, evaporator, condenser, and two on the transport lines (Figure D.2). The tops of these stands were anchored to the table to reduce deflection when the table was rotating. A survey was taken at 22 locations on the loop heat pipe to determine how far various portions of the loop heat pipe were from the centerline radius and at what distance that location was from the origin at point 1 (Figure 2.6(d)). The loop heat pipe had a minimum radius of 119.2 cm at locations 5 and 6 and maximum radius of 123.3 cm at location 15 at the outside edge of the tubing at each location. The entire loop heat pipe fitted within 4.6 cm for a percent radial difference of 3.7%. Complete survey data can be seen in Table D.1.

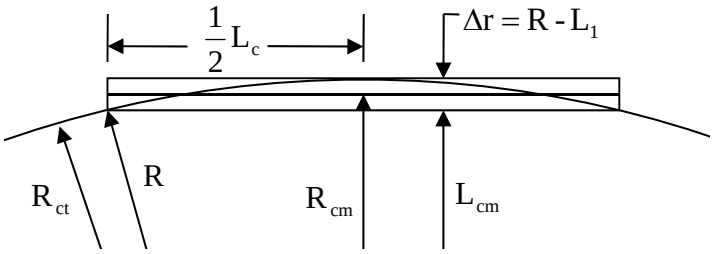

Figure D.1. Mounting of LHP to minimize acceleration gradient.

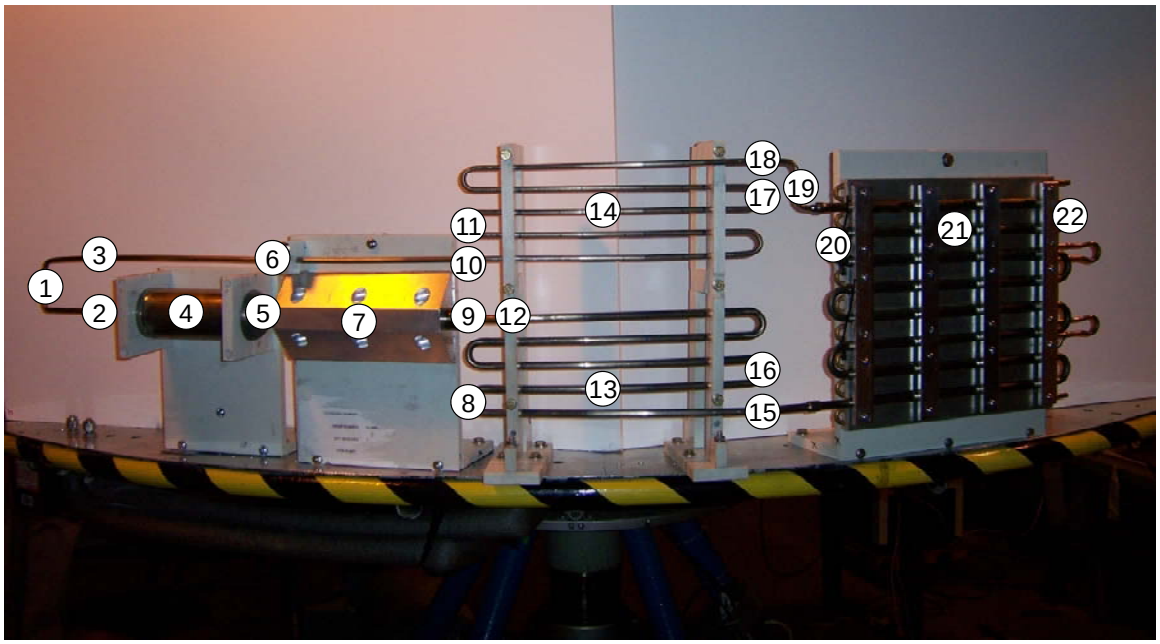

Figure D.2. LHP survey locations.

Table D.1. Loop heat pipe mounting survey data.

| Survey Location | s (cm) | r (cm) (tube centerline) |
|---|---|---|
| 1 | 0.0 | 123.0 |
| 2 | 15.9 | 122.9 |
| 3 | 26.0 | 122.2 |
| 4 | 35.9 | 121.5 |
| 5 | 35.9 | 120.5 |
| 6 | 35.9 | 120.5 |
| 7 | 47.6 | 120.5 |
| 8 | 59.7 | 121.1 |
| 9 | 59.7 | 122.1 |
| 10 | 59.7 | 120.8 |
| 11 | 59.7 | 121.1 |
| 12 | 64.1 | 123.0 |
| 13 | 76.5 | 121.1 |
| 14 | 76.5 | 121.1 |
| 15 | 92.4 | 123.4 |
| 16 | 93.3 | 121.1 |
| 17 | 93.3 | 121.1 |
| 18 | 93.3 | 122.7 |
| 19 | 97.2 | 122.7 |
| 20 | 101.6 | 122.1 |
| 21 | 119.1 | 121.1 |
| 22 | 136.8 | 122.1 |

## APPENDIX E. BRAYCO MICRONIC 889 TECHNICAL DATA

Technical data for various properties against temperature for Brayco Micronic 889, including density, specific heat at constant pressure, thermal conductivity, and kinematic viscosity were provided by Ghajar et al (1994). Brayco Micronic 889 technical data from Castrol was compiled and the data was curve-fitted using a least squares approach and varying order polynomials. The equations are only valid on the temperature range -54 ≤ T ≤ 135°C. The authors report that for $\rho$, $C_p$, and $k$ a maximum deviation of less than ±0.5% from the reported data for the property equations. For $\nu$, they reported a maximum deviation of +3.4%. The equations for these properties are given as

$$\rho = 1.36 \cdot 10^3 - 4.56T + 0.0157T^2 - 0.280 \cdot 10^{-4}T^3 + 0.174 \cdot 10^{-7}T^4 \quad \text{(E.1)}$$

$$k = 0.154 - 5.88 \cdot 10^{-5}T \quad \text{(E.2)}$$

$$C_p = 1.022 + 3.77 \cdot 10^{-3}T \quad \text{(E.3)}$$

For all of these equations, $T$ is in Kelvin, $\rho$ is in kg/m$^3$, $C_p$ is in kJ/kg-K, and $k$ is in W/m-K.

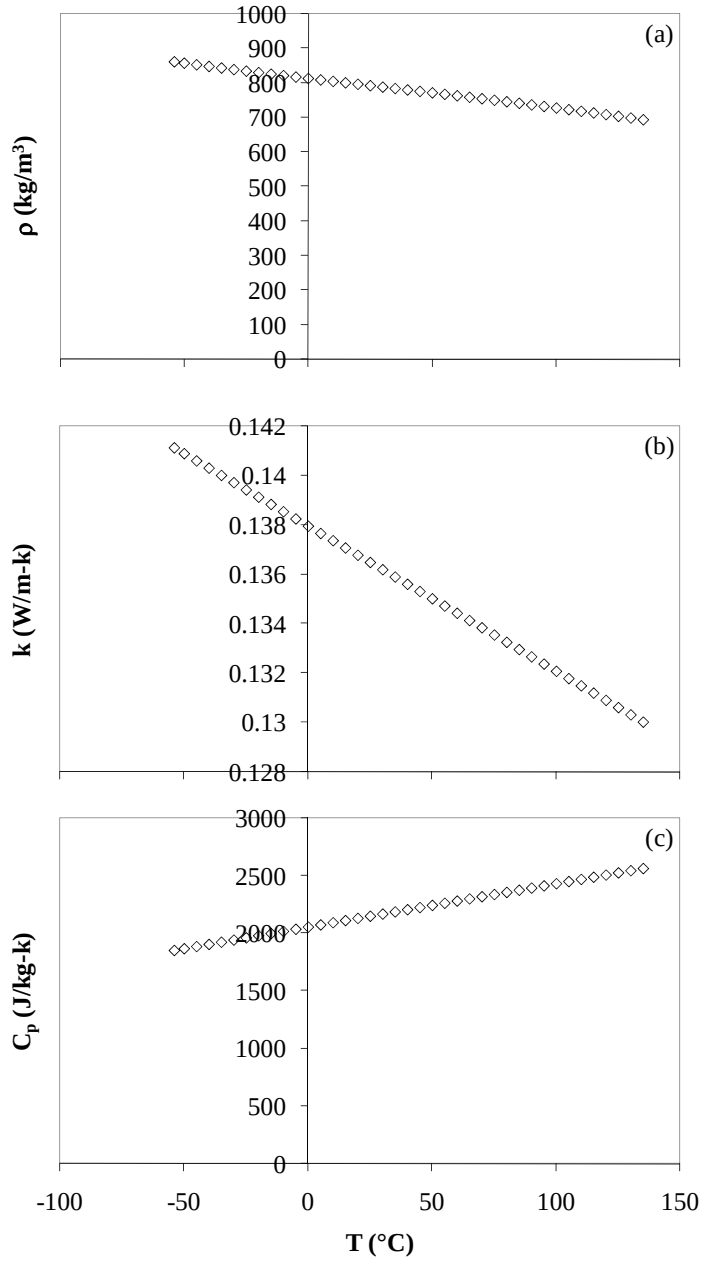


(c)

Figure E.1. Brayco Micronic 889 properties vs. temperature. (a) $\rho$ vs. $T$; (b) $k$ vs. $T$; (c) $C_p$ vs. $T$.

## APPENDIX F. CENTRIFUGE TABLE UPGRADES

The previous centrifuge table data acquisition system dated back to the early 1990's. The original computer was a Pentium 386 running ViewDAC for data collection and reduction. At the start of this project, it was determined that the data acquisition system needed to be upgraded, including the data acquisition unit and computer system. Since all of this equipment was going to be upgraded, it was decided to completely evaluate the existing data acquisition wiring and document this information.

The first step to updating the data acquisition system was to record the original data acquisition wiring. All of the wiring on the centrifuge table was rewired and documented so that it would be easier to trace wiring back to the centrifuge table control room. The wiring scheme on the centrifuge table can be seen in Figure F.1. The terminal strip at the bottom of this photo is located on the rotating table, while the terminal strips at the top are on the stationary support. These are connected via a 40-ring slip ring. A new wiring panel was developed for the wiring coming from the stationary terminal strips above the centrifuge table back to the control room, as shown in Figure F.2. Wiring on the centrifuge table terminal strip now matches the wiring coming into the centrifuge table control room. This information was completely documented for future reference. Each circuit from the centrifuge table to the slip ring wiring panel in the control room was checked for continuity by hand.

After verifying the wiring configuration was in proper operating condition, documentation for the new data acquisition hardware was reviewed so that the upgrades could be started. Initially, a new wiring panel was developed for the new data acquisition interface as shown in Figure F.3. This panel was designed to accommodate 64 channels (three wires per channel) for data acquisition, as well as 16 channels (four wires per channel) for voltage and current control. Each circuit from the data acquisition interface panel to the two new data acquisition modules was checked for continuity by hand. Jumper cables were created to transfer signals coming in from the slip rings to the data acquisition wiring panel.

The new data acquisition system from Agilent Technologies has a mainframe (E8408A) with four slots into which the following cards were installed: a command module (E1406A), an 8/16 channel D/A converter (E1418A), a 5½-digit multimeter (E1411B), and a sixty-four channel, 3-wire multiplexer (E1476A). The command module serves as the main source of communication between all of the cards in the mainframe. The command module also exchanges data and commands between the computer and data acquisition system. The D/A converter is a control type module, allowing the user to request a certain output voltage or current from up to sixteen channels. The multimeter reads the voltages that the multiplexer collects from thermocouples, pressure transducers, accelerometers, etc., as well as any externally applied voltages, currents, and resistances. Communication between the data acquisition system and the computer takes place via the general purpose interface bus (GPIB) or IEEE-488 protocol. Essentially, text commands are sent from the computer to the data acquisition system. Then, if the command requests a control signal, the proper output is processed. If the command were for data acquisition, then ASCII data is returned to the user for processing.

With the new data acquisition system and computer assembled, documentation for the data acquisition system needed to be reviewed to determine the proper commands necessary to use the computer to communicate with the data acquisition system. Initially, single text lines were sent from the computer using Agilent's VISA Assistant software. Commands were sent to read thermocouple temperatures on one of the channels of the multiplexer.

The software used for writing the data acquisition code was LabVIEW, a visual computer language. Virtual instruments (VIs) for communicating with the data acquisition system started fairly crudely. Virtual instruments are subprograms that are written with certain inputs and calculated outputs, which can greatly simplify a complicated code. First, the task of reading several voltage channels and outputting the data to the screen was accomplished. Second, the reading of several voltage channels was placed inside a timed loop such that data would be recorded at regular intervals and written to a file that Microsoft Excel could read. Next, the proper conversions for voltage

to temperature, acceleration, and pressure were written into the code so that actual data was recorded to a file.

The next task to be accomplished with this software was control communication. What was desired was a system where a certain voltage could be applied to increase the angular velocity of the centrifuge table, and to control a variety of other devices, such as pumps, heaters, etc. Following a similar process to the development of the data acquisition software, a virtual instrument was written that could control the output voltage of several channels along with the capability of turning them on and off at any time. This VI was then merged with the data acquisition program with appropriate Boolean commands for control. This VI was tested and verified when data was collected for a liquid-vapor separator experiment on the centrifuge table. A program was tailored for this experiment, including the appropriate flow meter, pressure transducer, accelerometer conversions, and data recording.

After control of the centrifuge table was accomplished using a voltage from the D/A converter to control the angular velocity, it was decided to control the acceleration directly. A relation was then developed between voltage and acceleration. Centrifugal acceleration is given by

$$a_{\mathrm{r}}^{+} = \frac{r\omega^2}{g} \tag{F.1}$$

Voltage is related to angular velocity by

$$V = B\omega \tag{F.2}$$

where $B$ is an experimental constant to be determined. Substituting this relation into the expression for centrifugal acceleration yields

$$a_{\mathrm{r}}^{+} = \frac{r}{g}\left(\frac{V}{B}\right)^2 \tag{F.3}$$

Solving equation (F.3) for voltage yields the relation used for deriving a corresponding voltage for a chosen centrifugal acceleration.

$$V = B\sqrt{\frac{a_{\mathrm{r}}^{+} g}{r}} \tag{F.4}$$

Thus, voltage is linearly related to the square root of centrifugal acceleration. This relation can be extended to relate voltage and the acceleration magnitude. The magnitude of acceleration is given by

$$a^{+} = \sqrt{a_{\theta}^{+^2} + a_{\mathrm{r}}^{+^2} + a_{\mathrm{z}}^{+^2}} \tag{F.5}$$

where $a_{\theta}^{+}$, $a_{\mathrm{r}}^{+}$, and $a_{\mathrm{z}}^{+}$ are the accelerations normalized by gravity in the azimuthal, radial, and axial directions on the centrifuge table. Solving for the radial acceleration gives

$$a_{\mathrm{r}}^{+^2} = a^{+^2} - a_{\theta}^{+^2} - a_{\mathrm{z}}^{+^2} \tag{F.6}$$

When the centrifuge table is rotating with a constant velocity, $a_{\theta}^{+} = 0$ and $a_{z}^{+} = -1$. After substituting these values in for equation (F.6) and solving for the square root of centrifugal acceleration

$$\sqrt{a_{\mathrm{r}}^{+^2}} = \left(a^{+^2} - 1\right)^{1/4} \tag{F.7}$$

Substituting equation (F.7) into (F.4) yields the relation between table voltage and the magnitude of the acceleration.

$$V_{\mathrm{ct}} = B\sqrt{\frac{g}{r}}\left(a^{+^2} - 1\right)^{1/4} \tag{F.8}$$

To calculate *B*, experimental data relating table voltage with centrifugal acceleration was collected. Then, a plot of voltage versus the square root of centrifugal acceleration was generated and a linear best fit regression was derived with the voltage intercept forced through the origin. The corresponding slope is then $B\sqrt{g/r}$. A sample plot can be seen in Figure F.4. After the slope for this equation was found, an acceleration control slide bar was added to the data acquisition program by deriving a corresponding voltage output. It is important to note that the slope is experiment specific, and if the location of the accelerometer is changed, a new slope needs to be found.

It was desired to have the capability of reading higher temperatures on the centrifuge table. The current thermocouple amplifier on the centrifuge table is for Type T thermocouples, which have an operating temperature range between -250 to 350°C. A

new Type E thermocouple amplifier (Omega OM7-47-E-07-2-C) has been installed on the underside of the centrifuge table opposite of the existing thermocouple amplifier so that either one can be used, depending on the experimental requirements specified, providing operating temperatures between -200 to 900°C.

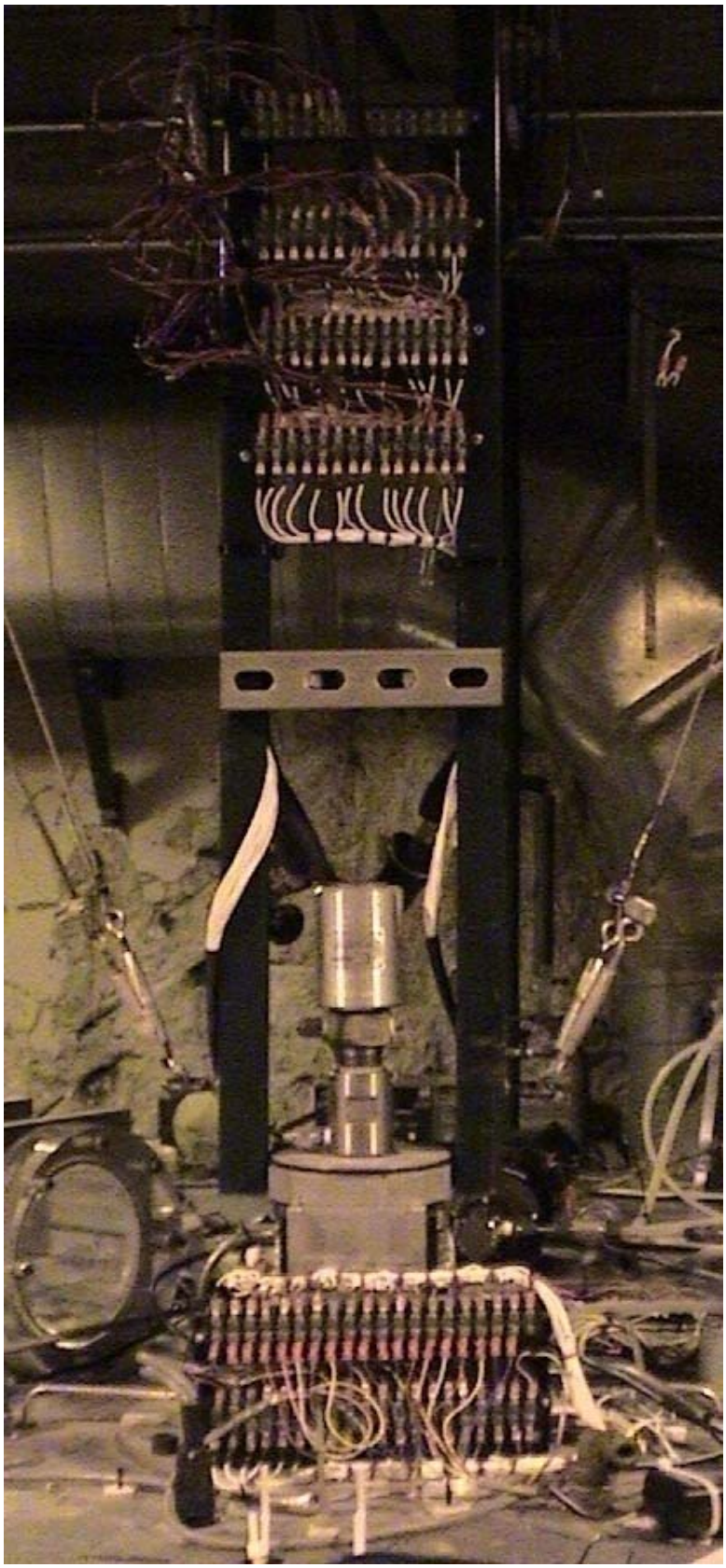

Figure F.1. Updated wiring on the centrifuge table.

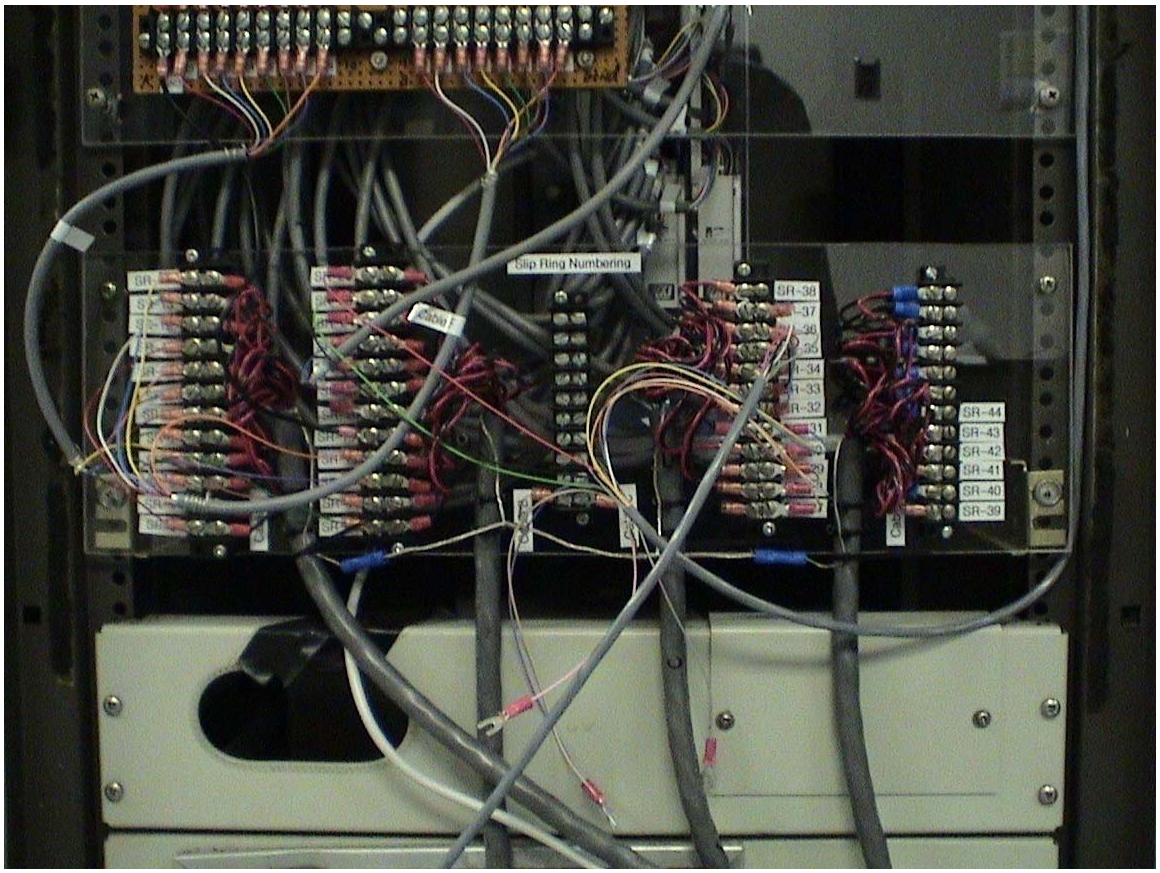

Figure F.2. Wiring panel from centrifuge table to the centrifuge table control room.

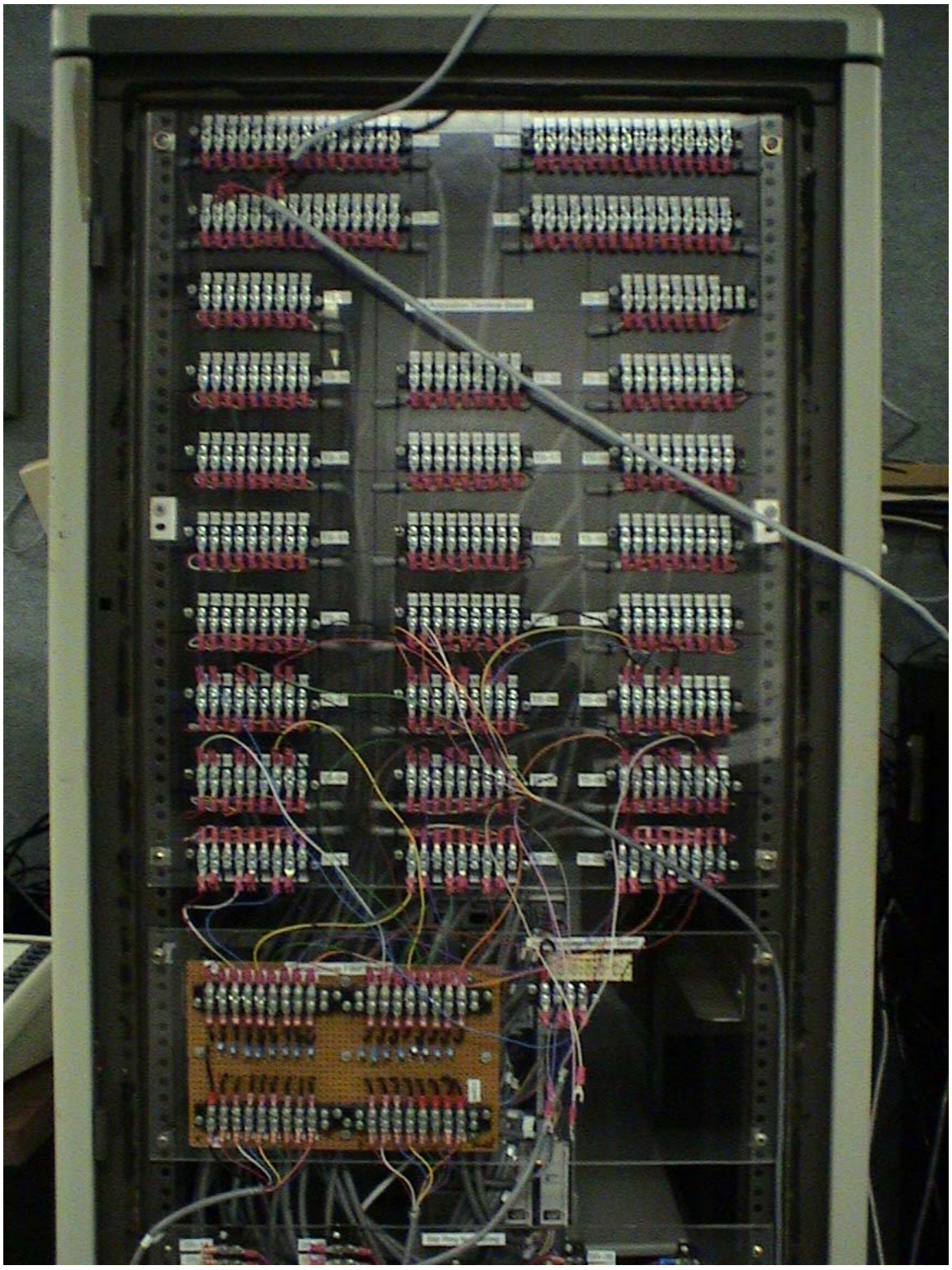

Figure F.3. Wiring panel for the new data acquisition system.

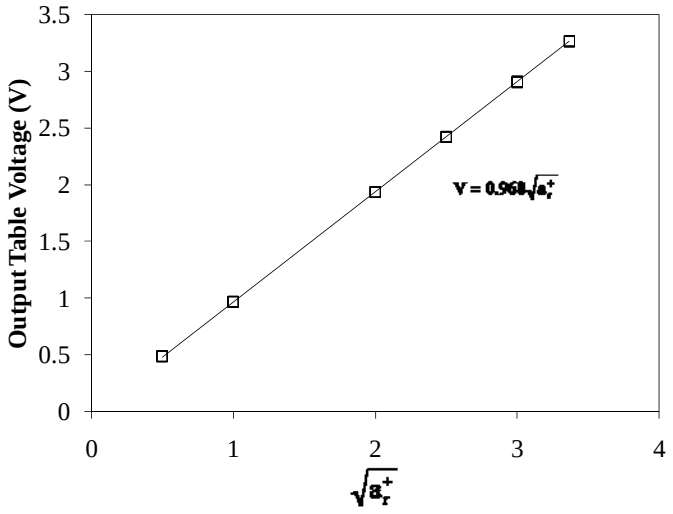


Figure F.4. Centrifuge table voltage versus $\sqrt{a_r^+}$ .

## APPENDIX G. LABVIEW PROGRAMS

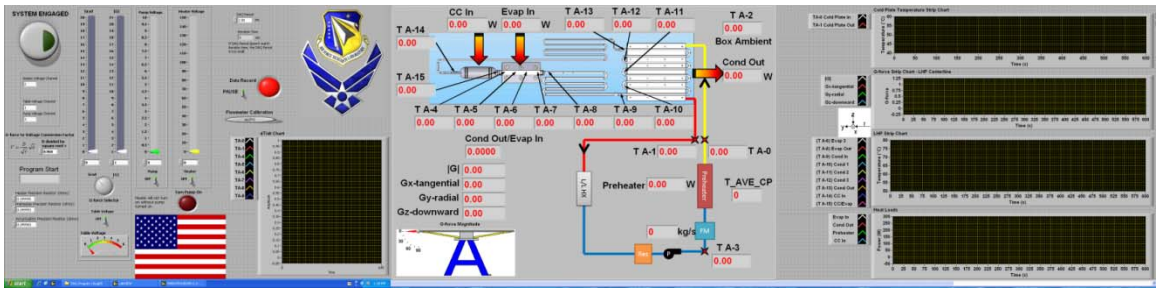


(a)

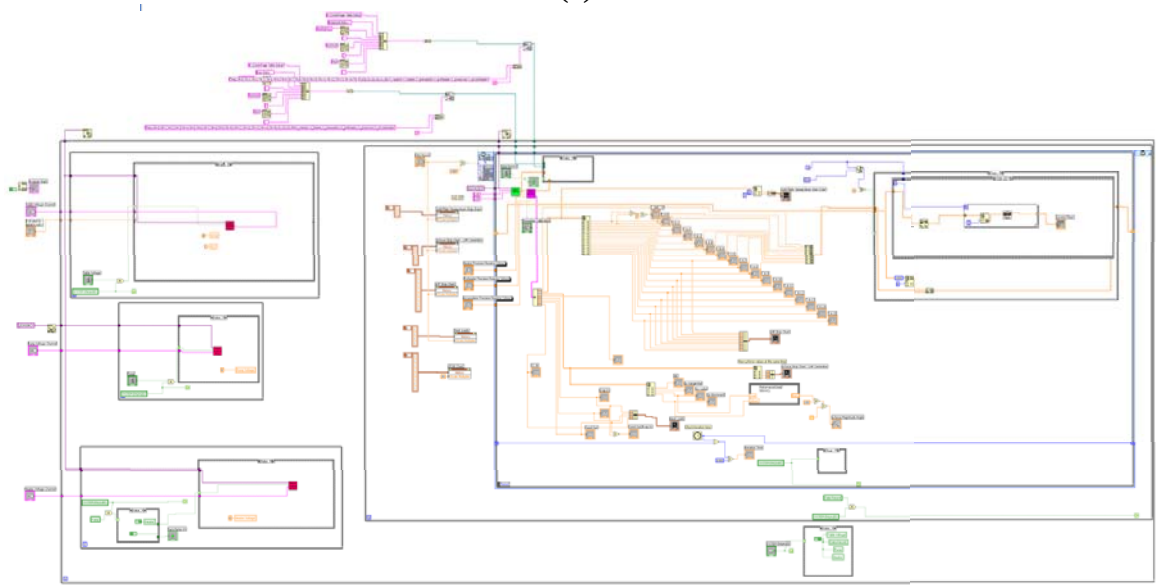

(b)

Figure G.1. LabVIEW VI for the LHP experiment: (a) Front panel; (b) Wire diagram.

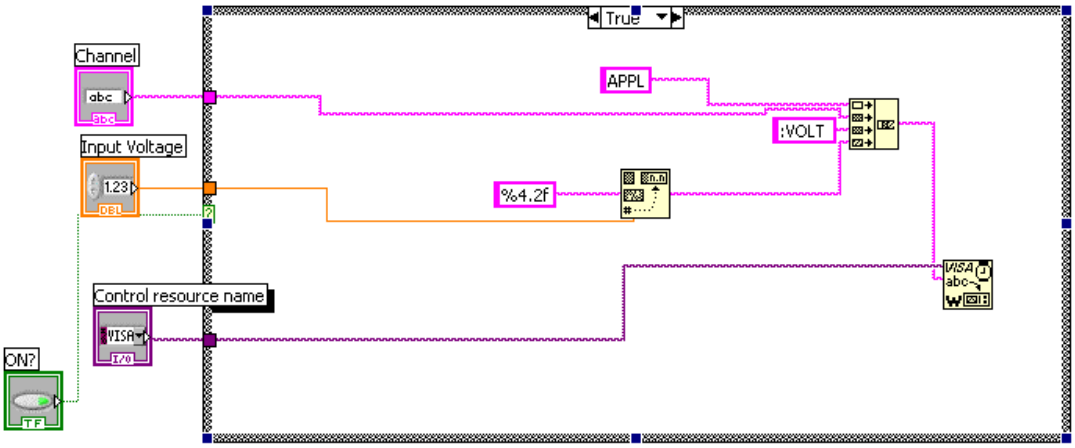


(a)

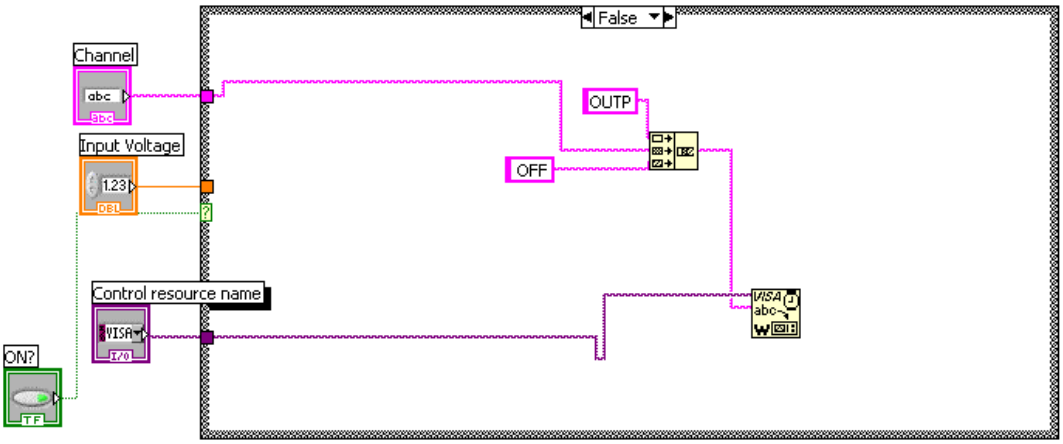


(b)

Figure G.2. LabVIEW sub-VI wire diagram for voltage output control: (a) Output on; (b) Output off.

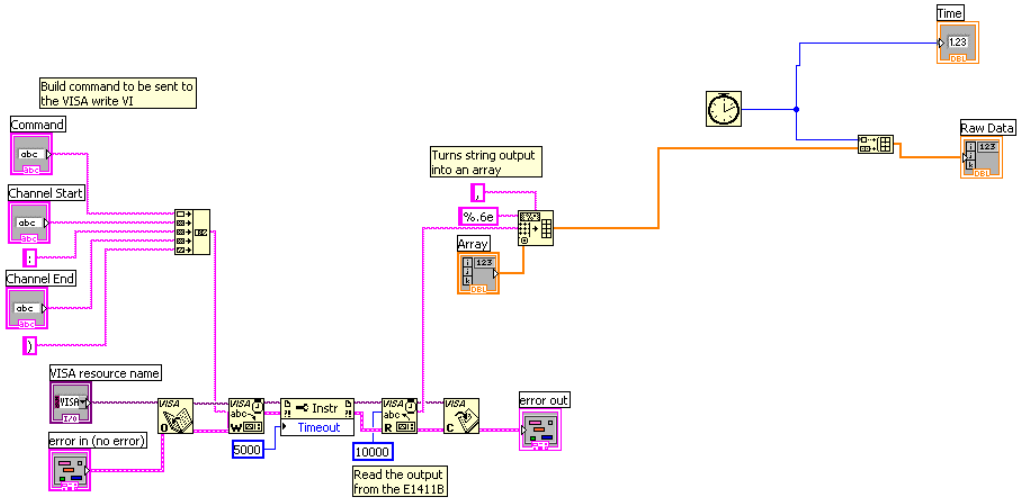


Figure G.3. LabVIEW sub-VI wire diagram for data acquisition communication.

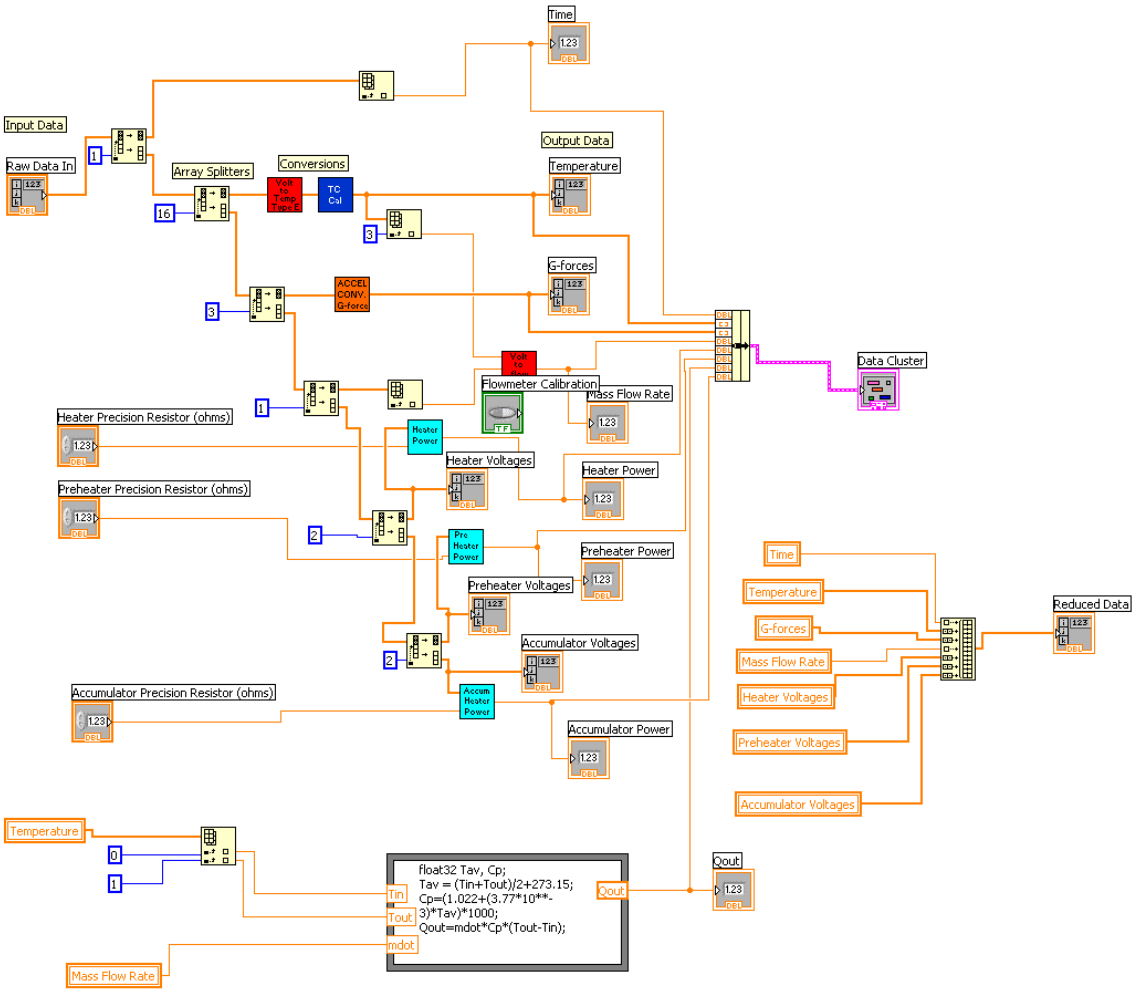


Figure G.4. LabVIEW sub-VI wire diagram for data analyzing.

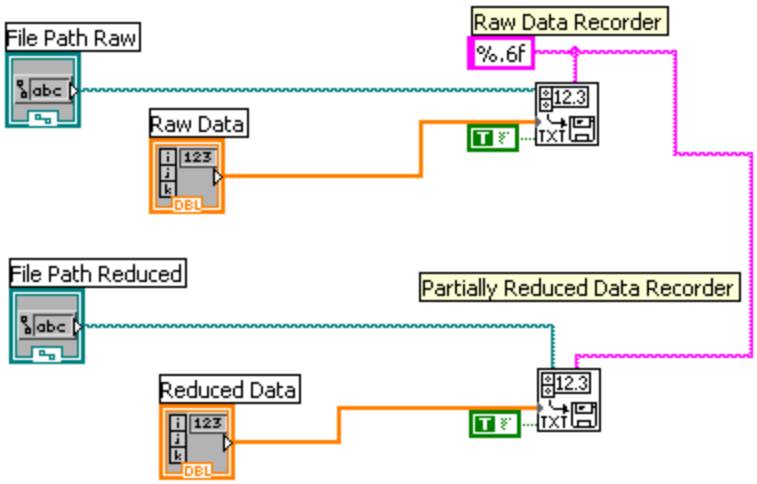


Figure G.5. LabVIEW sub-VI wire diagram for data recording.

## APPENDIX H. CENTRIFUGE WIRING TABLES

Table H.1. E1418A 8/16-CH D/A Converter wiring.

| Module Terminal Number | Terminal Letter | Wire Bundle Number | Wire Color | Terminal Strip Number | Terminal Number | Function | Slip Ring | Wire Color |
|---|---|---|---|---|---|---|---|---|
| 1 | HS | 23 | red | 23 | 01 | | | |
| | HI | | white | | 02 | Centrifuge Table Voltage (+) | | Green-Blue Shield |
| | LO | | blue | | 03 | Centrifuge Table Voltage (-) | | Black-Blue Shield |
| | LS | | yellow | | 04 | | | |
| 2 | HS | | green | | 05 | | | |
| | HI | | brown | | 06 | Heater Power Voltage (+) | | Red-Red Shield |
| | LO | | purple | | 07 | Heater Power Voltage (-) | | Black-Red Shield |
| | LS | | orange | | 08 | | | |
| 3 | HS | 24 | red | | 09 | | | |
| | HI | | white | | 10 | Pump Voltage (+) | 43 | Red-Red Shield |
| | LO | | blue | | 11 | Pump Voltage (-) | 44 | Black-Red Shield |
| | LS | | yellow | | 12 | | | |
| 4 | HS | | green | | 13 | | | |
| | HI | | brown | | 14 | | | |
| | LO | | purple | | 15 | | | |
| | LS | | orange | | 16 | | | |
| 5 | HS | 25 | red | 24 | 01 | | | |
| | HI | | white | | 02 | | | |
| | LO | | blue | | 03 | | | |
| | LS | | yellow | | 04 | | | |
| 6 | HS | | green | | 05 | | | |
| | HI | | brown | | 06 | | | |
| | LO | | purple | | 07 | | | |
| | LS | | orange | | 08 | | | |
| 7 | HS | 26 | red | | 09 | | | |
| | HI | | white | | 10 | | | |
| | LO | | blue | | 11 | | | |
| | LS | | yellow | | 12 | | | |
| 8 | HS | | green | | 13 | | | |
| | HI | | brown | | 14 | | | |
| | LO | | purple | | 15 | | | |
| | LS | | orange | | 16 | | | |
| 9 | HS | 27 | red | 25 | 01 | | | |
| | HI | | white | | 02 | | | |
| | LO | | blue | | 03 | | | |
| | LS | | yellow | | 04 | | | |
| 10 | HS | | green | | 05 | | | |
| | HI | | brown | | 06 | | | |
| | LO | | purple | | 07 | | | |
| | LS | | orange | | 08 | | | |
| 11 | HS | 28 | red | | 09 | | | |
| | HI | | white | | 10 | | | |
| | LO | | blue | | 11 | | | |
| | LS | | yellow | | 12 | | | |
| 12 | HS | | green | | 13 | | | |
| | HI | | brown | | 14 | | | |
| | LO | | purple | | 15 | | | |
| | LS | | orange | | 16 | | | |
| 13 | HS | 29 | red | 26 | 01 | | | |
| | HI | | white | | 02 | | | |
| | LO | | blue | | 03 | | | |
| | LS | | yellow | | 04 | | | |
| 14 | HS | | green | | 05 | | | |
| | HI | | brown | | 06 | | | |
| | LO | | purple | | 07 | | | |
| | LS | | orange | | 08 | | | |
| 15 | HS | 30 | red | | 09 | | | |
| | HI | | white | | 10 | | | |
| | LO | | blue | | 11 | | | |
| | LS | | yellow | | 12 | | | |
| 16 | HS | | green | | 13 | | | |
| | HI | | brown | | 14 | | | |
| | LO | | purple | | 15 | | | |
| | LS | | orange | | 16 | | | |
| | GND | 31 | red | 27 | 01 | | | |
| | EXT TRIGn | | white | | 02 | | | |
| | GND | | blue | | 03 | | | |
| | GND | | yellow | | 04 | | | |
| | CAL HS | | green | | 05 | | | |
| | CAL HI | | brown | | 06 | | | |
| | CAL LO | | purple | | 07 | | | |
| | CAL LS | | orange | | 08 | | | |

Table H.2. Data acqusition terminal board wiring.

| E1476A Module Terminal Number | E1476A Terminal Letter | Main Terminal Strip Number | Main Terminal Number | Function | Slip Ring Number | Wire Color | Board Terminal Number | Location |
|---|---|---|---|---|---|---|---|---|
| 00 | H | 01 | 01 | TC00 | 3 | red | 01 | CP In |
| | L | | 02 | TC Ground | 19 | black | GND | |
| | G | | 03 | | | | | |
| 01 | H | | 04 | TC01 | 4 | white | 02 | CP Out |
| | L | | 05 | TC Ground | 19 | black | GND | |
| | G | | 06 | | | | | |
| 02 | H | | 07 | TC02 | 5 | blue | 03 | Box Ambient |
| | L | | 08 | TC Ground | 19 | black | GND | |
| | G | | 09 | | | | | |
| 03 | H | 02 | 01 | TC03 | 6 | yellow | 04 | Flow meter In |
| | L | | 02 | TC Ground | 19 | black | GND | |
| | G | | 03 | | | | | |
| 04 | H | | 04 | TC04 | 7 | green | 05 | Evap 1 |
| | L | | 05 | TC Ground | 19 | black | GND | |
| | G | | 06 | | | | | |
| 05 | H | | 07 | TC05 | 8 | brown | 06 | Evap 2 |
| | L | | 08 | TC Ground | 19 | black | GND | |
| | G | | 09 | | | | | |
| 06 | H | 03 | 01 | TC06 | 9 | purple | 07 | Evap 3 |
| | L | | 02 | TC Ground | 19 | black | GND | |
| | G | | 03 | | | | | |
| 07 | H | | 04 | TC07 | 10 | orange | 08 | Evap 4 |
| | L | | 05 | TC Ground | 19 | black | GND | |
| | G | | 06 | | | | | |
| 08 | H | | 07 | TC08 | 11 | red | 09 | Evap Out |
| | L | | 08 | TC Ground | 19 | black | GND | |
| | G | | 09 | | | | | |
| 09 | H | 04 | 01 | TC09 | 12 | white | 10 | Cond In |
| | L | | 02 | TC Ground | 19 | black | GND | |
| | G | | 03 | | | | | |
| 10 | H | | 04 | TC10 | 13 | blue | 11 | Cond 1 |
| | L | | 05 | TC Ground | 19 | black | GND | |
| | G | | 06 | | | | | |
| 11 | H | | 07 | TC11 | 14 | yellow | 12 | Cond 2 |
| | L | | 08 | TC Ground | 19 | black | GND | |
| | G | | 09 | | | | | |
| 12 | H | 05 | 01 | TC12 | 15 | green | 13 | Cond 3 |
| | L | | 02 | TC Ground | 19 | black | GND | |
| | G | | 03 | | | | | |
| 13 | H | | 04 | TC13 | 16 | brown | 14 | Cond 4 |
| | L | | 05 | TC Ground | 19 | black | GND | |
| | G | | 06 | | | | | |
| 14 | H | | 07 | TC14 | 17 | purple | 15 | Bayonet In |
| | L | | 08 | TC Ground | 19 | black | GND | |
| | G | | 09 | | | | | |
| 15 | H | 06 | 01 | TC15 | 18 | orange | 16 | Evap/CC |
| | L | | 02 | TC Ground | 19 | black | GND | |
| | G | | 03 | | | | | |
| 16 | H | | 04 | Accel x-axis | 21 | red | 2 | |
| | L | | 05 | Accel GND | 20 | black | 1 | |
| | G | | 06 | | | | | |
| 17 | H | | 07 | Accel y-axis | 22 | white | 3 | |
| | L | | 08 | Accel GND | 20 | black | 1 | |
| | G | | 09 | | | | | |
| 18 | H | 07 | 01 | Accel z-axis | 23 | blue | 4 | |
| | L | | 02 | Accel GND | 20 | black | 1 | |
| | G | | 03 | | | | | |
| 19 | H | | 04 | Flowmeter | 24 | green | | |
| | L | | 05 | Flowmeter GND | 25 | black | | |
| | G | | 06 | | | | | |
| 20 | H | | 07 | Evap Heater Resistor Voltage (+) | 26 | red | | |
| | L | | 08 | Evap Heater Resistor Voltage (-) | 27 | orange | | |
| | G | | 09 | | | | | |
| 21 | H | 08 | 01 | Evap Heater Voltage (+) | 28 | white | | |
| | L | | 02 | Evap Heater Voltage (-) | 29 | brown | | |
| | G | | 03 | | | | | |
| 22 | H | | 04 | Preheater Resistor Voltage (+) | 30 | yellow | | |
| | L | | 05 | Preheater Resistor Voltage (-) | 31 | blue | | |
| | G | | 06 | | | | | |
| 23 | H | | 07 | Preheater Voltage (+) | 32 | red | | |
| | L | | 08 | Preheater Voltage (-) | 33 | black | | |
| | G | | 09 | | | | | |
| 24 | H | 09 | 01 | CC Heater Resistor Voltage (+) | 34 | gray | | |
| | L | | 02 | CC Heater Resistor Voltage (-) | 35 | purple | | |
| | G | | 03 | | | | | |
| 25 | H | | 04 | CC Heater Voltage (+) | 36 | pink | | |
| | L | | 05 | CC Heater Voltage (-) | 37 | tan | | |
| | G | | 06 | | | | | |
| 26 | H | | 07 | | | | | |
| | L | | 08 | | | | | |
| | G | | 09 | | | | | |

## APPENDIX I. SAMPLE CALCULATIONS

Example Calculation of Average Heat Transfer Coefficient for Flat Plate Flow

Given:

Altitude: $H = 5$ km
Mach number: $\mathrm{Ma}_\infty = 0.8$
Wall temperature: $T_w = 135$ °C = 408.15 K
Plate length: $L = 1.0$ m

Calculations:

Freestream temperature:
$T_\infty = (7.7664\text{E-}4)H^4 - (2.8994\text{E-}2)H^3 + (5.3483\text{E-}1)H^2 - (9.5033)H + (4.8507\text{E+}1)$
$T_\infty = 284.37$ K

Freestream density:
$\rho_\infty = (-4.9336\text{E-}6)H^3 + (2.0898\text{E-}3)H^2 - (8.9917\text{E-}2)H + 1.0868$
$\rho_\infty = 0.6870$ kg/m$^3$

Film temperature:
$T^* = T_\infty(0.5 + 0.039\ \mathrm{Ma}_\infty^2) + 0.5T_w = (284.37\text{ K})(0.5+0.039(0.\ 8)^2)+0.5(408.15\text{ K})$
$T^* = 353.36$ K

Air density at the film temperature:
$\rho^* = \rho_\infty/(T_\infty/T^*) = (0.6870\text{ kg/m}^3)(284.37\text{ K})/(353.36\text{ K}) = 0.5528\text{ kg/m}^3$

Freestream speed of sound:
$a_\infty = \sqrt{(\gamma RT_\infty)} = \sqrt{((1.4)(286.9\text{ m}^2/\text{s}^2\cdot\text{K})(\ 284.37\text{ K}))} = 337.97$ m/s

Freestream velocity:
$U_\infty = \mathrm{Ma}_\infty a_\infty = (0.8)(337.97\text{ m/s}) = 270.37$ m/s

Freestream absolute viscosity (Reference values from Incropera and DeWitt, 2002):
$\mu_\infty = \mu_R(T_\infty/T_R)^{0.76} = (184.6 \times 10^{-7}\text{ N}\cdot\text{s/m}^2)(284.37\text{ K} / 300\text{ K})^{0.76}$
$\mu_\infty = 1.772 \times 10^{-5}$ N·s/m$^2$

Reynolds number:
$\mathrm{Re}_L = (\rho_\infty U_\infty L)/\mu_\infty = (0.6870\text{ kg/m}^3)(270.37\text{ m/s})(1\text{ m}) / (1.772 \times 10^{-5}\text{ N}\cdot\text{ s/m}^2)$
$\mathrm{Re}_L = 1.05 \times 10^7$
[TURBULENT]

Prandtl number at the film temperature:
$Pr^* = (-1.2593E-9)T^3 + (1.7778E-6)T^2 - (9.4177E-4)T + (8.6418E-1)$
$Pr^* = 0.6978$

Specific heat at the film temperature:
$C_p^* = (4.4444E-7)T^3 - (3.3333E-5)T^2 - (6.9921E-2)T + (1.0187E+3)$
$C_p^* = 1009.44$ J/(kg·K)

Recovery factor for turbulent flow:
$r = Pr^{*1/3} = (0.6978)^{1/3} = 0.8870$

Adiabatic wall temperature:
$T_{aw} = T_\infty[1+r((\gamma-1)/2)Ma_\infty^2] = (284.37\text{ K})(1+(0.8870)(0.4/2)(0.8)^2) = 316.66$ K

Absolute viscosity at the film temperature:
$\mu^* = \mu_R(T^*/T_R)^{0.76} = (184.6 \times 10^{-7}\text{ N}\cdot\text{ s/m}^2)(353.36\text{ K} / 300\text{ K})^{0.76} = 2.091 \times 10^{-5}$ N·s/m$^2$

Local skin friction coefficient at the end of the plate:
$C_{f,L}^* = 0.455/(\ln^2(0.06\rho^* U_\infty L/\mu^*))$
$= 0.455/(\ln^2(0.06(0.5528\text{ kg/m}^3)(270.37\text{ m/s})(1\text{ m}) / (2.091 \times 10^{-5}\text{ N}\cdot\text{ s/m}^2))$
$= 0.002705$

Local Stanton number at the end of the plate:
$St_L^* = (C_{f,L}^*/2) / (1+12.7(Pr^{*2/3}-1)(C_{f,L}^*/2)^{1/2}$
$= (0.002705/2) / (1+12.7((0.6978)^{2/3}-1)(0.002705/2)^{1/2}) = 0.001502$

Local heat transfer coefficient at the end of the plate:
$h_L = St_L^* \rho^* U_\infty C_p^* = (0.001502)(0.5528\text{ kg/m}^3)(270.37\text{ m/s})(1009.44\text{ J/kg}\cdot\text{K})$
$= 226.7$ W/m$^2$·K

Average heat transfer coefficient over the length of the plate:
$\bar{h} = 1.15\, i_L = 1.15(226.7\text{ W/m}^2\cdot\text{K}) = 260.7$ W/m$^2$·K

Average heat flux dissipated over the plate:
$q_w = \bar{h}(T_w - T_{aw}) = (260.7\text{ W/m}^2\cdot\text{K})(408.15\text{ K} - 316.66\text{ K}) = 23847.7$ W/m$^2$